

Solar Driven Hydrogen Generation with Dye-Sensitised CuCrO_2 Photocathodes



Charles Eric Creissen

Department of Chemistry
University of Cambridge

This dissertation is submitted for the degree of

Doctor of Philosophy

Declaration

This dissertation is the result of my own work and includes nothing which is the outcome of work done in collaboration except as declared in the Preface and specified in the text.

It is not substantially the same as any that I have submitted, or, is being concurrently submitted for a degree or diploma or other qualification at the University of Cambridge or any other University or similar institution except as declared in the Preface and specified in the text. I further state that no substantial part of my dissertation has already been submitted, or, is being concurrently submitted for any such degree, diploma or other qualification at the University of Cambridge or any other University or similar institution except as declared in the Preface and specified in the text.

This thesis does not exceed 60,000 words.

Charles Eric Creissen

March 2019

Solar Driven Hydrogen Generation with Dye-Sensitised CuCrO_2 Photocathodes

Charles Eric Creissen

Abstract

Solar conversion of water into chemical energy carriers offers a sustainable alternative to fossil fuels. Inspired by natural processes, dye-sensitised photoelectrochemical cells provide a platform for H_2 generation from water. Fuel-forming photocathodes are currently limited by the small range of wide-bandgap p-type semiconductors available. The majority of previous reports have employed NiO, which displays low performance with immobilised dyes and catalysts, requiring exploration of other metal oxides. In this thesis, CuCrO_2 is presented as an alternative p-type semiconductor for dye-sensitised H_2 production.

Synthesis and characterisation of CuCrO_2 using a sol-gel method is described. First, co-immobilisation of a phosphonated diketopyrrolopyrrole dye with a Ni-bis(diphosphine) catalyst on CuCrO_2 is presented as a strategy for producing a functional photocathode capable of generating H_2 (Chapter 2). Photocurrent analysis and product detection revealed a high turnover number for the catalyst, outperforming an analogous NiO photoelectrode. The study serves to demonstrate the benefits of adopting delafossite structures for dye-sensitised systems. The versatility of sol-gel synthesised CuCrO_2 was highlighted through immobilisation of ZnSe nanorods (NRs) (Chapter 3). Ligand-stripped ZnSe-NRs were deposited on CuCrO_2 to produce the first reported ZnSe-sensitised photocathode capable of photoelectrochemical proton reduction under solar irradiation.

Hydrothermal synthesis of CuCrO_2 nanoparticles enabled the development of nanostructured inverse opal electrodes (IO- CuCrO_2) using a bottom-up templating method (Chapter 4). These electrodes were explored as a scaffold for solar H_2 production together with a molecular Ni catalyst and two different organic dyes based on perylene monoimide and diketopyrrolopyrrole chromophores. Improved activity over the mesoporous CuCrO_2 films was associated with the novel morphology of the p-SC and the integration of a more suitable dye for hole injection. Photoelectrochemical analysis and a discussion of the influence of molecular components in these highly proficient electrodes provides a basis for future development of dye-sensitised CuCrO_2 -based photocathodes.

Acknowledgements

I would like to thank Prof. Erwin Reisner for his support, guidance, and advice throughout my PhD. The Reisner group has provided a collaborative and welcoming community for me. The social events and entertaining times both outside and within the lab will stick with me forever.

In particular I would like to thank Esther Edwardes Moore, Dr. Kristian Dalle, Mark Bajada, Dr. Bertrand Reuillard, Daniel Antón García, Constantin Sahm, Julian Vigil, and Andreas Wagner for the countless good trips and laughs we have shared. Special thanks are extended to Kristian for the Tuesday afternoon problem classes that kept me up to speed. I also extend my gratitude to Dr. Benjamin Martindale, Dr. David Wakerley, Dr. Timothy Rosser, Dr. William Robinson, Dr. Moritz Kuehnel, Dr. Janina Willkomm, Dr. Jane Leung and Dr. Julien Warnan for being so fun and helpful, both academically and socially.

The NanoDTC in Cambridge are acknowledged for financial support and for training in applied and theoretical nanotechnology. Additional thanks are extended to The Christian Doppler Association for funding in the last stages of my PhD. I would also like to thank those who provided me with materials – Dr. Julien Warnan (**DPP-P**), Dr. Benjamin Martindale and Daniel Antón García (**NiP**), Dr. Moritz Kuehnel and Constantin Sahm (ZnSe), Dr. Yoann Farré and Prof. Fabrice Odobel (**PMI-P**).

I have also received a great deal of support from family (Deirdre, Terry, Alfie, and Henry) and friends outside of Cambridge (James, Josh H, Toby, Alex, Niall, Cam, Rory, Josh K, Doug, and Jem) over the course of my PhD. It would not have been possible without them.

List of Publications

This thesis contains results published in the following peer-reviewed publications:

1. C. E. Creissen, J. Warnan, E. Reisner, 'Solar H₂ generation in water with a CuCrO₂ photocathode modified with an organic dye and a molecular Ni catalyst', *Chem. Sci.*, 2018, **9**, 1439-1447.
2. M. F. Kuehnel[†], C. E. Creissen[†], C. D. Sahn[†], D. Wielend, A. Schlosser, K. L. Orchard, E. Reisner, 'ZnSe Nanorods as Visible-Light Absorbers for Photocatalytic and Photoelectrochemical H₂ Evolution in Water', *Angew. Chem. Int. Ed.*, 2019, **58**, 5059 - 5063. [†]denotes equal contribution
3. C. E. Creissen, J. Warnan, D. Antón-García, F. Odobel, E. Reisner, 'Next Generation CuCrO₂ Photocathodes for Dye-Sensitised H₂ Production', *Manuscript in Preparation*, 2019.

Contributions were also made to the following publications but were not included in this thesis:

1. M. A. Gross, C. E. Creissen, K. L. Orchard, E. Reisner, 'Photoelectrochemical hydrogen production in water using a layer-by-layer assembly of a Ru dye and Ni catalyst on NiO', *Chem. Sci.*, 2016, **7**, 5537 – 5546.
2. H. Liu, V. Andrei, K. J. Jenkinson, A. Regoutz, N. Li, C. E. Creissen, A. E. Wheatley, H. Hao, E. Reisner, D. S. Wright, S. D. Pike, 'Single-Source Bismuth (Transition Metal) Polyoxovanadate Precursors for the Scalable Synthesis of Doped BiVO₄ Photoanodes', *Adv. Mater.*, 2018, **30**, 1804033.

Table of Contents

1. Introduction	1
1.1. Artificial Photosynthesis	1
1.1.1. Photocatalysis with Suspension Systems	2
1.1.2. PV-Electrolysis	3
1.1.3. Photoelectrochemical Cells	4
1.1.4. Dye-Sensitised Photoelectrochemical Cells	5
1.2. Catalysts	7
1.2.1. Figures of Merit	7
1.2.2. Heterogeneous Catalysts	7
1.2.3. Molecular Catalysts	8
1.3. Photosensitisers	10
1.3.1. Molecular Dyes	11
1.3.2. Quantum Dots	13
1.4. Semiconductor Electrochemistry	14
1.4.1. Band Structure in Semiconductors	14
1.4.2. Semiconductor/Electrolyte Solution Interface	17
1.4.3. Mott-Schottky Analysis	19
1.4.4. Key Parameters for p-Type Semiconductors in DSPCs	22
1.5. Dye-Sensitised Photocathodes	22
1.5.1. Performance Evaluation	22
1.5.2. Hydrogen Generating DSPCs	24
1.5.3. Summary of Current DSPCs	27
1.6. Delafossite CuCrO₂	28
1.7. Project Aims and Outline	30
2. Hydrogen Generation with Organic Dye-Sensitised CuCrO₂ and a Co-Immobilised Molecular Catalyst	32
2.1. Introduction	32
2.2. CuCrO₂ Synthesis and Physical Characterisation	33
2.2.1. Mott-Schottky Analysis	37
2.3. Molecular Components	38
2.3.1. Organic Dye Properties	38
2.3.2. Molecular Catalyst Properties	39
2.4. Photoelectrochemistry of DPP-P Immobilised on CuCrO₂	40
2.5. Photoelectrochemistry with Co-Immobilised DPP-P and NiP	44
2.6. Conclusions	49
2.7. Experimental Section	50
3. Photoelectrochemical Hydrogen Generation with ZnSe Nanorods	54
3.1. Introduction	54
3.2. ZnSe Nanorods	56
3.2.1. Synthesis and Characterisation	56
3.2.2. Photocatalytic Properties	57
3.3. Assembly and Characterisation of CuCrO₂ ZnSe Photoelectrodes	58

3.4.	Hydrogen Generation with CuCrO ₂ ZnSe Electrodes	61
3.5.	Conclusions.....	67
3.6.	Experimental Section.....	68
4.	Next Generation CuCrO₂ Photocathodes for Dye-Sensitised H₂ Production	73
4.1.	Introduction	73
4.2.	Development of Inverse Opal Structures.....	75
4.2.1.	CuCrO ₂ Nanoparticle Synthesis and Characterisation	75
4.2.2.	CuCrO ₂ Inverse Opal Structures.....	76
4.3.	Photosensitiser Properties	79
4.4.	Photoelectrode Assembly and Characterisation	81
4.5.	IO-CuCrO ₂ Acceptor Studies.....	83
4.5.1.	Thickness Optimisation with DPP-P	83
4.5.2.	Comparison of PMI-P and DPP-P.....	84
4.6.	Photoelectrochemical H ₂ Generation	85
4.7.	Conclusions.....	96
4.8.	Experimental Section.....	97
5.	Conclusions and Outlook.....	101
6.	References.....	107
A.	Appendix.....	126
A.1.	H ₂ Quantification by Gas Chromatography	126
A.2.	Additional Figures.....	127

List of Figures

Figure 1.1 – Illustration of ‘one pot’ photocatalysis	3
Figure 1.2 – Illustration of PV-electrolysis and photoelectrochemical cells	5
Figure 1.3 – Illustration of a dye-sensitised photoelectrochemical (DSPEC) cell	6
Figure 1.4 – The active site of [FeFe]-H ₂ ase and Ni bis(diphosphine) molecular catalysts... ..	9
Figure 1.5 – Molecular structure of NiP	9
Figure 1.6 – Mechanism of H ₂ generation with Dubois-type Ni catalysts.....	10
Figure 1.7 – Examples organic dyes.....	12
Figure 1.8 – Illustration of molecular orbital formation	14
Figure 1.9 – Representation of CB and VB dispersion relations for a semiconductor.	16
Figure 1.10 – Illustration of band bending exhibited by a p-SC	18
Figure 1.11 – Illustration of a p-SC under bias for flatband condition	20
Figure 1.12 – Phase lag between an AC voltage and the current response.....	20
Figure 1.13 – Layer-by-layer assembly procedure.....	26
Figure 1.14 – Crystal structure CuCrO ₂	29
Figure 2.1 – Reductive quenching pathway for a DSPC.....	33
Figure 2.2 – XRD pattern of a CuCrO ₂ electrode	35
Figure 2.3 – UV-Vis spectrum and Tauc plot of a CuCrO ₂ electrode	35
Figure 2.4 – SEM images of a CuCrO ₂ film.	36
Figure 2.5 – Mott-Schottky plot of a CuCrO ₂ electrode	37
Figure 2.6 – Molecular structure of DPP-P	38
Figure 2.7 - Molecular structure of the catalyst NiP	39
Figure 2.8 – Photographs UV-Vis spectrum of CuCrO ₂ DPP-P	40
Figure 2.9 – Chronoamperometry analysis with CuCrO ₂ DPP-P using an SEA	41
Figure 2.10 – LSVs of DPP-P -sensitised CuCrO ₂ and NiO electrodes using an SEA	43
Figure 2.11 – LSVs of CuCrO ₂ DPP-P/NiP and NiO DPP-P/NiP electrodes.	44
Figure 2.12 – Chronoamperometry measurements of CuCrO ₂ DPP-P/NiP and NiO DPP-P/NiP electrodes	45
Figure 2.13 – Cyclic voltammograms of a CuCrO ₂ electrode	46
Figure 2.14 – IPCE measurements for CuCrO ₂ and CuCrO ₂ DPP-P/NiP electrodes.	46
Figure 2.15 – CPPE of a CuCrO ₂ DPP-P/NiP electrode over 2 h.....	47
Figure 3.1 – Illustration of photocatalytic proton reduction with a sacrificial electron donor and photoelectrochemical hydrogen generation with ZnSe-sensitised CuCrO ₂	55
Figure 3.2 – Physical characterisation of ZnSe-NRs	56

Figure 3.3 – Photocatalysis results with ZnSe-NRs.	57
Figure 3.4 – Photocurrents with different strategies to form ZnSe layers on CuCrO ₂	58
Figure 3.5 – Cross-sectional SEM image of a CuCrO ₂ ZnSe electrode.....	60
Figure 3.6 – EDS elemental map of the CuCrO ₂ /CuCrO ₂ ZnSe edge.	60
Figure 3.7 – UV-Vis spectra of ZnSe, CuCrO ₂ , and CuCrO ₂ ZnSe electrodes	61
Figure 3.8 – LSVs uof CuCrO ₂ and CuCrO ₂ ZnSe electrodes	62
Figure 3.9 – Chronoamperograms of CuCrO ₂ and CuCrO ₂ ZnSe electrodes.....	62
Figure 3.10 – IPCE measurements for CuCrO ₂ and CuCrO ₂ ZnSe electrodes	64
Figure 3.11 – CPPE of a CuCrO ₂ ZnSe electrode over the course of 4 h.	65
Figure 4.1 – Illustration of the two different dye structures (DPP-P and PMI-P) with co-immobilised NiP on IO-CuCrO ₂	75
Figure 4.2 – TEM images of CuCrO ₂ -NPs.	76
Figure 4.3 – Illustration of the method used to form IO-CuCrO ₂ films.....	77
Figure 4.4 – SEM images of IO-CuCrO ₂ films formed using 15 wt% dispersions.....	77
Figure 4.5 – SEM images of IO-CuCrO ₂ films formed using 7.5 wt% dispersions.....	78
Figure 4.6 – XRD patterns for CuCrO ₂ -NPs and IO-CuCrO ₂ films.....	78
Figure 4.7 – Molecular structures of DPP-P and PMI-P	80
Figure 4.8 – UV-Vis spectra of DPP-P and PMI-P recorded in DMF.	80
Figure 4.9 – Photographs of IO-CuCrO ₂ , IO-CuCrO ₂ DPP-P/NiP , and IO-CuCrO ₂ PMI-P/NiP electrodes with corresponding UV-Vis spectra	82
Figure 4.10 – Chronoamperometry experiments with different IO-CuCrO ₂ thickness using an SEA.....	84
Figure 4.11 – Chronoamperometry experiments with IO-CuCrO ₂ DPP-P and IO-CuCrO ₂ PMI-P electrodes using an SEA	84
Figure 4.12 – LSVs of IO-CuCrO ₂ DPP-P/NiP and IO-CuCrO ₂ PMI-P/NiP electrodes.....	86
Figure 4.13 – Chronoamperometry experiments at an applied potential of +0.3 V vs. RHE with IO-CuCrO ₂ DPP-P/NiP and IO-CuCrO ₂ PMI-P/NiP electrodes.....	87
Figure 4.14 – Chronoamperometry experiments at an applied potential of 0.0 V vs. RHE with IO-CuCrO ₂ DPP-P/NiP and IO-CuCrO ₂ PMI-P/NiP electrodes.....	87
Figure 4.15 – Chronoamperometry experiments at an applied potential of 0.0 V vs. RHE with IO-CuCrO ₂ , IO-CuCrO ₂ dye , and IO-CuCrO ₂ dye/NiP electrodes	89
Figure 4.16 – Dark electrolysis of IO-CuCrO ₂ and IO-CuCrO ₂ phenylphosphonic acid electrodes	90
Figure 4.17 – IPCE measurements of IO-CuCrO ₂ , IO-CuCrO ₂ DPP-P/NiP , and IO-CuCrO ₂ PMI-P/NiP electrodes.....	91
Figure 4.18 – CPPE of IO-CuCrO ₂ DPP-P/NiP and IO-CuCrO ₂ PMI-P/NiP at 0 V and +0.3 V vs. RHE	92

Figure 4.19 – Comparison of CPPE results at applied potentials of 0.0 V vs. RHE and +0.3 V vs. RHE with IO-CuCrO ₂ DPP-P/NiP and IO-CuCrO ₂ PMI-P/NiP electrodes	93
Figure 4.20 – Comparison of CPPE results with IO-CuCrO ₂ DPP-P/NiP and CuCrO ₂ DPP-P/NiP electrodes	94

List of Tables

Table 4.1 – Maximum absorption wavelength (λ_{max}) with corresponding extinction coefficient (ϵ), zero-zero excitation energy (E_{00}), excited state reduction potential (ES^*/S^-), and ground state reduction potential (ES/S^-) for PMI-P and DPP-P	81
Table 4.2 – Dye and catalyst loadings for IO-CuCrO ₂ and mesoporous CuCrO ₂ electrodes.	82
Table 4.3 – Amount of H ₂ generated, TON _{NiP} , and FE for each photoelectrode following CPPE at +0.3 V and 0.0 V vs. RHE for 2 h.	92

List of Abbreviations

AA	Ascorbic Acid
AM 1.5G	Air Mass 1.5 Global
BET	Brunauer-Emmett-Teller
bpy	Bipyridine
CB	Conduction Band
CPE	Constant Phase Element
CPPE	Controlled Potential Photoelectrolysis
C_{sc}	Interfacial Capacitance
CV	Cyclic Voltammetry
DHA	Dehydroascorbic Acid
DMF	<i>N,N</i> -Dimethylformamide
DOS	Density of States
DPP	Diketopyrrolopyrrole
DSP	Dye-Sensitised Photocatalysis
DSPC	Dye-Sensitised Photocathode
DSPEC	Dye-Sensitised Photoelectrochemical
DSSC	Dye-Sensitised Solar Cell
DTDP	4,4'-Dithiodipyridine
E_{00}	Zero-Zero Excitation Energy
E_{app}	Applied Potential
EDS	Energy-Dispersive X-Ray Diffraction
EDT	Ethanedithiol
E_{fb}	Flatband Potential
EIS	Electrochemical Impedance Spectroscopy
E_{redox}	Redox Potential
FE	Faradaic Efficiency
GC	Gas Chromatography
HEC	Hydrogen Evolution Catalyst
HOMO	Highest Occupied Molecular Orbital
ICP-OES	Inductively Coupled Plasma-Optical Emission Spectroscopy
ICSD	Inorganic Crystal Structure Database
IO	Inverse Opal
IPCE	Incident Photon-to-Current Efficiency

ITO	Indium Tin Oxide
j	Photocurrent Density
LSV	Linear Sweep Voltammetry
LUMO	Lowest Unoccupied Molecular Orbital
MEPA	3-Mercaptoethylphosphonic Acid
MLCT	Metal-to-Ligand Charge Transfer
MPA	3-Mercaptopropionic Acid
NP	Nanoparticle
NR	Nanorod
PEC	Photoelectrochemical
PEM	Proton Exchange Membrane
PMI	Perylene Monoimide
PS	Polystyrene
p-SC	p-Type Semiconductor
PV	Photovoltaic
QD	Quantum Dot
R _{CT}	Charge Transfer Resistance Element
RHE	Reversible Hydrogen Electrode
R _s	Solution Resistance Element
SEA	Sacrificial Electron Acceptor
SED	Sacrificial Electron Donor
SEM	Scanning Electron Microscopy
St	Stearate
STH	Solar-to-Hydrogen
TBAOH	Tetrabutylammonium Hydroxide
TCO	Transparent Conducting Oxides
TEM	Transmission Electron Microscopy
TEOA	Triethanolamine
TOF	Turnover Frequency
TON	Turnover Number
UV-Vis	Ultraviolet-Visible Spectroscopy
VB	Valence Band
WOC	Water Oxidation Catalyst
wt%	Weight Percent
XRD	X-Ray Diffraction
ϵ	Molar Extinction Coefficient

Chapter 1

Introduction

Human reliance on energy derived from fossil fuels has played a significant role in global warming over the past century.^{1,2} Increasing worldwide energy demand has raised concerns over depletion of these finite reserves as well as the environmental impact of their usage. With fossil fuels comprising more than 85% of primary fuel consumption in 2017,³ securing a sustainable replacement requires political involvement and technological developments to ensure economic viability. Natural resources including wind, hydroelectric, and solar power, provide a route to electrical energy, with photovoltaic technology currently a frontrunner in terms of growth.⁴ However, intermittency and seasonal variations mean that a combination of solar- and wind-derived energy sources together with storage of any surplus electricity is likely necessary to meet future demand.⁵ Furthermore, reliance on chemical feedstocks for commodity production and heavy dependence on fuels in the transportation sector underlines the need for direct energy storage solutions. Secondary batteries offer a solution but issues including low energy density, short lifetimes, safety concerns, and high initial costs limit widespread employment.^{5,6} For these reasons, direct synthesis of chemical fuels using solar energy is a highly attractive approach.

In natural photosynthesis, living organisms use solar light to store energy in chemical bonds. Enzyme-catalysed reactions are used to convert CO₂ and H₂O into organic molecules, where complex electron transfer chains ensure highly efficient charge transfer between light harvesting components – an exemplary pathway being the four-electron oxidation of water and simultaneous generation of reducing equivalents following light absorption by photosystem II.⁷ Although effective for living organisms, overall solar energy conversion to biomass is low (< 1%) since energy is consumed through metabolism and reproduction.⁸ To redirect charge transfer and generate fuels for human consumption, a synthetic approach can be adopted. Replicating the core processes of light harvesting, charge separation, and catalysis in synthetic systems provides a route to solar-driven energy conversion – this is termed artificial photosynthesis.⁹

1.1. Artificial Photosynthesis

Artificial photosynthesis systems are capable of using solar light to effectively ‘split’ water into its molecular components, H₂ and O₂, or promote the conversion of CO₂ into value-added

chemicals. H₂ is a storable fuel source with a high energy density (142 MJ kg⁻¹), which generates water as the only side product upon combustion.^{10,11} Recent progress in the development of fuel cells has opened up the scope for use in H₂-powered vehicles and future prospects suggest that this technology could compete with secondary batteries in the transport sector.^{12,13} Additionally, H₂ is used as a feedstock in the chemical industry in processes such as the Haber-Bosch synthesis of ammonia and can be used to form hydrocarbons through the Fischer-Tropsch process.¹⁴ However, over 95 % of the world's H₂ comes from fossil fuels, the majority being sourced from steam reforming of methane.¹⁵ Shifting this supply to a renewable source through solar water splitting is a necessary step in mitigating climate change.

The thermodynamic barrier to water splitting is +237 kJ mol⁻¹, corresponding to an electrochemical potential of -1.23 V (Equation 1.3). However when accounting for catalyst overpotential and material-dependent factors, realistic values in the range of at least 1.6 – 1.7 V are expected for solar-driven devices.¹⁶ Devices to carry out this reaction must therefore meet this fundamental energy requirement.



Three technological approaches to achieve artificial photosynthesis have been proposed: 'one-pot' photocatalysis; photovoltaic-driven electrolysis; and photoelectrochemical (PEC) cells. Each have their own merits with respect to economic and technical implementation.^{17–19}

1.1.1. Photocatalysis with Suspension Systems

Colloidal suspensions of semiconductor nanoparticles can be used to directly split water into its individual components. The thermodynamic properties of semiconductors must be aligned with the redox potentials of the desired reaction. For full water splitting, the conduction band (CB) must be more negative than the proton reduction potential and the valence band (VB) more positive than the oxidation potential of water. Unfortunately, the range of semiconductors with the thermodynamic and kinetic requirements for both water oxidation and proton reduction is limited.²⁰ Instead, a Z-scheme can be adopted where separate particles for oxidation and reduction reactions are coupled using a redox mediator, which permits dual light

absorption, mimicking processes in natural photosynthesis (**Figure 1.1**).²¹ The proton reduction half-reaction can be modelled using a sacrificial electron donor (SED), and the oxidation process with a sacrificial electron acceptor (SEA), removing complications associated with assembly of the full setup. Z-scheme arrangements face challenges with safety due to the formation of explosive gas mixtures in the full setup. Additionally, replacement of the sacrificial component is required for commercial application. Proposed solutions to bypass these issues include organic transformations, biomass oxidation, or plastic reforming to replace O₂ generation.^{22–26} For these reasons, this approach is currently considered as the least developed of the three configurations, however easy integration in flow systems and the use of cheap and non-toxic components make this a promising route to future solar fuel generation.

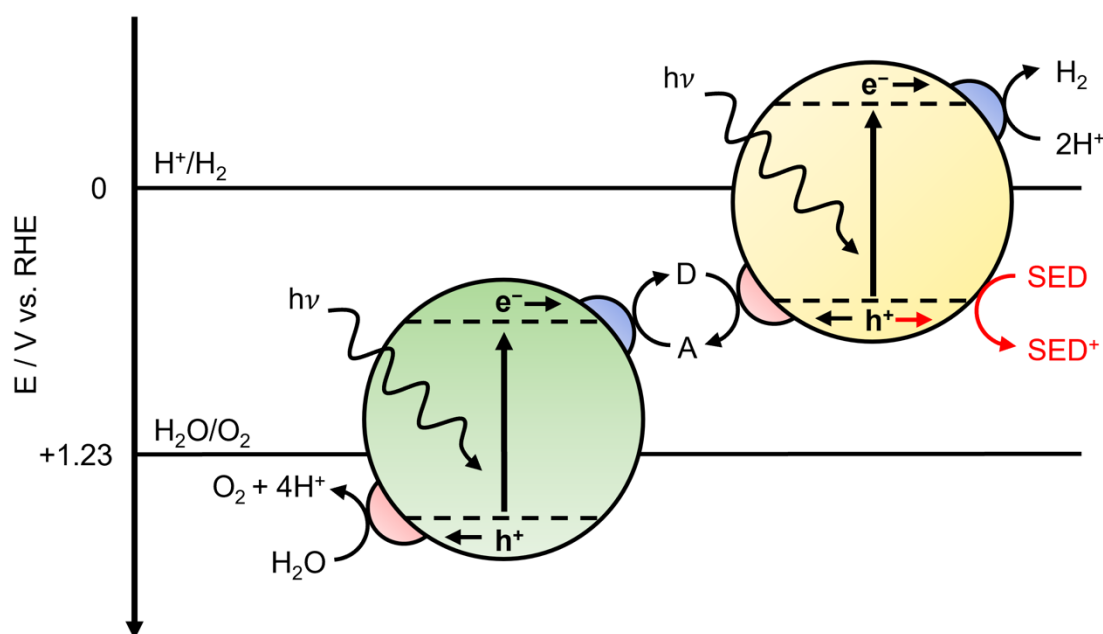


Figure 1.1 – Illustration of ‘one pot’ photocatalysis with a Z-scheme configuration showing the route to oxidation of a sacrificial electron donor highlighted in red. D = donor, A = acceptor, h⁺ = holes, e⁻ = electrons. Dashed lines are representative of conduction and valence band positions.

1.1.2. PV-Electrolysis

Devices combining the already established fields of high efficiency PV cells and water electrolyzers provide a practical route to H₂ generation (**Figure 1.2**).^{18,19,27,28} Such devices bypass problems such as pH-dependent stability of different metal oxide semiconductors and light-induced photocorrosion in aqueous solution, by decoupling light absorption from

catalysis. These devices are considered the most advanced of the three types with benchmark PV-electrolysis cells having achieved over 30% solar-to-hydrogen (STH) efficiency using solar concentrators,²⁹ and Si-based devices achieving over 14% STH efficiency.³⁰ Despite their high performance, the cost of setup currently outweighs the value of fuel generated and they are considered too expensive for implementation on a large scale.^{5,31,32} Recent research has been aimed towards a combined approach incorporating PEC devices with PV cells to avoid electricity losses or to enhance catalysis.^{32,33} The most significant progress with PV-electrolysis is likely to come from engineering solutions that target stability issues with electrolyzers and membranes,³⁴ or integration with grid electricity to effectively couple solar-driven and electrocatalytic H₂ generation.¹⁹

1.1.3. Photoelectrochemical Cells

PEC cells present an attractive route to solar fuel generation.^{9,18,35–39} In such systems, a photoanode responsible for the oxidation reaction is coupled with a photocathode, where the reduction reaction takes place. The catalysts can be immobilised directly on the semiconductor surface or dissolved in solution (**Figure 1.2**). Separation of the two compartments with a proton exchange membrane (PEM) allows for easy extraction of O₂ and H₂ without substantial crossover, thereby avoiding explosive gas mixtures. Such an arrangement also allows each half-reaction to be studied in a three-electrode electrochemical setup, enabling individual optimisation of reduction and oxidation components. Unlike with suspension systems, there is no need for SEDs or SEAs for half-reaction optimisation, therefore unwanted side reactions can be avoided which in some cases can generate damaging products and give false estimations of activity when in a full Z-scheme system.^{40–42} However, material processing costs, stability issues, and low efficiency, have so far hindered commercial application. On the photocathode side, narrow-bandgap p-type semiconductors (p-SCs) tend to suffer from instability in aqueous conditions. Protective coatings have been successfully employed in many cases to improve stability but eventual leakage results in device degradation.^{43–47} To circumvent this problem, more stable narrow-bandgap p-SCs need to be discovered or cheaper and commercially viable protective coatings engineered. Alternatively, wide-bandgap p-SCs that tend to show high stability in aqueous solution can be coupled with inexpensive light absorbers in dye-sensitised photoelectrochemical (DSPEC) cells.^{48–50}

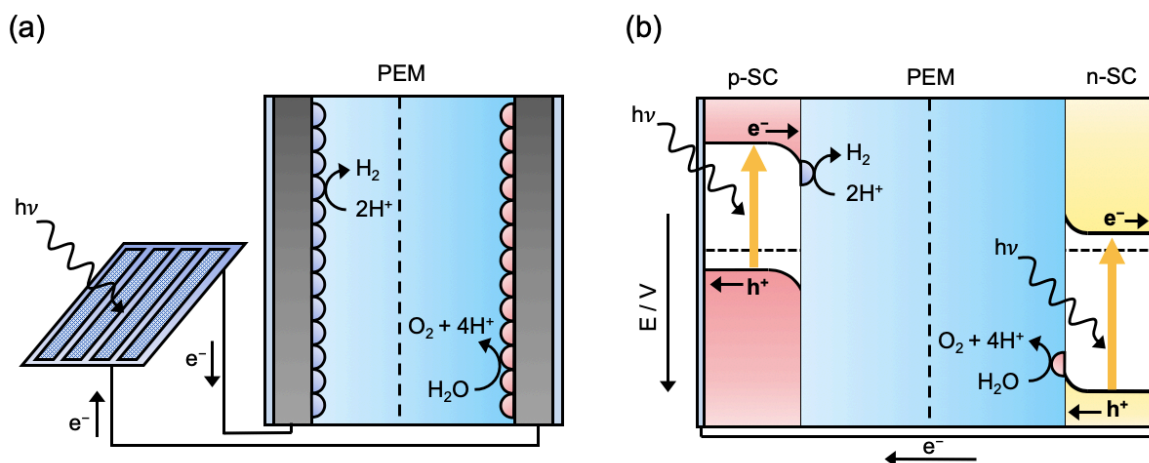


Figure 1.2 – Illustration of a) PV-electrolysis and b) photoelectrochemical cell devices for solar water splitting. PEM = proton exchange membrane, blue and red semicircles are hydrogen and oxygen evolution catalysts respectively.

1.1.4. Dye-Sensitised Photoelectrochemical Cells

Solar-driven reactions can be performed using a dye-sensitised derivative of conventional PEC devices. These systems draw inspiration from dye-sensitised solar cells (DSSCs), in which stable wide-bandgap semiconductors are functionalised with light-harvesting components to generate electricity using a redox mediator.^{51,52} Replacement of the redox mediator with aqueous solution, and addition of water oxidation and proton reduction catalysts enables PEC water splitting in DSPEC cells (**Figure 1.3**).^{48–50,53} This term is extended to include quantum dot (QD) systems in this thesis.

In line with the function of chromophores in natural photosynthesis, molecular dyes harvest sunlight and transfer photogenerated charge to or from a catalytic site. The catalyst can be coupled directly to the dye species or co-immobilised on the semiconductor using a range of immobilisation strategies.^{54–57} The catalyst relies on sufficient thermodynamic driving force to reach a catalytically active state, therefore the selection must be rationalised with respect to a specific molecular dye. Additionally, the kinetics of hole injection and electron transfer to the catalyst control the efficiency, therefore specific design of a dye to suit kinetically fast charge transfer is required. Semiconductors are responsible for regeneration of the dye, a proximity-dependent process facilitated through functionalisation with surface anchoring groups.^{58,59} Coupling an n-type photoanode with a p-type photocathode enables full water splitting, where the additive photovoltage removes the need for an external bias.^{60,61}

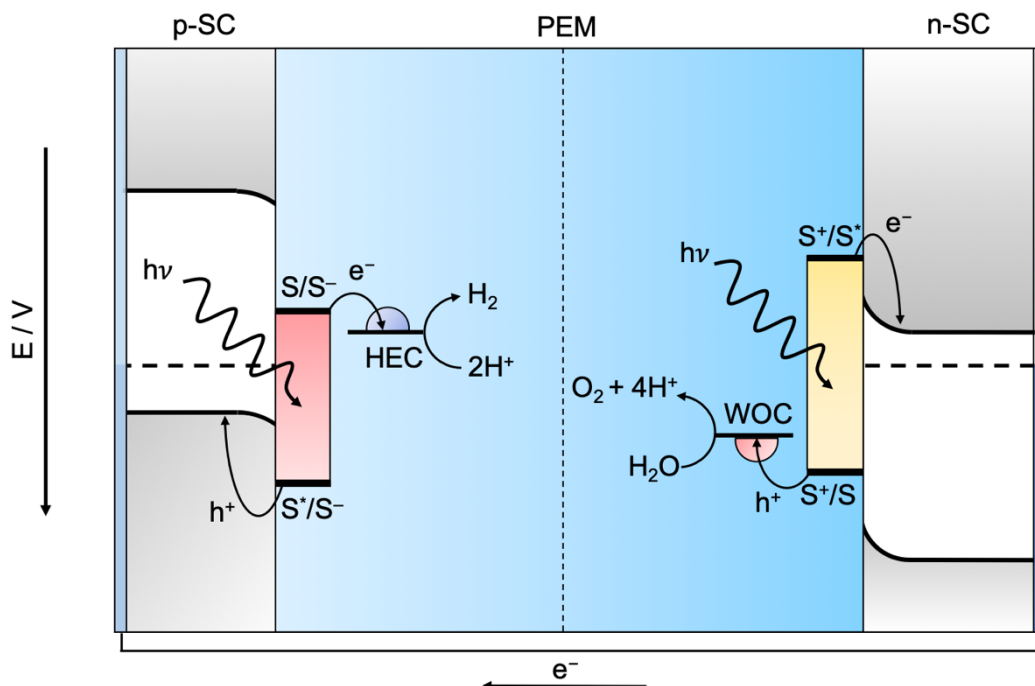


Figure 1.3 – Illustration of a dye-sensitized photoelectrochemical (DSPEC) cell, where h^+ = holes, e^- = electrons, S = sensitiser, HEC = hydrogen evolution catalyst, and WOC = water oxidation catalyst.

Dye-sensitized photoanode development has seen dramatic progress in recent years owing to better understanding of the dye/semiconductor interface as well as engineering of materials for enhanced charge separation and reduced recombination.^{48,50,62–64} Dye-sensitized photocathodes (DSPCs) responsible for fuel-forming reactions are currently less advanced; their limited photocurrents represent a bottleneck for tandem DSPEC cell development.^{48,49} Identifying photocurrent-limiting factors is however quite practical in such arrangements, as the modular assembly allows each component to be tailored individually and performance analysis with spectroscopic and electrochemical evidence affords a better understanding of the DSPC as a whole.

The work presented in this thesis will focus on H_2 -generating DSPCs based on p-type semiconductors (p-SCs). The influence of semiconductor material and morphology is emphasised through descriptions of functional systems incorporating a range of photosensitisers and catalysts. These separate components are discussed in the following sections and examples of fully assembled proton reduction systems presented in Section 1.5.

1.2. Catalysts

Catalysts incorporated in dye-sensitised systems fall into three classes: heterogeneous, molecular, and enzymatic. Although enzymes are often regarded as model examples, their incorporation in DSPEC cells is limited to only one case and will therefore not be discussed in detail here.⁶⁵ This section will outline some key parameters used to evaluate catalyst performance followed by a discussion of some key concepts and examples with heterogeneous and molecular catalysts.

1.2.1. Figures of Merit

The overpotential (η) for a catalyst defines the minimum electrochemical potential required to initiate substrate conversion. A low overpotential for a catalyst is desired as the reaction will proceed with a lower energy input. With respect to DSPEC cells, the dye needs to provide sufficient driving force to enable the catalytic reaction. The turnover number (TON) is the number of moles of product generated for each mole of catalyst and therefore is a good measure of performance as well as overall stability. The turnover frequency (TOF) is the turnover number per unit time and therefore is reflective of the rate of product generation. These three values provide a good measure of how well a catalyst performs under operating conditions and provides a basic framework for comparison.

1.2.2. Heterogeneous Catalysts

'Heterogeneous catalyst' is the name given to nanoparticulate and bulk, metallic or semiconducting surfaces that are capable of driving catalytic reactions when provided with sufficient energy. Platinum is considered a benchmark proton reduction catalyst owing to its innate ability to balance the binding of protons and release of H₂ as outlined by the Sabatier principle.^{66,67} Unfortunately, the scarcity and consequently high cost of Pt excludes extensive applicability for solar H₂ generation. The development of computational methods for screening a vast range of possible alternatives has produced some interesting results that have encouraged the design of cheap, earth abundant catalysts.⁶⁸⁻⁷¹ In particular, a benchmarking study to examine hydrogen evolution catalysts (HECs) in different conditions revealed that a previously established NiMo alloy^{72,73} performed better than Pt but was not stable in long-term studies.⁷⁴ Interestingly, engineering of MoS₂ and development of methods to increase the exposed edge sites intrinsic to this semiconductor have enhanced catalysis and enabled it to

act as a stable coating for p-Si, showing that development of existing catalysts can have huge benefits in these applications.^{45,75–77}

A simple method for deposition of heterogeneous catalysts is through the photoreduction of metal salt precursors. Although less well-defined than direct deposition, this provides a very easy way of forming catalysts *in situ* and Pt,^{78–82} Ni,^{26,83,84} and Co^{26,85} catalysts have been effectively deposited using this method. It should be noted that although this often forms a heterogeneous catalyst, homogeneous molecular catalysts that remain in solution have also been reported. Extra care must therefore be taken to avoid ligand decomposition, and post-catalysis characterisation used to confirm the attachment of the heterogeneous catalyst.^{86,87}

One drawback to such systems is that determining the TON and TOF for heterogeneous catalysts is extremely difficult as the number of active sites is notoriously hard to define.⁷⁴ Furthermore, the catalytically active species or site can also be difficult to identify as the coordination around the metal, the formation and adaptation of oxides, and association and dissociation of species from external sources (e.g. electrolyte solution or substrate) can alter activity.

1.2.3. Molecular Catalysts

Synthetic molecular catalysts offer some clear advantages over heterogeneous catalysts. Precise control over chemical structure allows them to be tuned for optimal activity and selectivity, which becomes important when looking at multiple product generation for example in CO₂ reduction.^{88–92} Modification and subsequent performance analysis of molecular catalysts enables rational design for improvement of their ‘single site’ activity, with alterations to anchoring groups, metal centres, and primary and secondary co-ordination spheres being highly influential with regards to catalysis.^{56,93–97} Additionally, simple spectroscopic and/or electrochemical characterisation can be used to mechanistically study such species and reaction intermediates, extracting structure-function relationships and outlining development routes.^{98–102}

Among the most active and well-studied molecular proton reduction catalysts are a class of nickel (II) bis(diphosphine) complexes initially synthesised by DuBois and co-workers.¹⁰³ Exhibiting TOFs in excess of 100,000 s⁻¹, these catalysts represent some of the most active 3d-transition metal molecular catalysts for proton reduction.¹⁰⁴ A dominant feature responsible for such high activity is the presence of a pendant amine group in the secondary coordination

sphere, which facilitates proton transfer to the Ni centre, as well as stabilising H-H bond formation to assist H₂ generation.^{105,106} The structural functionality mimics that exhibited by [Fe-Fe]-hydrogenase, in which a bridging dithiolate ligand bearing a secondary amine shuttles protons to the active site (**Figure 1.4**).¹⁰⁷

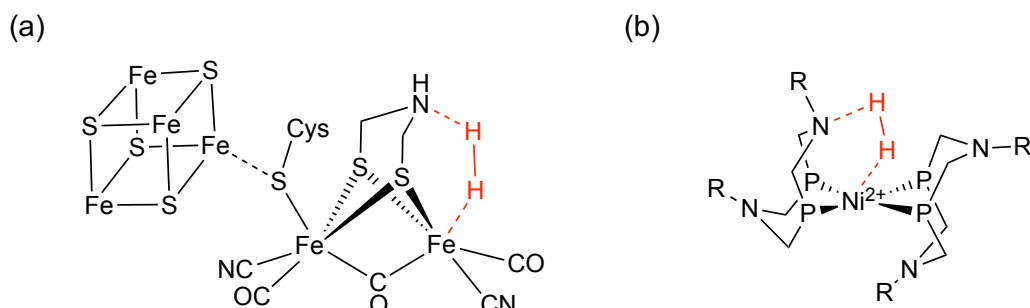


Figure 1.4 – The active site of a) [FeFe]-H₂ase and b) the Ni bis(diphosphine) class of molecular catalysts.

Although these electrocatalysts have predominantly been studied in organic solutions,^{103,108,109} functionalisation with phosphonic acid or amino acid residues enables aqueous solubility.^{96,97} One of the initial examples of photocatalysis using a DuBois-type catalyst in purely aqueous conditions was with a tetra-phosphonated derivative hereafter referred to as **NiP** (**Figure 1.5**), where the additional functionalisation enables anchoring to metal oxide surfaces, an essential feature for DSPEC, photocatalytic, and PEC systems.⁹⁷

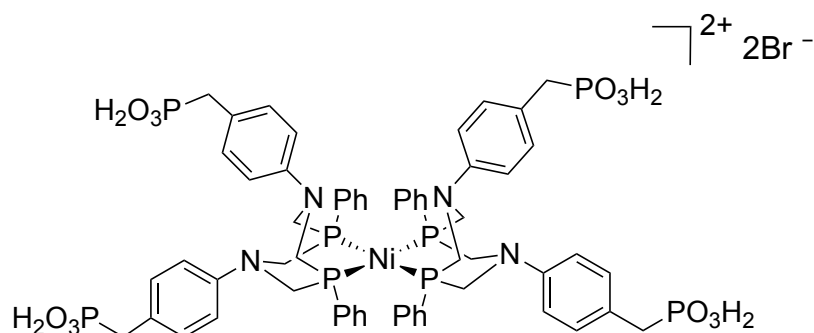


Figure 1.5 – Molecular structure of **NiP**.

The generally accepted mechanism for this class of catalyst involves consecutive reduction and protonation steps (in sufficiently acidic conditions), therefore the catalytically active state is correlated with the Ni^{I/0} transition, as has been demonstrated using cyclic voltammetry (**Figure 1.6**).^{97,110} It is important to note that the protonated species in these complexes can adopt two isomers: endo and exo, where the ‘pinched’ exo conformation is stabilised by intramolecular N-H...N hydrogen bonding. Experimental and computational studies suggest that H₂ generation only occurs with the endo configuration, as the H-H bond forms through

donation of a hydride from Ni, and a proton from the protonated pendant amine.^{110–113} The low overpotential requirement (200 mV), high stability, and high activity of **NiP** make it an ideal catalyst for immobilisation in DSPCs.

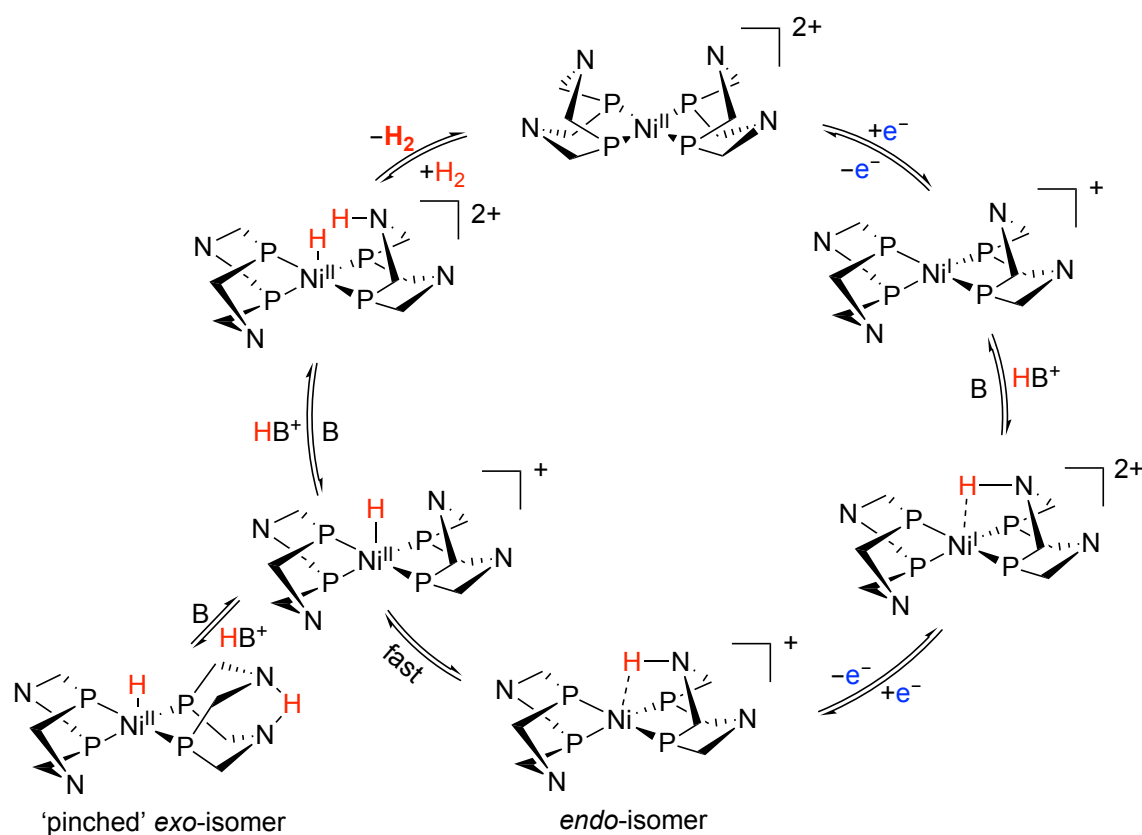


Figure 1.6 – Mechanism of H₂ generation with Dubois-type Ni catalysts. P and N substituents have been omitted.¹¹⁰

1.3. Photosensitisers

The role of a photosensitiser is to absorb light, creating long-lived excitons that permit charge transfer to a catalytic site. The desirable properties for an effective photosensitiser are: light absorption over a broad range of wavelengths; stability in aqueous solution; a high molar extinction coefficient; and sufficient thermodynamic driving force for charge transfer to a semiconductor or catalyst. This section introduces two common types: molecular dyes and quantum dots (QDs). Properties and characteristics of both are discussed with respect to photocatalytic and photoelectrochemical aspects.

1.3.1. Molecular Dyes

Light harvesting photosynthetic pigments in natural systems require numerous stacks of chromophores with specific light absorption, such as chlorophyll a and b, which shuttle excitons towards the reaction centre.^{8,9} Synthetic alternatives to such chromophores can be tailored to avoid the need for such large sequences, simplifying the process. Structural modifications to simple organic and inorganic chromophores can influence electronic properties, absorptivity, and stability, and also permit additional functionality such as surface anchoring groups and hydrophobic/hydrophilic units. For this reason, molecular dyes and their incorporation into solar-fuel-generating devices is highly practical.

DSPCs rely on hole injection from an excited dye to a p-SC and which typically occurs by a reductive quenching mechanism when a catalyst or acceptor species is present. Thermodynamically, successful hole injection relies on the dye's excited state reduction potential, $E_{(S^*/S^-)}$, being more positive than the valence band edge of the p-SC. The reduction potential of the reduced dye, $E_{(S/S^-)}$, must be sufficiently negative to reduce the acceptor species or catalyst. Kinetically, the performance is controlled by the rate of each charge-transfer step. Fast hole injection into the p-SC is required to generate the dye anion followed by rapid transfer of an electron to the catalyst to regenerate the ground state. The dominant charge recombination pathway between reduced dye/p-SC can be restricted by tailoring dyes for kinetically fast injection of holes and spatial removal of the LUMO from the p-SC.

The most well-studied inorganic dyes for solar energy conversion are derivatives of ruthenium tris-2,2'-bipyridine ($[\text{Ru}(\text{bpy})_3]^{2+}$; bpy = bipyridine).^{114,115} These dyes exhibit broad metal-to-ligand charge transfer (MLCT) bands, producing an excited state with the electron situated on the aromatic ligand and the hole at the metal centre.¹¹⁵⁻¹¹⁷ The long-lived excited state facilitates highly efficient electron transfer when coupled with n-SCs for photocatalytic,^{118,119} PEC,^{50,63,120} and DSSC applications.⁵² Incorporation of phosphonic acid-bearing Ru complexes with p-SCs has shown some degree of success,^{121,122} but fast charge recombination between the reduced sensitizer and holes in the p-SC valence band limits catalytic activity. Removing the electron in the reduced state (*i.e.* the ground state LUMO) from the p-SC surface can limit recombination, and positioning the HOMO adjacent to the anchoring group to ensure rapid hole injection has proven effective in systems incorporating dyes tailored specifically for p-SCs.^{49,61,123,124} Modifications to precious metal-containing dyes, including cyclometalated iridium (III) complexes¹²⁵⁻¹²⁷ and polypyridyl ruthenium (II) complexes,^{121,128-139} has been successful, however moving to organic dyes offers advantages.

Recent progress in engineering of organic dyes has increased efficiency, stability, and availability over their precious-metal-based counterparts, making them attractive low-cost alternatives.^{61,62,140} Unlike metal-based dyes, which tend to undergo MLCT transitions and weaker *d-d* transitions at the metal centre, organic dyes exhibit strong $\pi-\pi^*$ transitions giving them characteristically high molar extinction coefficients.^{62,141} Modification and immobilisation of triphenylamine,^{98,142–145} perylene monoimide (PMI),^{79,146–150} coumarin,^{151–153} and diketopyrrolopyrrole (DPP)-based dyes on p-SCs,^{80,124,154} has established a precedent for employment in DSPCs (**Figure 1.7**).

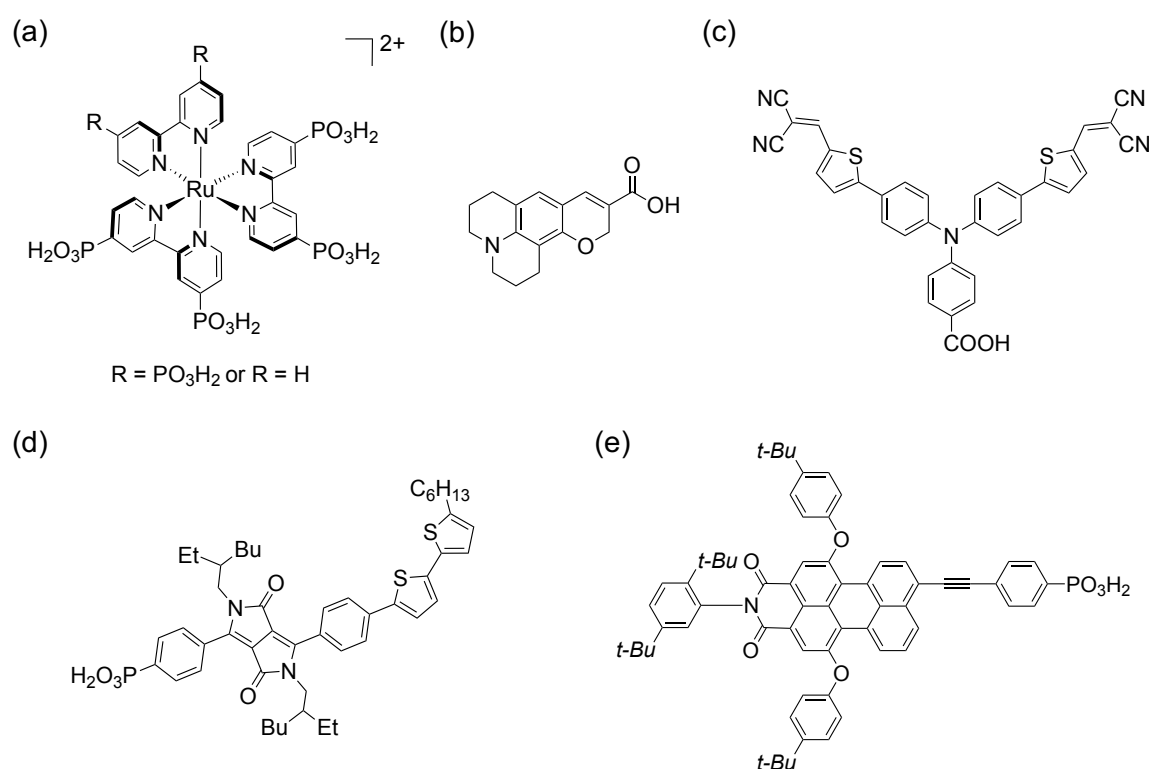


Figure 1.7 – Examples of a) $[Ru(bpy)_3]^{2+}$, b) coumarin, c) triphenylamine, d) diketopyrrolopyrrole, and e) perylene monoimide dyes.

DPP and PMI dyes in particular stand out as adaptable and highly applicable dyes. In the 1970s synthesis of the first DPP dye was reported.¹⁵⁵ Since then, established synthetic protocol and tuneable photophysical properties of DPP dyes through structural modifications has positioned them as attractive candidates in organic solar cells and organic field-effect transistors.^{156–161} DPP dyes have more recently shown promise in p-DSSCs,^{124,154,162–164} and have been successfully employed in dye-sensitised photocatalysis (DSP) systems with TiO_2 nanoparticles in conjunction with a molecular catalyst.⁸⁰ Thus far no reports of DSPCs featuring DPP dyes exist. However, features including ultrafast hole injection into NiO ,¹²⁴ and

a long-lived charge-separated state brought about by the inner electron acceptor unit,^{162,163} highlight them as attractive photosensitisers for coupling with molecular catalysts on p-SCs. PMI dyes have been employed in multiple NiO-based DSPCs.^{146–148,150,165,166} They are easily tailored and have recently been modified with a variety of different anchoring groups in DSP arrangements.⁷⁹ Additionally, PMI dyes are highly photostable, which motivates their implementation in DSPCs.

1.3.2. Quantum Dots

Colloidal nanocrystals offer several advantages over bulk semiconductors as they often exhibit large extinction coefficients and bandgaps that can be tuned through size and composition control.^{167–170} The tuneable bandgap is a consequence of quantum confinement, which is a phenomenon occurring when the particle diameter approaches the size of its exciton Bohr radius, creating discrete energy levels. Therefore, the optical and electronic properties of QDs lie somewhere between the classifications of continuous bands in crystalline materials and discrete orbitals for molecules.¹⁷¹

Solar fuel production can be achieved using these beneficial light-absorption and charge-separation properties. Additionally, control over the surface structure through simple modifications of capping ligands imparts catalytic flexibility, allowing for different reactions to be favoured or suppressed thereby influencing product selectivity.^{92,172–177}

The most commonly employed QDs in photocatalysis are transition metal dichalcogenides. These semiconductors are easily synthesised using various different methods, achieving high activities and good long-term stability in aqueous conditions. In particular, Cd-based QDs have demonstrated the highest activity for proton reduction, currently showing superior performance to Cd-free alternatives.^{57,92,178–180} Recently carbon materials have become more accessible and carbon nitride, carbon dots, and organic polymers have shown some clear success for H₂ generation, however their activity remains much lower than the corresponding Cd-based systems.^{22,78,181–186} ZnSe has also been established as a viable replacement but, until recently, H₂ generation was low with systems requiring Cd components to function effectively.^{187–189} ZnSe nanorods with a ligand-stripped surface were recently reported as highly active H₂-generating QDs.¹⁹⁰ The performance is competitive with Cd-based QDs without the requirement of a co-catalyst to function effectively. QDs have also been used as photosensitisers for wide-bandgap p-SCs, but as with photocatalysis, most systems rely on Cd components. Specific examples of such systems are discussed in Section 1.5.

1.4. Semiconductor Electrochemistry

The semiconductor plays a vital role in DSPCs as it is responsible for regeneration of the dye and ultimately enables holes to be transported away from the electrolyte solution, assisting productive catalytic reactions. The p-type conductivity is vital in directing charge transport and the properties of such semiconductors in aqueous solutions dictates their role in DSPCs. A brief description of semiconductor properties is outlined in the following sections, along with the key requirements for a p-SC in DSPCs.

1.4.1. Band Structure in Semiconductors

Solid crystalline materials are composed of multiple bonds between neighbouring atoms which form a periodic lattice structure. The nature of the bonding between these atoms and the composition of the lattice accounts for the electronic, mechanical, and optical properties in such materials. The combination of atoms to form molecular orbitals creates discrete energy levels that electrons can occupy. For the simplest case, two atoms combine to form a bonding and an anti-bonding orbital as described by the linear combination of atomic orbitals model, also referred to as tight binding theory due to the assumption that the atomic orbital is bound tightly to the nucleus.^{191,192} In a solid material, unlike in molecules, there are many atoms that combine to form molecular orbitals, with different assigned energies. The combination of all these orbitals in such a minute space warrants a low energy difference creating a so-called 'band' which can be thought of as a continuum of allowed energy states (**Figure 1.8**).

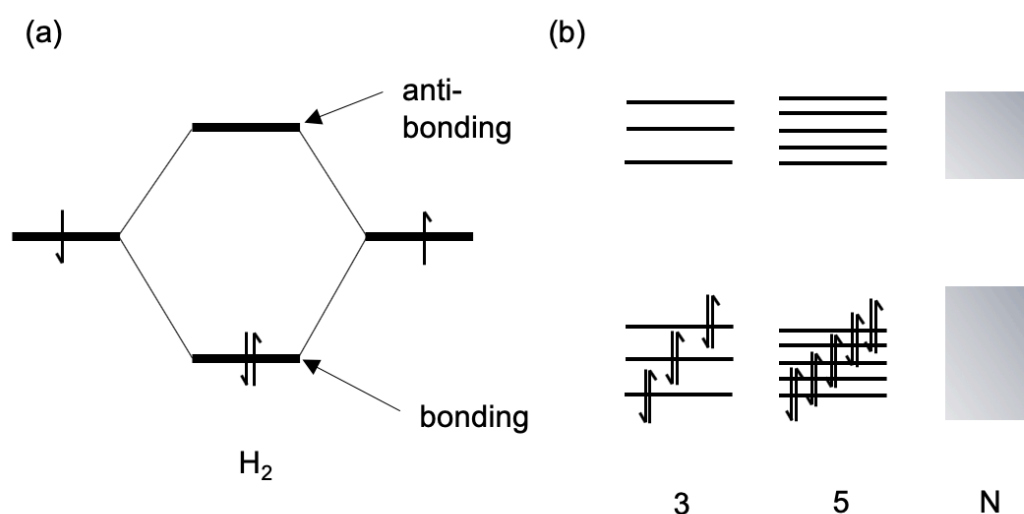


Figure 1.8 – Illustration of molecular orbital formation for a) the 2 atom case and b) 3, 5, and N atom cases.

In understanding band theory with respect to a semiconductor, it is more helpful to use Bloch's theorem. The theorem builds on the Drude-Sommerfeld model (also called the free electron model), which assumes that electrons can move freely through a metal as an 'electron gas', ignoring any interaction between ionic cores and electrons. The free electrons can be treated as travelling waves with additional 'particle' terms, therefore a mixture of quantum and classical methods define the dispersion relation for electrons (Equations 1.4 – 1.6, where h is Planck's constant, m is mass, v is velocity, p is momentum, λ is wavelength, E is the kinetic energy of electrons, and k is the wavevector).

$$\lambda = \frac{h}{p} = \frac{h}{mv} \quad (\text{Equation 1.4})$$

$$k = \frac{2\pi}{\lambda} \therefore k = \frac{2\pi}{h} p \quad (\text{Equation 1.5})$$

$$E = \frac{1}{2}mv^2 \therefore E = \frac{h^2}{8\pi^2m} k^2 \quad (\text{Equation 1.6})$$

Despite the Drude-Sommerfeld model being highly valuable in defining metal properties, it fails to account for insulating or semiconducting behaviour – for this reason, considering the periodic potential of a lattice is highly beneficial in understanding bands in semiconductors. Bloch's theorem describes how the periodicity of a lattice induces a potential energy profile with corresponding periodicity; this can be depicted by the solution to the Schrödinger equation (Equation 1.7), where the wavefunction (ψ) is periodic with the lattice (Equation 1.8). $u(r)$ is a function with the same periodicity as the crystal ($u(r) = u(r + T)$), in this case represented by a lattice translation, T .

$$\left[-\frac{\hbar^2}{2m} \nabla^2 + V(r) \right] \psi(r) = E\psi(r) \quad (\text{Equation 1.7})$$

$$\psi(r) = e^{ikr} u(r) \quad (\text{Equation 1.8})$$

Solving the Schrödinger equation with these conditions gives two regions of allowed wavefunctions: the filled lower energy valence band (VB), and the empty higher energy conduction band (CB) (**Figure 1.9**).¹⁹³ The curvature and direction of the bands is correlated with an effective electron mass (m^*) (Equations 1.9 – 1.10). A negative effective electron mass is representative of holes in the VB which behave as though they carry positive charge,

whereas a positive effective mass corresponds to CB electrons that behave as negative charge carriers. With respect to DSPCs, the VB and associated hole transport is the dominant factor. The variation in bands with different effective mass values can have a huge impact on the semiconductor properties as this parameter accounts for the band width as well as the position of the VB maximum and CB minimum. The effective mass is also related to the charge carrier mobility (μ), where higher mobility is observed with a lower effective electron mass, (Equation 1.11, where q is the charge and τ_c is the average time between collisions).¹⁹⁴

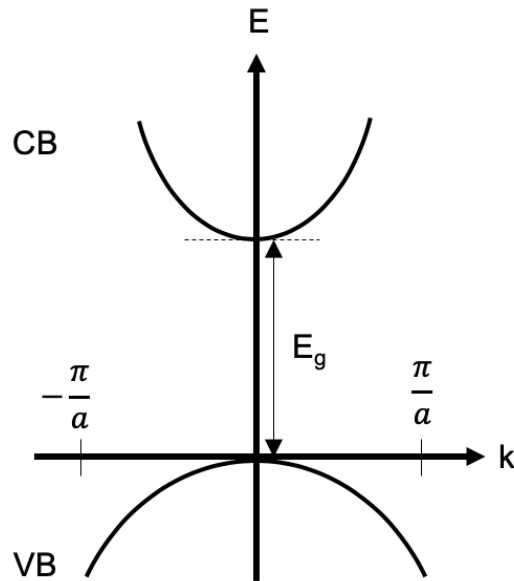


Figure 1.9 – Representation of CB and VB dispersion relations for a semiconductor. E = energy, E_g = bandgap, k = electron wavevector, a = lattice constant.

$$E = \frac{\hbar^2}{8\pi^2 m^*} k^2 \quad (\text{Equation 1.9})$$

$$m^* = \frac{\hbar^2}{d^2 E / dk^2} \quad (\text{Equation 1.10})$$

$$\mu = \frac{q\tau_c}{m^*} \quad (\text{Equation 1.11})$$

In the case where the k -vectors are directly aligned at $k = 0$, the semiconductor exhibits a direct bandgap. However, when the conduction band minimum does not align with $k = 0$, an indirect bandgap is observed, requiring the absorption or emission of a phonon to conserve momentum.^{192,193} Characterisation of materials using optical spectroscopy can confirm the nature of the bandgap.

The energy gap between the occupied band (VB) and the unoccupied band (CB) dictates whether a material will be conducting, semiconducting, or insulating. The hole or electron transport properties are defined by the band structure, which has an influence on photocatalytic reactions and kinetics of charge transfer processes. In photoelectrochemistry, the absolute positions of the VB and CB edges need to be taken into account with respect to thermodynamic driving force for a catalytic reaction or electron transfer process; this is discussed in more detail with respect to redox processes occurring at the semiconductor/solution interface in the next section.

1.4.2. Semiconductor/Electrolyte Solution Interface

Interfacing a semiconductor with aqueous solution induces several effects that are dependent on both the physical properties of the semiconductor and the composition of the solution it is in contact with. Most metal oxides will exhibit intrinsic n- or p-type conductivity due to oxygen vacancies or intercalation. For example, TiO₂ is n-type due to oxygen vacancies and reduced Ti ions that create donor levels close to the conduction band, whereas NiO exhibits p-type behaviour due to Ni²⁺ vacancies that are filled by oxygen atoms. The n- or p-type classification is imperative for understanding the nature of the semiconductor/electrolyte solution interface.

Electrocatalytic reactions at semiconductor surfaces can be heavily influenced by the ability of metal oxides to display band bending at an interface. The concept originates from the variation in electrochemical potential within a semiconductor due to charge transfer between itself and a solution-based species – **Figure 1.10** demonstrates this using a simplified band diagram for a p-SC.

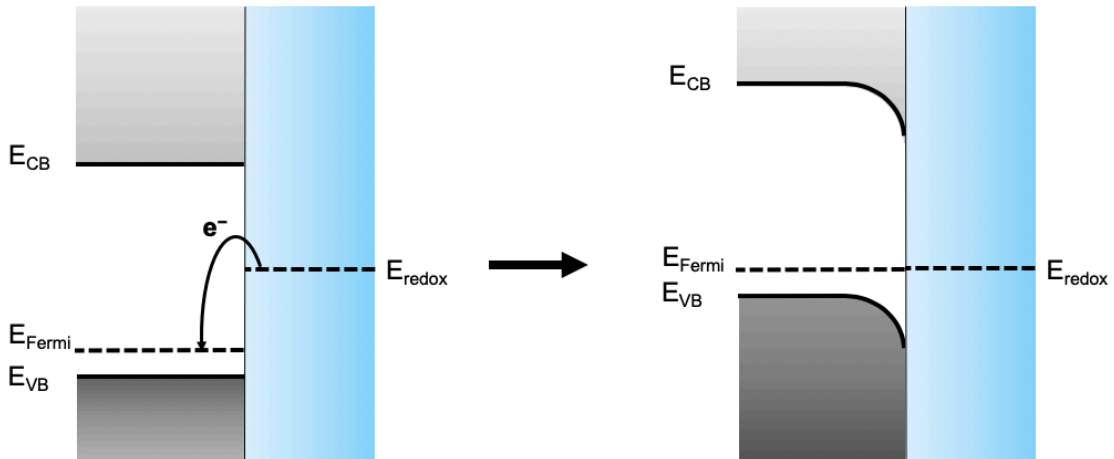


Figure 1.10 – Illustration of band bending exhibited by a p-SC when brought into contact with an electrolyte solution. E_{redox} is the redox potential of the solution species and E_{Fermi} is the Fermi level of the p-SC.

When the semiconductor is brought into contact with a redox species in solution, the whole system acts to equilibrate in order to reach the lowest energy configuration and to balance charge. Typically, the redox potential of the solution species is higher in energy than the Fermi level of a p-SC, therefore electrons are transferred from the solution to the semiconductor. The charge carrier density in the electrolyte tends to be much higher than in the semiconductor, so any change in potential falls predominantly across a region in the semiconductor – the space charge layer. The Helmholtz layer contribution, although still present, can effectively be ignored seeing as the capacitance in this region is so large that an induced potential drop will be minute compared to that in the space charge layer. The semiconductor surface is depleted of free carriers (in this case holes) through charge transfer, and this depletion layer grows until an equilibrium is reached. The width of the space charge region (W) is modulated by the donor density (N_d), the relative permittivity (ϵ_r), and the potential drop across the space charge region (ϕ_{sc}) of the semiconductor and is therefore material dependent (Equation 1.12).

$$W = \sqrt{\frac{2\epsilon_0\epsilon_r}{eN_d} \left(\phi_{sc} - \frac{kT}{e} \right)} \quad (\text{Equation 1.12})$$

For a p-SC, band bending assists the directional transport of electrons towards the interface due to the built-in electric field. Any excitation occurring in the space charge region will likely result in charge separation rather than recombination due to the fast movement of electrons and holes, whereas in the bulk, charges are more likely to recombine. Longer-lived electrons

are more likely to contribute to a catalytic reaction, in this case reduction, and therefore band bending enhances activity.

With regards to DSPCs, p-SCs are required for hole transport following injection from the immobilised dye. Gerischer's theory of interfacial electron transfer can be applied to DSPCs for understanding of the factors that control charge transfer between p-SCs and the dye species.¹⁹⁵ The theory relates the kinetic dependence of hole injection to the degree of overlap between the acceptor and donor species.^{196,197} In DSPCs, the photoexcited dye must have a distribution function that overlaps well with the density of states (DOS) in the p-SC located around the VB for fast hole transfer. The reduction potential of the dye in the excited and reduced state can be easily determined using cyclic voltammetry (CV) and UV-Vis spectroscopy, but the Fermi level of the p-SC, which is a good indication of the donor maximum of the DOS, is more difficult to obtain. One way to measure the Fermi level position is through Mott-Schottky analysis.

1.4.3. Mott-Schottky Analysis

Applying a bias to a semiconductor enables modification of the band bending within the space charge region. When a negative potential is applied to a p-SC, the bulk of the semiconductor is shifted cathodically with respect to the band edges; this is representative of the depletion condition. However, if the potential is pushed anodically, a point will be reached where the semiconductor displays no net band bending – this is the flatband potential (E_{fb}), indicating the Fermi level of the semiconductor (**Figure 1.11**). The E_{fb} value for a p-SC indicates the thermodynamic ability to accept holes from an immobilised or solution-based species and is therefore an important characteristic for DSPCs. The most reliable and commonly used method for determining E_{fb} employs electrochemical impedance spectroscopy (EIS).

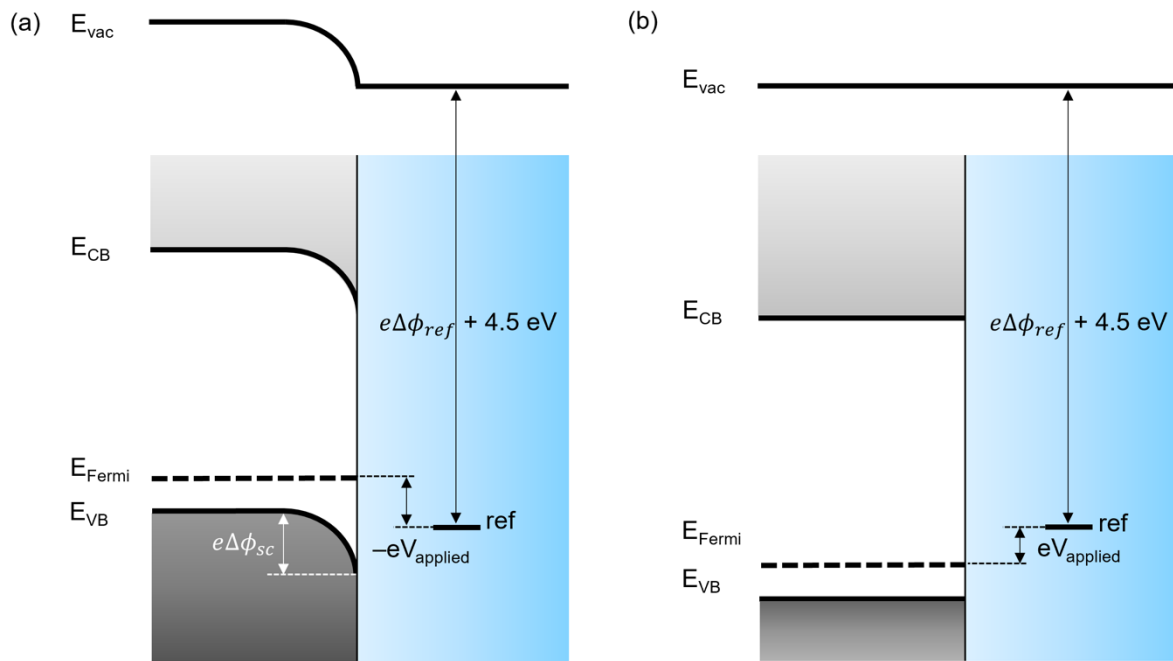


Figure 1.11 – Illustration of a p-SC under a) cathodic bias and b) anodic bias to reach the flatband condition. E_{CB} = conduction band, E_{VB} = valence band, E_{vac} = vacuum level, ref = reference electrode.

Impedance is the complex equivalent of resistance, in that it describes the relative ‘difficulty’ of an electric current to pass through a medium. An ideal resistor obeys Ohm’s law but real systems tend towards non-ideal behaviour in that they exhibit a resistance that is not independent of frequency and usually display an out-of-phase current response to an applied AC voltage (**Figure 1.12**).

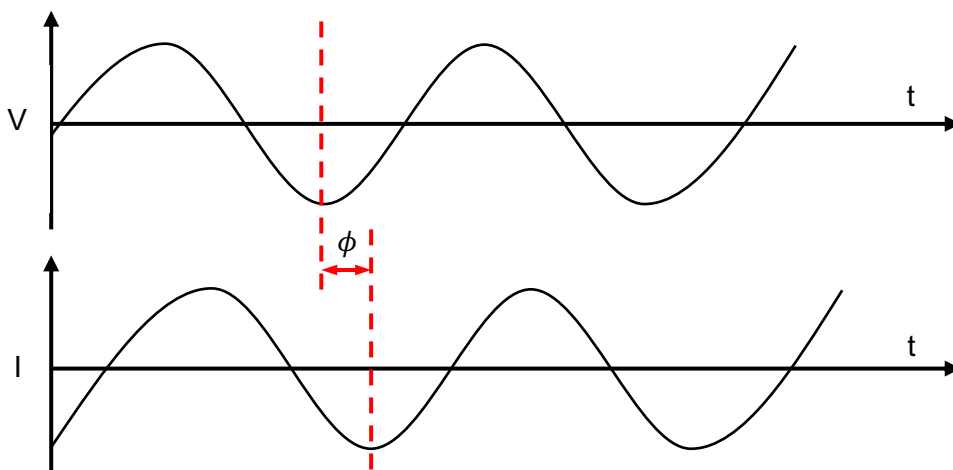


Figure 1.12 – Illustration of the phase lag between an AC voltage and the current response

The characteristic phase lag is advantageous as it provides a basis to construct a complex, time-dependent model for resistivity which manifests itself in impedance. For electrochemical systems, there is usually a non-linear response in current due to an applied potential and for this reason, a small perturbation signal (usually < 10 mV) must be chosen where the system will show a pseudo-linear response. The phase difference is used to form equations for the voltage and current at a defined time (Equations 1.13 – 1.14, where ω is the angular frequency ($2\pi f$)). Relating this back to the resistance of an ideal resistor gives an impedance equation (Equation 1.15, where Z is the impedance).

$$V_t = V_0 \sin(\omega t) \quad (\text{Equation 1.13})$$

$$I_t = I_0 \sin(\omega t + \phi) \quad (\text{Equation 1.14})$$

$$Z = \frac{V_t}{I_t} = \frac{(V_0 \sin(\omega t))}{(I_0 \sin(\omega t + \phi))} = Z_0 \frac{\sin(\omega t)}{\sin(\omega t + \phi)} \quad (\text{Equation 1.15})$$

Simplification using Euler's law (Equation 1.16) results in a full expression for the impedance with real and imaginary components (Equation 1.19).

$$\exp(j\phi) = \cos\phi + j\sin\phi \quad (\text{Equation 1.16})$$

$$V_t = V_0 \exp(j\omega t) \quad (\text{Equation 1.17})$$

$$I_t = I_0 \exp(j\omega t - \phi) \quad (\text{Equation 1.18})$$

$$Z = Z_0 \exp(j\phi) = Z_0(\cos\phi + j\sin\phi) \quad (\text{Equation 1.19})$$

Plotting the imaginary vs. the real component gives a Nyquist plot, which can be used for analysis with equivalent circuit modelling. An equivalent circuit that accurately represents the physical properties of a system must be chosen – this ensures that no additional circuit elements are used to fit the data.

Mott-Schottky analysis uses the variation of the impedance response with applied potential to extract the interfacial capacitance (C_{sc}) for an electrochemical system under steady state conditions. The flatband potential (E_{fb}) for a semiconductor can be obtained by plotting $1/C_{sc}^2$

against the applied potential (E_{app}) as described by the Mott-Schottky relation (Equation 1.20, where N_A is the acceptor density, A the interfacial area, e the electronic charge, ϵ the dielectric constant for the p-SC, ϵ_0 the permittivity of free space, T the temperature, and k_B the Boltzmann constant). For p-SCs a negative slope is obtained with the x -intercept being a good approximation of E_{fb} .

$$\frac{1}{C_{SC}^2} = \frac{2}{\epsilon\epsilon_0 A^2 e N_A} \left(E - E_{fb} - \frac{k_B T}{e} \right) \quad (\text{Equation 1.20})$$

1.4.4. Key Parameters for p-Type Semiconductors in DSPCs

Taking in to account the electrochemical properties of p-SCs in aqueous solution and their role in DSPCs, some requirements can be outlined:

- 1) A highly anodic VB position is desirable. The photocurrent onset is representative of the VB position as it marks the potential at which holes can be extracted, therefore the more anodic the VB, the earlier the photocurrent onset potential.
- 2) The conductivity should be as high as possible to facilitate light-driven charge transfer, therefore high mobility of holes is desired.
- 3) The bandgap should be sufficiently large to avoid visible light absorption.
- 4) The thickness must be tailored for efficient charge transport and high dye loading with minimal visible light absorption (Chapter 2, Section 2.4).
- 5) A mesoporous structure (pore size between 2 – 50 nm) is ideal to load significant amounts of the molecular species.
- 6) The p-SC should be relatively stable in aqueous conditions to avoid dissolution of metallic components that could contribute to catalysis.

1.5. Dye-Sensitised Photocathodes

1.5.1. Performance Evaluation

For molecular DSPCs there are some clear figures of merit that can be used as guidelines for comparison. Dynamic electrochemical measurements including linear sweep voltammetry (LSV) and CV can be coupled with light irradiation to show how the photogenerated current varies across a broad potential range. Such experiments provide a great deal of information about the DSPC, including the photocurrent onset potential; the maximum achievable photocurrent; and point to dark reactions from degradation and non-Faradaic processes.

Chronoamperometry experiments, where the applied potential is maintained at a constant value and the light chopped at regular intervals, are used to determine the steady-state photocurrent. Generally, the potential chosen reflects the point of highest photocurrent without significant degradation or contribution from the p-SC. The shape of the photocurrent response is influenced by characteristics of the p-SC, dye, and catalyst components, where interfacial charge build-up and recombination pathways are represented by transient spikes and slow increases in photocurrents upon light excitation.⁴⁹ Although effects from the separate interfaces are not easily distinguishable, qualitative information regarding limiting processes can be extracted through variation of different components.

In the presence of a SEA, these techniques can be used to determine the theoretical maximum achievable photocurrent for a specific dye/semiconductor arrangement. Such experiments remove the catalyst component so essentially probe only the dye/p-SC interface, providing the SEA chosen is easily reduced by the dye. However, this does not always accurately reflect the catalytic ability of the assembly due to differences in the thermodynamic and kinetic properties of the SEA and the catalyst. For true activity analysis, controlled potential photoelectrolysis (CPPE) must be used.

CPPE is a long-term chronoamperometry experiment under illumination and is followed by detection of products using gas chromatography or Clark-type electrodes. If H₂ generation is successful, a TON and TOF for the catalyst can be calculated as long as the amount of catalyst used can be accurately quantified. The Faradaic efficiency (FE) represents how much of the current extracted contributes to catalysis (Equation 1.21, where z is the number of electrons, F is the Faraday constant, $n_{product}$ is the number of moles of product generated, and Q is the charge passed). The FE indicates how stable and effective the DSPC is, as well as helping to identify contributions from dark current and side reactions that are not involved in catalysis. Unfortunately, with modestly performing systems a large portion of generated H₂ is likely to remain in solution, which cannot easily be accounted for even with long equilibration times – this therefore lowers the observed FE, TON, and amount of product generated if only sampling from the gas headspace.¹⁹⁸

$$FE(\%) = \frac{zFn_{product}}{Q} \times 100 \quad (\text{Equation 1.21})$$

Incident photon-to-current efficiency (IPCE) measurements are also a key test for DSPCs. Variation of the wavelength of monochromatic light with simultaneous photocurrent analysis at a fixed potential allows an IPCE spectrum to be obtained. The spectrum is representative

of the number of photons that contribute to photocurrent, and therefore supply electrons for catalysis. The plot should correspond with the absorption spectrum of the dye used for a DSPC. Equation 1.2.2 outlines the IPCE conversion for a given wavelength, where h is Planck's constant, c is the speed of light, e is the elementary charge, j is the photocurrent density, λ is the wavelength, and P is the light intensity.

$$IPCE(\lambda) = \frac{hc}{e} \cdot \frac{j(\lambda)}{\lambda P(\lambda)} \quad (\text{Equation 1.22})$$

Recombination routes can be evaluated by altering molecular and p-SC components. Photocurrent analysis with stepwise assembly gives indirect evidence for suppression or promotion of specific steps. Transient absorption and IR spectroscopy are valuable methods for direct extraction of rates of each charge transfer process and have been highly beneficial in outlining issues with DSPCs.

With these analytical tools, the performance of a given DSPC can be compared to other systems. Section 1.5.2 uses the figures of merit outlined here to detail some important progress in molecular DSPCs for H₂ generation in water.

1.5.2. Hydrogen Generating DSPCs

Research directed towards DSPC development originated in the DSSC community. In 1999, the first reported p-DSSC placed p-type NiO at the forefront as a practical photocathode semiconductor.¹⁹⁹ Despite successful development of NiO-based p-DSSCs, translation to DSPCs has been much less effective. A range of H₂-evolving NiO-based DSPCs have defined material problems such as low hole mobility, fast charge recombination between semiconductor and dye, and surface hole traps, which have restricted reports of high activity. Here, specific examples form a discussion of how alteration of molecular catalyst and photosensitiser units, as well as development of novel assembly methods and spectroscopic analyses, has highlighted the need for improved p-SCs.

Cobaloxime catalysts are the most commonly employed molecular catalysts in DSPCs, with the first example being formed through deposition of [Co(dmgBF₂)₂(H₂O)₂] (dmgBF₂ = difluoroboryldimethylglyoximate anion), on an organic triphenylamine dye-sensitised NiO.²⁰⁰ In this case, the lack of anchoring group for the catalyst led to fast desorption from the surface and deactivation of the system. A number of subsequent related co-immobilised dye/catalyst assemblies with cobaloximes featuring different anchoring groups,

permitted H₂ generation over much longer periods.^{144,201} However, the overall poor performance was attributed predominantly to material properties where the low thickness of the NiO layer, which is restricted by the effective diffusion length of holes, limited dye loading. A comparison of PEC activity with different NiO preparation methods using the unmodified cobaloxime deposition route further stressed the importance of high surface area and hole mobility in device performance.¹⁴⁵ Several covalently linked dye/cobaloxime-based complexes have been reported.^{142,202,203} The most notable progression was the development of a molecular dyad incorporating the more stable cobalt diimine-dioxime catalyst structure²⁰⁴ with a push-pull organic dye, achieving a photocurrent density of $-15 \mu\text{Acm}^{-2}$ when immobilised on NiO.¹⁴² Although a low FE was observed, this was attributed in part to Ni²⁺ reduction to Ni⁰, which was later confirmed for similar NiO systems.¹⁴⁷ Co-immobilisation of comparable but separate photosensitiser and catalyst units on NiO showed similar photocurrents to the dyad species suggesting that the co-assembly approach is feasible for DSPCs, avoiding the need for complicated synthesis steps.⁹⁸ The latter report also used spectroelectrochemical techniques to reveal the catalytically active species, observing a Co^I complex following illumination of the photoelectrode. A limitation of the co-assembled electrodes was attributed to issues with NiO, and a suggested route to improvement was the use of alternate p-SCs.

Bimetallic iron complexes have also revealed interesting phenomena about NiO-based DSPCs. Originating from an initial report detailing charge transfer between a coumarin dye and a co-immobilised mononuclear Fe-catalyst on NiO,²⁰⁵ a bimetallic Fe catalyst ([FeFe](mcbdt)(CO)₆; mcbdt = 3-carboxybenzene-1,2-dithiolate) was developed.²⁰⁶ In this system, fast hole injection from a photoexcited dye to the semiconductor (200 fs) and electron hopping to a catalyst (10 ps) was observed. Charge recombination between the reduced catalyst and the p-SC in this case was much slower (μs timescales) but not sufficiently slow to permit H₂ generation. Substitution for a similar Fe catalyst bearing a phosphonic acid anchoring group in place of the carboxyl group extended the reduced catalyst lifetime to ms, allowing the system to generate H₂, however catalyst degradation was observed suggesting the need for more stable catalysts.¹⁵¹ Recent mid-infrared transient absorption spectroscopy studies of the DSPC revealed that co-immobilisation is a valid strategy to form DSPCs provided a reductive quenching pathway is observed.¹⁵² Arrangement and packing of the dye and catalyst species on the surface alters the charge injection processes, and is therefore dependent on the morphology and surface structure of the p-SC used.

The most stable functional DSPCs are based on Dubois-type Ni catalysts. The first example using an immobilised Dubois-type catalyst with a naphthalene diimide dye failed to generate detectable H₂, a possible explanation being charge recombination between the catalyst and

NiO.²⁰⁷ We subsequently reported a layer-by-layer assembled photoelectrode, using a Zr^{IV} linker to connect a hexa-phosphonated ruthenium bipyridyl dye to a tetra-phosphonated [Ni(P₂N₂)]²⁺-based catalyst (**Figure 1.13**).¹²¹ Separation of the catalyst from the p-SC proved to be an efficient method to reduce charge recombination, enabling H₂ generation in aqueous conditions with up to $-8.8 \mu\text{A cm}^{-2}$ photocurrent at 0.0 V vs. RHE applied bias. The co-immobilised equivalent in this case produced approximately $-0.9 \mu\text{A cm}^{-2}$ photocurrent and did not yield any detectable H₂. The layer-by-layer method was subsequently used by Meyer and co-workers to develop an ITO-based photocathode with a tetra-phosphonated ruthenium dye and NiP, where a dianiline moiety was used to direct holes to the degenerate semiconductor surface.¹²² Introduction of donor and acceptor units on ITO allows charge to be directed depending on the assembly order and enables long-lived redox equivalents, as has been demonstrated with molecular species on ITO and NiO.^{208,209} Interestingly, charge transport through NiO was directed using a bilayer structure, where K⁺-doped NiO was formed and a Cu²⁺-doped overlayer, followed by an ITO inverse opal (IO) structure on which the molecular dye and catalyst were assembled with Zr^{IV}. Efficient hole transport generated photocurrents of approximately $-60 \mu\text{A cm}^{-2}$, emphasising how tailoring the semiconductor can positively influence activity.¹³⁷

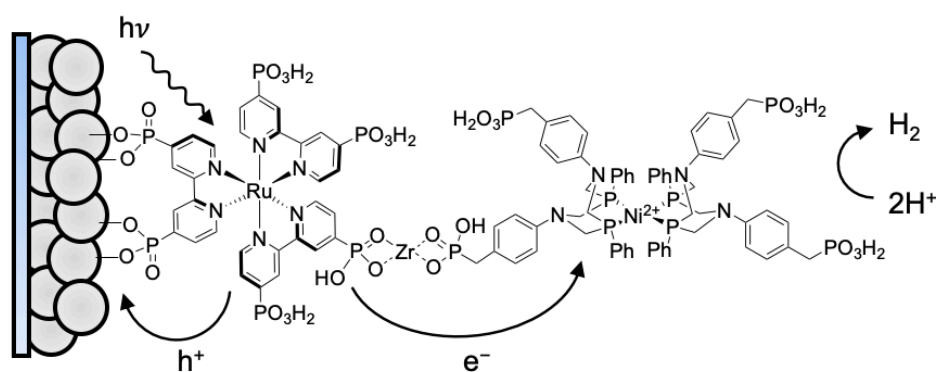


Figure 1.13 – Schematic of layer-by-layer assembly procedure used in a Dubois-type catalyst based DSPCs

DSPCs based on QDs have also been developed with varying degrees of success. CdSe has been successfully immobilised on NiO with a bimetallic Fe-dithiolate catalyst²¹⁰ and with a phosphonic acid-bearing cobaloxime catalyst to generate H₂.²¹¹ A recent study showed that in the cobaloxime-based system, hole transfer to the thiol-based capping ligand competed with catalysis thereby limiting efficiency.²¹² Molecular-catalyst-free CdSe systems have been successful, demonstrating that QDs can act as photocatalysts in DSPCs.^{213,214} However, there are currently no Cd-free examples of QD-based systems for H₂ generation.

1.5.3. Summary of Current DSPCs

The previous sections discussed the role of photosensitiser, catalyst, and semiconductor components in dye-sensitised solar fuel generation. There are benefits of tailoring dyes for p-SCs and organic dyes in particular possess favourable qualities that enable simple modification. Understanding how rates of charge injection and recombination depend on chemical structure and the interface with a p-SC, has led to appreciable developments with these systems. The immobilisation of QDs also shows some promise, as they are easily synthesised and are stable with high efficiency. However, the most efficient QDs currently consist of carcinogenic materials, necessitating replacement with less toxic components.

With respect to molecular catalysts, the most proficient systems are represented by stable species featuring robust anchoring groups as exemplified with the Dubois-type Ni catalysts. The higher performance is partly due to kinetically fast catalysis of these complexes, which limits recombination between the reduced catalyst and the p-SC. It is unclear at this stage if dyad systems are necessary for efficient hole hopping between dye and catalyst as recent spectroscopic findings suggest that charge transfer is proficient in co-immobilised systems.¹⁵² Kinetically limiting trap state mediated recombination between the reduced dye and the p-SC through passivation of NiO is one approach that has shown some success,^{215,216} and spatial separation of the catalyst from the surface works to limit catalyst/semiconductor recombination and enhances activity in NiO systems.¹²¹ However, switching to alternative p-SCs may alleviate these problems and permit high yields of H₂ with the synthetically less complex co-immobilisation approach.

Problems with NiO have become apparent through design and integration of functional devices, where spectroscopic findings have described issues relating to surface traps and fast recombination rates.²¹⁷ Despite these drawbacks, alternate p-SCs are underexplored due to the lack of easily accessible and simply derived materials with the required properties of transparency, p-type conductivity, mesoporosity, and a low-lying valence band. In this vein, exploration and assessment of new materials offers the opportunity to acquire knowledge that will direct future DSPC research. The work presented here will focus on establishing CuCrO₂ as a suitable alternative.

1.6. Delafossite CuCrO₂

Delafossite structures have been explored for direct PEC H₂ generation with narrow-bandgap CuFeO₂^{218–221} and CuRhO₂²²². However, these p-SCs are unstable under illumination in inert conditions, requiring O₂ to stabilise the Cu(I) sites against reduction to Cu(0). Wide-bandgap delafossite structures do not suffer from the same instability under solar illumination, as the excitation process is not permissible due to the insufficient energy supplied by visible light to excite electrons from the VB to the CB. The stability and lack of visible light absorption is advantageous for application in DSPCs.

One promising candidate has been explored as a replacement for NiO in p-DSSCs is CuGaO₂.^{223–225} However, so far devices have not shown appreciable improvement over the NiO analogues due to the low short circuit current densities achieved. One example of employment in DSPCs exists, where CuGaO₂ was functionalised with a precious metal-based Ru-Re dyad to enable CO₂ reduction.¹³⁹ In this system, similar photocurrents were observed for the analogous NiO DSPC but the shift in onset potential owing to the more anodic VB of CuGaO₂ enables tandem water splitting.

CuCrO₂ has also been employed in p-DSSCs^{226–230} and as a UV-active photocathode,^{231,232} but has not previously been developed as a DSPC. CuCrO₂ has however been studied extensively in the field of transparent conducting oxides (TCOs), where the intrinsic high hole mobility and conductivity set it apart from other delafossites.²³³ Furthermore, exploration in the field of TCOs has made properties and characteristics of films formed using various synthetic approaches readily available. CuCrO₂ is therefore a promising p-SC to consider for DSPCs.

CuCrO₂ is a wide-bandgap (~3.1 eV) p-SC which crystallises in the rhombohedral (3R) delafossite structure, which consists of infinite [CrO₂] layers of edge-shared [CrO₆] octahedra linked by linear O-Cu-O dumbbells (**Figure 1.14**).^{228,234} The p-type character derives mainly from Cu⁺ vacancies,^{234,235} and strong mixing between Cr 3d and O 2p states increases the covalent character of the valence band which accounts for a high intrinsic hole mobility.^{234,236} With such materials, the preparation method can have a huge influence on the presence of defects, intrinsic and extrinsic dopants, and surface structure. Additionally, the preparation method for NiO electrodes in DSPCs has been known to influence performance.¹⁴⁵ Surface area and transparency become additional factors when considering synthesis of p-SCs for DSPCs. Therefore, the synthetic procedure is a key consideration for development of CuCrO₂.

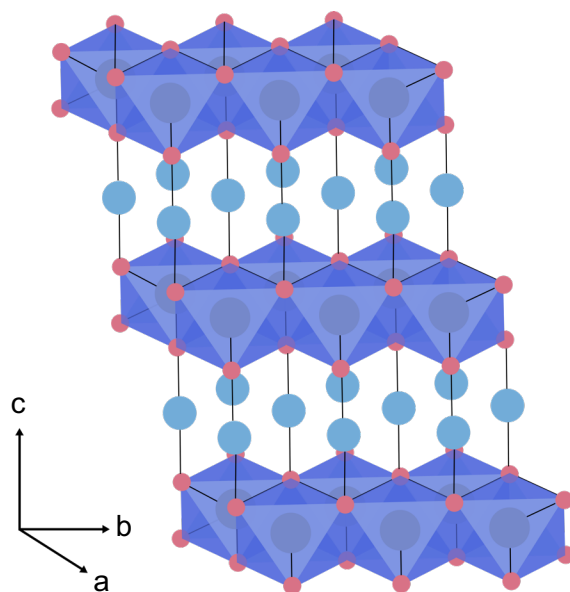


Figure 1.14 – Crystal structure of the 3R polytype of CuCrO_2 with Cu^+ sites connecting edge shared chromium oxide octahedra stacked along the c-axis. Light blue = copper, grey = chromium, red = oxygen.

Reports of synthetic routes to CuCrO_2 include: solid state reaction of oxide precursors;^{237,238} radio frequency magnetron sputtering;²³⁹ hydrothermal synthesis;^{228,240} and sol-gel synthesis.^{231,241,242} From a manufacturing perspective, the hydrothermal and sol-gel methods are preferred as solution-based processes present a scalable approach to production, with low-temperature synthetic methods being favoured over solid state reactions. From a practical viewpoint, these routes allow film stoichiometry to be easily controlled and nanostructured surfaces to be constructed with tuneable thicknesses, enabling optimisation of dye and catalyst loading.

In this thesis, sol-gel and hydrothermal routes are explored for the development of CuCrO_2 -based DSPCs. The two routes allow the CuCrO_2 structures to be manipulated in terms of thickness and morphology, permitting direct comparisons to be drawn between the different synthetic pathways.

1.7. Project Aims and Outline

The small number of functional H₂-generating DSPCs can be attributed to limitations with the most commonly employed p-SC – NiO – highlighting the need for substitution with a better-suited material. The aim of this thesis is to introduce CuCrO₂ as a novel DSPC material and to demonstrate PEC H₂ production from aqueous solution using immobilised molecular catalysts, QDs, and molecular dyes.

In Chapter 2, the development of sol-gel derived CuCrO₂ films and subsequent photosensitisation with an organic DPP dye and a Dubois-type nickel catalyst is presented as a novel route to H₂-generating DSPCs. Comparison is made with an analogous NiO-based photocathode to highlight the influence of material properties on the activity of the system as a whole. The delafossite photocathode is the first demonstration of H₂ generation with dye-sensitised CuCrO₂, offering a new p-SC for these applications.

In Chapter 3, recently developed ligand-stripped ZnSe nanorods are presented as Cd-free semiconductor nanoparticles to replace the molecular dye component in DSPCs. These QDs were immobilised on a CuCrO₂ electrode forming the first reported ZnSe-sensitised photocathode. The demonstration of photoelectrochemical H₂ generation highlights the versatility of CuCrO₂ in such systems.

In Chapter 4, inverse opal (IO) CuCrO₂ nanostructures were developed for immobilisation of two different organic dye species based on DPP and PMI cores. Two photocathodes, constructed through co-immobilisation of a molecular nickel catalyst with each dye, are used to establish the effect of structural differences on catalytic activity. A direct comparison is made with the sol-gel derived DSPCs constructed in Chapter 2 to provide a better understanding of the influence p-SC morphology has on activity. These next generation photocathodes provide insight into the influence of each component in co-assembled DSPCs.

Finally, in Chapter 5, significant findings are outlined, providing a framework for development of DSPCs. A general discussion of future prospects is given, identifying some key routes to alternative reactions and additional studies that could assist DSPC development in the future.

Chapter 2

Hydrogen Generation with Organic Dye-Sensitised CuCrO_2 and a Co-Immobilised Molecular Catalyst

*This chapter forms the basis of the following publication: C. E. Creissen, J. Warnan and E. Reisner, Solar H_2 generation in water with a CuCrO_2 photocathode modified with an organic dye and a molecular Ni catalyst, Chem. Sci., 2018, 9, 1439-1447. All experiments were conducted by the author with the exceptions stated here. **DPP-P** was synthesised by Dr. Julien Warnan and **NiP** was synthesised by Dr. Benjamin Martindale.*

2.1. Introduction

Chapter 1 introduced dye-sensitised photoelectrochemical (DSPEC) cells as solar fuel-generating devices that can overcome instability and high cost associated with p-type semiconductors (p-SCs) employed in conventional PEC cells.^{48–50,243} Hybrid photocathodes, based on stable wide-bandgap semiconductors featuring surface-anchored molecular catalysts and dyes, offer a modular platform for solar fuel generation. Simple and scalable procedures for the synthesis of each component enhances their applicability and accessibility, creating an inexpensive route to device fabrication. Considerable progress has been made in the development of dye-sensitised photoanodes,^{48,50,62–64} however corresponding dye-sensitised photocathodes (DSPCs) are currently restricted by choice of p-SC, with the majority of reports being based on NiO. Although stable and easily synthesised,^{145,199,244–247} NiO suffers from drawbacks such as low hole mobility and fast charge recombination between holes in the valence band (VB) and the reduced sensitiser.^{217,248,249} These properties ultimately limit overall device performance and have so far prevented reports of high photocurrent densities and significant turnover numbers for the catalyst.^{250–253}

DSPCs operate through rapid hole injection from a dye species to the p-SC, followed by reduction of the catalyst. A molecular catalyst is immobilised on the p-SC or covalently linked to the dye to facilitate the catalytic reaction. Typically, DSPCs undergo a reductive quenching mechanism with immobilised photosensitisers, whereby the initial step of photoexcitation of the dye is followed by hole injection into the p-SC, creating a reduced dye that can subsequently transfer an electron to the molecular catalyst (**Figure 2.1**). Metal oxides are attractive as p-SCs for two reasons: 1) they are easily synthesised using solution processing techniques; and 2) their surface is easily functionalised with molecules featuring compatible

anchoring groups, facilitating efficient charge transfer. Transport of charge through the p-SC film and the ability to accept photogenerated holes depends on the physical characteristics of the material. High hole mobility throughout the film, low light absorption, and a thermodynamically accessible VB, are highly beneficial qualities for a p-SC.

In this study, delafossite CuCrO_2 is proposed as a novel DSPC material. Interfacing this p-SC with an organic visible-light-harvesting diketopyrrolopyrrole (DPP) dye and a molecular Ni proton reduction catalyst highlights the important role of semiconductor development for H_2 -generating DSPCs. Sol-gel synthesis and characterisation of CuCrO_2 is presented as a simple route to construction of CuCrO_2 electrodes. Co-immobilisation of the dye and catalyst species, and photoelectrochemical (PEC) characterisation of the photocathode with comparison to a corresponding NiO photocathode, highlights the semiconductor's influence on PEC H_2 production.

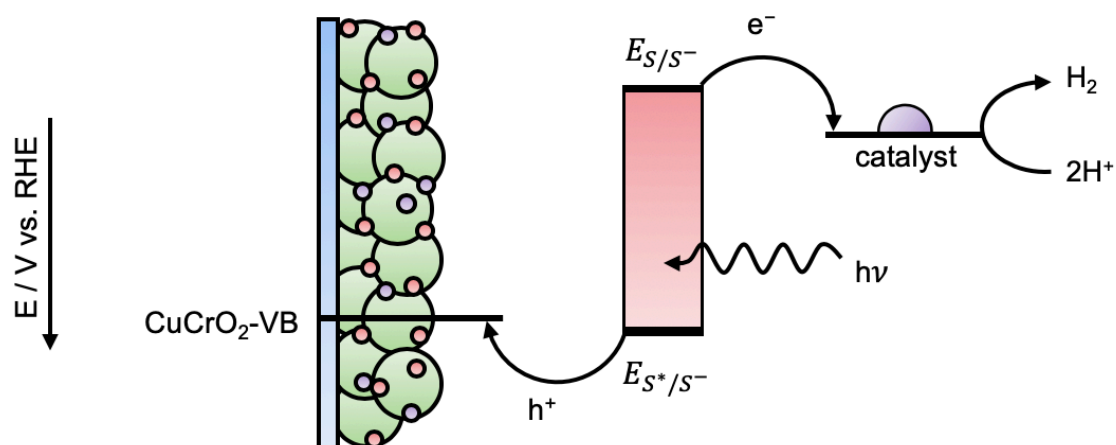


Figure 2.1 – Illustration of the reductive quenching pathway for a DSPC, where h^+ = holes, e^- = electrons, S = the dye species, E = electrochemical potential, and VB = valence band.

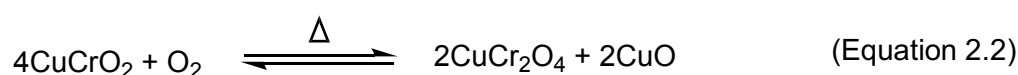
2.2. CuCrO_2 Synthesis and Physical Characterisation

Sol-gel processing is a wet-chemical method used to synthesise materials at relatively lower temperatures than corresponding solid-state reactions. In a typical sol-gel synthesis, a solution composed of a colloidal suspension of metal precursors undergoes hydrolysis and condensation reactions to form a sol with dispersed particulates. The sol can be deposited on a substrate, where gelation occurs to generate a thin-film upon evaporation of the solvent. Subsequent heating in air acts to remove any organic precursors used and crystallises the amorphous material. The advantages of forming films through this method include good

control over the stoichiometry, low-temperature synthesis, and the use of inexpensive precursors, making it a commercially practical technique for metal oxide development.^{254,255}

A previously reported sol-gel method was adopted to synthesise CuCrO₂ films directly on Indium Tin Oxide- (ITO-) coated glass (see experimental section for full details).²⁴² Cu(acetate)₂·H₂O was initially dissolved in EtOH with triethanolamine (TEOA), which acts as a chelating agent. Cr(NO₃)₃·9H₂O was subsequently added to form the precursor sol. Local heterogeneity in films often arises from faster reaction of one component over another. In this case, faster dissolution and reaction of the copper salt over the corresponding chromium salt is inhibited by the addition of TEOA, which also acts to enhance the solubility of the copper acetate precursor in EtOH.

The precursor sol was spin-coated on ITO-coated glass, followed by annealing in air (400 °C) to generate a mixture of CuO and CuCr₂O₄ (Equation 2.1). Subsequent annealing at 600 °C in inert atmosphere was required to obtain CuCrO₂ films, as heating in the presence of oxygen promotes the formation of spinel phase CuCr₂O₄, negatively impacting performance (Equation 2.2).²²⁸ Films with high crystallinity, mesoporous structure, and controllable thickness were obtained using this method.



The rhombohedral delafossite structure (space group $R\bar{3}m$) was confirmed using X-ray diffraction, where only pure phase CuCrO₂ was detected excluding significant spinel phase formation (**Figure 2.2**). Preferential crystallisation along the c-axis was observed resulting in the enhanced (00 l) peak. CuCrO₂ films synthesised using this method displayed a direct bandgap of 3.1 eV, as estimated from a Tauc plot (**Figure 2.3**).

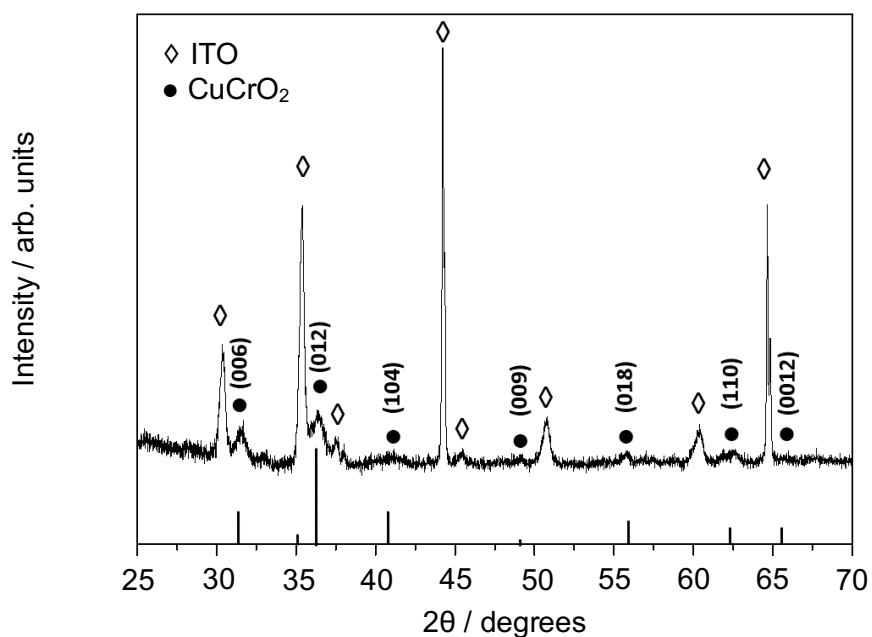


Figure 2.2 – XRD pattern for a 500 nm thick CuCrO_2 electrode where diamonds represent peaks from the ITO-glass and dots peaks from CuCrO_2 . Reference pattern shown for comparison (black lines, ICSD collection code 026676).

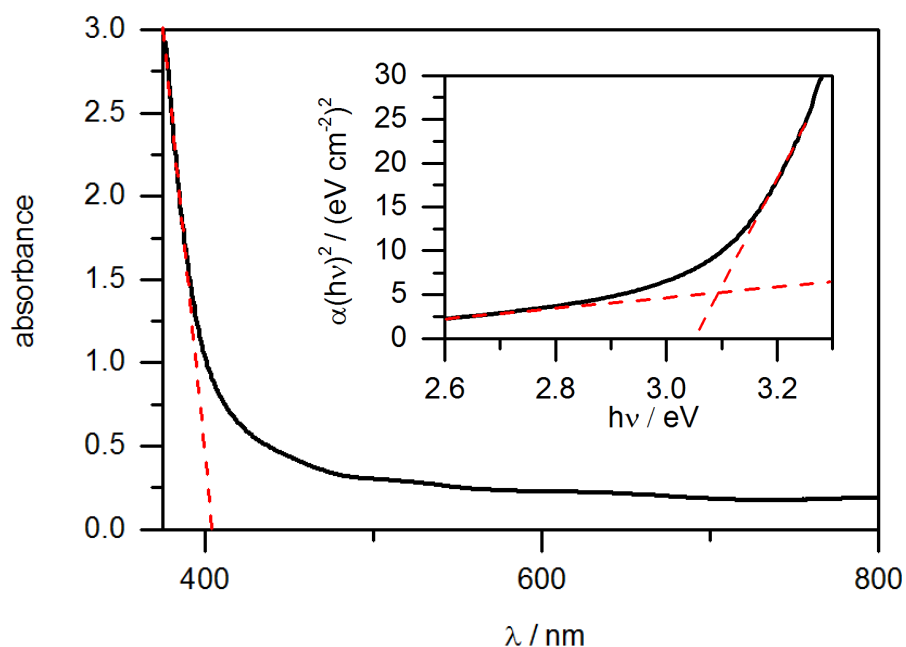


Figure 2.3 – UV-Vis spectrum obtained in transmission mode and Tauc plot (inset) of a 500 nm thick CuCrO_2 electrode with the ITO-glass background subtracted.

Scanning electron microscopy (SEM) images revealed a mesoporous surface structure consisting of nanorods of length 73 ± 17 nm and thickness of 21 ± 4 nm, giving an average pore diameter of 17 ± 5 nm. The thickness of the films can be tuned by altering the number of layers deposited. Here, structures with 3, 6, and 9 layers were formed, corresponding to 300, 500, and 700 nm thick films respectively (**Figure 2.4**). 700 nm thick films showed a less defined structure which likely arises from partial flaking or poor intercalation of the sol-gel precursor following consecutive spin coating steps. N_2 gas adsorption isotherms displayed type-IV behaviour, as is expected for mesoporous structures, and gave a Brunauer-Emmett-Teller (BET) surface area of $25 \text{ m}^2 \text{ g}^{-1}$. NiO films typically display a higher BET surface area in the range of $50 - 75 \text{ m}^2 \text{ g}^{-1}$, which indicates that higher dye loadings can be obtained.¹⁴⁵ For comparative studies, NiO films were prepared using a previously reported hydrothermal synthesis.¹²¹ With NiO, a film thickness of $2 \mu\text{m}$ was used, which gave the highest photocurrents following dye sensitisation. Therefore, although not identical in terms of dye loading or surface structure, the best performing NiO system is presented. The comparison is made between each individually optimised photocathode featuring the same surface-immobilised species.

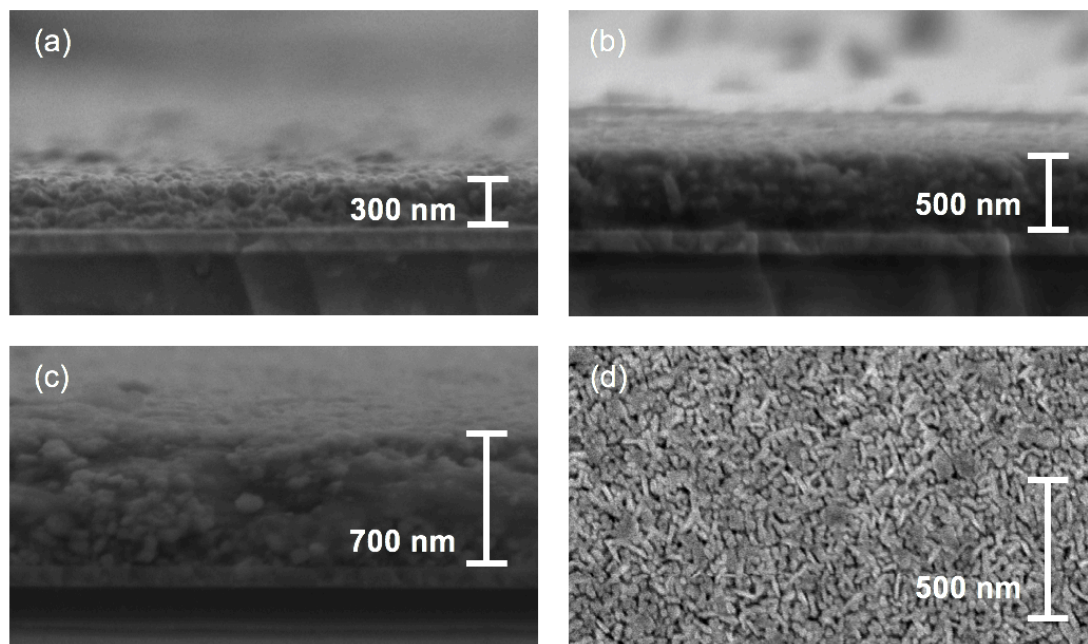


Figure 2.4 – Cross-sectional SEM images of a) 300 nm, b) 500 nm, and c) 700 nm CuCrO_2 electrodes, d) a top down image of a 500 nm CuCrO_2 film.

2.2.1. Mott-Schottky Analysis

For successful dye regeneration, a thermodynamically accessible VB is required. The flatband potential (E_{fb}) of a p-SC denotes the potential of the Fermi level with respect to a reference electrode. The E_{fb} is therefore reflective of the thermodynamic ability of a semiconductor to accept holes from a solution-based or immobilised species. The E_{fb} value also dictates the photocurrent onset potential for the p-SC, an important consideration with respect to the development of tandem DSPEC cells. Mott-Schottky analysis is a common method for E_{fb} determination with stable semiconductors and was employed here for characterisation of CuCrO_2 (for further explanation of electrochemical impedance spectroscopy and Mott-Schottky analysis, please refer to Chapter 1, Section 1.4.3). A modified Randles circuit featuring a constant phase element was used to fit obtained Nyquist plots. The negative slope indicates p-type behaviour and the x -intercept is equal to $E_{fb} + k_B T/e$, giving a flatband value of +1.0 V vs. RHE (**Figure 2.5**). NiO under the same conditions displayed an E_{fb} of around +0.75 V vs. RHE,¹²¹ therefore the onset potential for CuCrO_2 should be earlier than that of NiO , as the E_{fb} value is approximately 250 mV more positive.

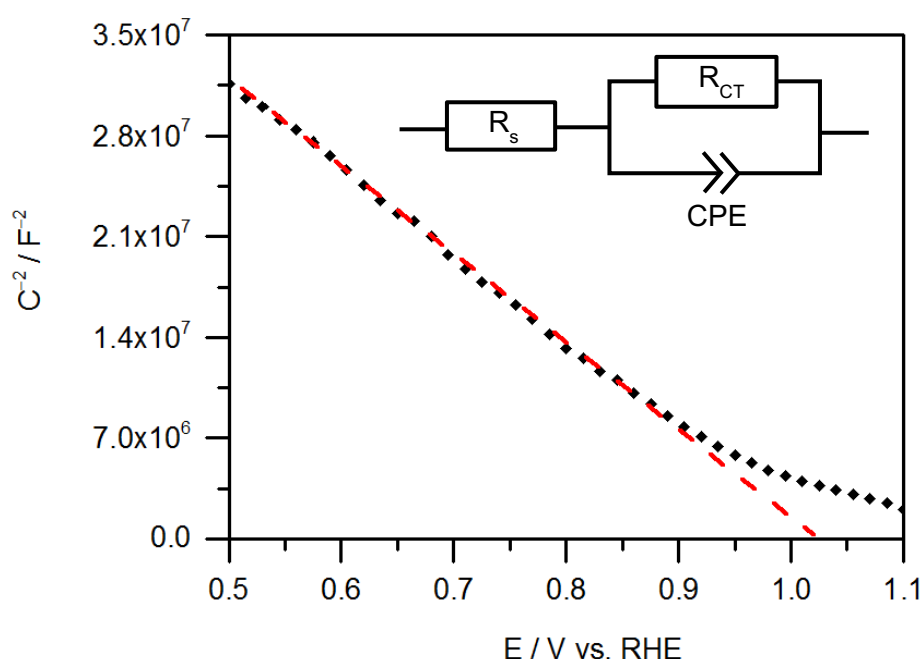


Figure 2.5 – Mott-Schottky plot of a CuCrO_2 (500 nm) electrode conducted in aqueous Na_2SO_4 (0.1 M, pH 3) at room temperature. R_s is solution resistance, R_{CT} charge transfer resistance, and CPE represents a constant phase element.

2.3. Molecular Components

2.3.1. Organic Dye Properties

Incorporation of organic dyes in p-DSSCs,^{61,124,154,162,164} colloidal systems,^{79,80} and DSPCs,^{98,142,144,151,152,200,202,205–207} has proven successful, highlighting their ability to function as stable and powerful light absorbers. A DPP dye, **DPP-P (Figure 2.6)**, was chosen as the photosensitiser for CuCrO₂. DPP chromophores are highly photostable organic species that are easily synthesised and modified.^{156–159,162} Their high capacity to absorb visible light and accessible reduction potential in the excited state makes them good candidates for coupling with p-SCs, on which they have been known to exhibit ultrafast hole injection (fs timescale).¹²⁴ **DPP-P** exhibits a strong visible light absorption ($\epsilon_{496\text{ nm}} = 2.6 \times 10^4 \text{ M}^{-1} \text{ cm}^{-1}$, DMF) owing to the DPP core and additional structural modifications. Side chains featuring alkyl groups act to limit aggregation (green), the phosphonic acid anchoring group electronically couples the dye to the semiconductor (blue), the thiophene units increase conjugation and close the bandgap allowing absorption of a large portion of the solar spectrum (purple), and the hydrophobic tail reduces aqueous solubility, preventing dissociation to solution (orange). The bicyclic lactam ring acts as an internal acceptor, spatially removing the LUMO from the anchoring point at the p-SC surface.²⁵⁶ This feature acts to limit recombination between the reduced dye with holes in the VB of the p-SC, as has been shown previously with similar DPP derivatives on NiO (**Figure 2.6**).¹²⁴

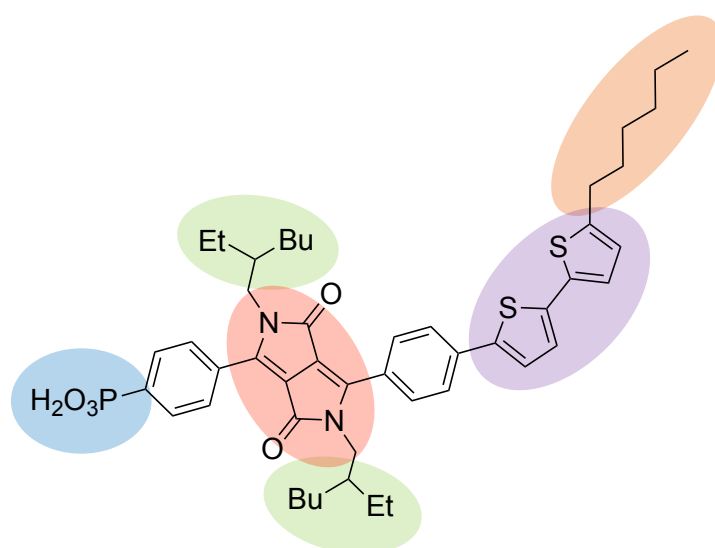


Figure 2.6 – Molecular structure of **DPP-P** with important structural features highlighted.

In the proposed reductive quenching pathway, the excited dye **DPP-P*** is initially reduced by hole injection into the semiconductor. Then the reduced species, **DPP-P⁻**, is oxidised by the catalyst or a solution-based acceptor to regenerate the dye. The excited state reduction potential ($E_{(S^*/S^-)}$) of +1.57 V vs. RHE allows the excited dye to inject holes into the VB of CuCrO₂. The oxidation potential for the reduced dye ($E_{(S/S^-)}$) of -0.7 V vs. RHE provides a high driving force for reduction of an immobilised catalyst.

2.3.2. Molecular Catalyst Properties

To form a functional system that is not limited by diffusion of a catalyst in solution and to avoid the need for a sacrificial electron acceptor, an immobilised molecular catalyst is required. The catalyst chosen in this study was **NiP (Figure 2.7)**, a Dubois-type molecular Ni catalyst based on the nickel (II) bis(diphosphine) ($[\text{Ni}(\text{P}_2\text{N}_2)_2]^{2+}$) core, featuring four phosphonic acid anchoring groups (see Chapter 1, Section 1.2.3 for further details). **NiP** has been employed as an immobilised proton reduction catalyst in several DSPCs and with TiO₂-coated narrow-bandgap photocathodes displaying good performance and stability in all cases.^{47,121,122,137,257} The overpotential for the second reduction of the nickel centre to a catalytically active state occurs at -0.21 V vs. RHE,⁹⁷ therefore **DPP-P⁻** exhibits sufficient thermodynamic driving force to reduce the immobilised catalyst. Effective turnover requires two electrons from excited dye species to be successfully transferred to the catalyst.

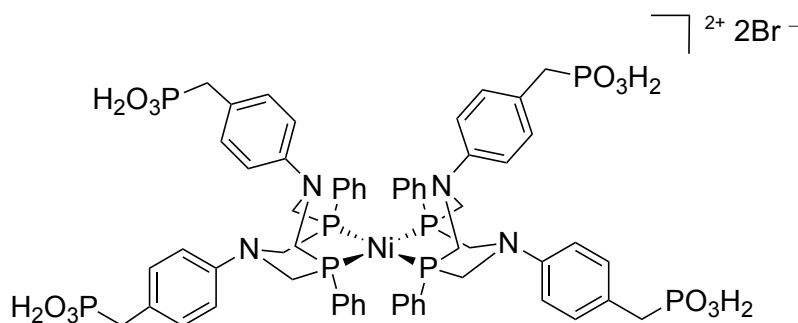


Figure 2.7 - Molecular structure of the catalyst **NiP**.

As outlined in Chapter 1, co-immobilisation of a molecular proton reduction catalyst presents a desirable route to H₂ generation. Current systems relying on NiO have struggled to generate H₂ in a co-immobilised arrangement owing to recombination between the reduced catalyst and the semiconductor.^{151,205–207} The problem has forced research towards the development of synthetically complicated dyad structures, limiting the availability of DSPC

arrangements.^{99,142,258} In this study, NiO and CuCrO₂ photocathodes were formed through a simple co-immobilisation route to emphasise the influence of the p-SC in DSPCs.

The interface between the dye and semiconductor is initially evaluated using a diffusional electron acceptor to act as a 'model catalyst' without significant kinetic constraints. Subsequent immobilisation of the molecular catalyst provides a working system. The step-by-step assembly and analysis provides information about the separate components and their individual interaction with the p-SC surface.

2.4. Photoelectrochemistry of DPP-P Immobilised on CuCrO₂

CuCrO₂|DPP-P electrodes were prepared by soaking CuCrO₂ in a DPP-P solution (1 mM, DMF) for 15 h. Immobilisation of the dye was confirmed by the colour change and verified using UV-Vis spectroscopy, which displays a clear absorption maximum at 500 nm, consistent with the electronic transition exhibited by DPP-P (Figure 2.8).

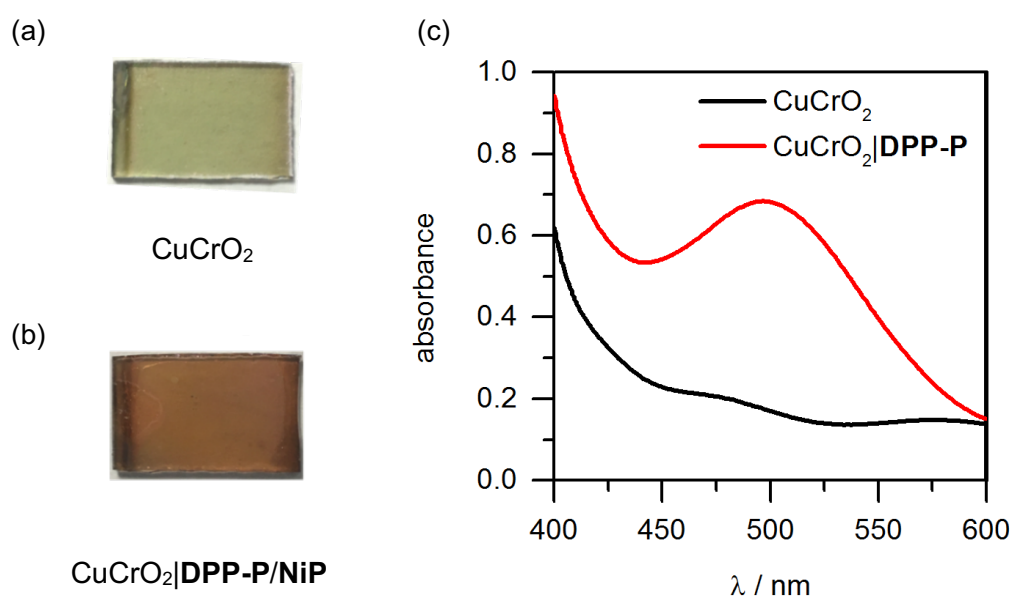


Figure 2.8 – Photographs of a) CuCrO₂ and b) CuCrO₂|DPP-P/NiP films, c) transmission UV-Vis spectrum of CuCrO₂ (black) and CuCrO₂|DPP-P (red) electrodes (ITO-glass background subtracted).

To assess the PEC compatibility of DPP-P with CuCrO₂, a sacrificial electron acceptor (SEA) was used. 4,4'-dithiodipyridine (DTDP) was chosen as it has a readily accessible reduction potential in aqueous solution ($E_{\text{red,DTDP}} = -0.06$ V vs. RHE) and undergoes rapid reduction.

DTDP therefore allows **DPP-P**⁻ to easily transfer electrons to regenerate the ground state. Using a SEA limits charge recombination between the dye and semiconductor by enabling fast electron transfer and prevents substantial reductive dye decomposition, which occurs in the absence of an electron acceptor. These tests therefore provide a good estimate of the maximum attainable photocurrent for a given photocathode.

Photocurrent analysis was conducted with 300, 500, and 700 nm thick electrodes using DTDP (5 mM in 0.1 M Na₂SO₄, pH 4.6). Chronoamperometry measurements showed that **DPP-P** is capable of efficient light-mediated hole transfer to CuCrO₂ and **DPP-P**⁻ can reduce DTDP as exemplified by the cathodic photocurrent (**Figure 2.9**). The optimal thickness giving highest photocurrents was 500 nm ($j \approx -160 \mu\text{A cm}^{-2}$ at 0.0 V vs. RHE), whereas the 300 and 700 nm thick electrodes both resulted in lower photocurrents ($j \approx -50 \mu\text{A cm}^{-2}$ and $j \approx -40 \mu\text{A cm}^{-2}$ at 0.0 V vs. RHE respectively). For comparison, a NiO electrode sensitised with **DPP-P** obtained photocurrents of $j \approx -80 \mu\text{A cm}^{-2}$ at 0.0 V vs. RHE. The higher photocurrents suggest that CuCrO₂ is able to extract holes more effectively than NiO, suggesting that CuCrO₂ is less susceptible to recombination between the reduced dye and holes in the semiconductor as has been observed in previous reports.²²⁶

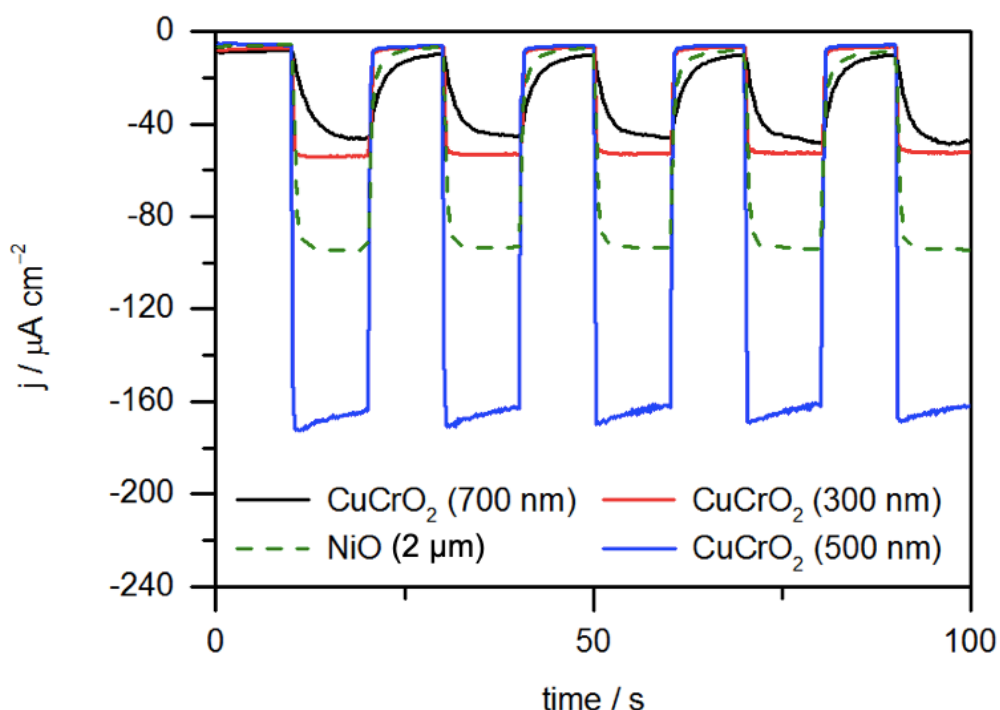


Figure 2.9 – Chronoamperometry analysis with **DPP-P**-sensitised electrodes under chopped light illumination (100 mW cm^{-2} , AM 1.5G, $\lambda > 420 \text{ nm}$) in the presence of DTDP (5 mM in 0.1 M Na₂SO₄, pH 4.6). Applied potential = 0.0 V vs. RHE, electrode active area of 0.25 cm^2 was used in all cases.

The optimal thickness is rationalised by considering the effective hole diffusion length (L) at a given applied potential, which is related to the hole diffusion coefficient (D) and hole recombination lifetime (τ_r) as described by Equation 2.3.^{259,260} Assuming the generally accepted trapping-detrapping model for n-type DSSCs, a simplified relation between the film thickness (d) and the hole transport time (τ_{tr}) can be drawn; the factor of 2.35 arises from geometry dependent contributions to diffusion (Equation 2.4).^{261,262} Combination of these two equations gives Equation 2.5. For efficient hole transport, the effective diffusion length must be greater than the thickness.

$$L = \sqrt{D\tau_r} \quad (\text{Equation 2.3})$$

$$D = \frac{d^2}{2.35\tau_{tr}} \quad (\text{Equation 2.4})$$

$$L = \sqrt{\frac{d^2\tau_r}{2.35\tau_{tr}}} \quad (\text{Equation 2.5})$$

Three interdependent factors are responsible for steady state photocurrent generation: 1) charge collection efficiency (η_{cc}); 2) light harvesting efficiency (η_{LH}); and 3) electron injection efficiency (η_{inj}).^{263,264} With dye-sensitised systems η_{inj} depends on the electronic coupling and η_{LH} is dependent on the absorption coefficient (α) of the dyed film, so both are dependent on the dye structure. η_{cc} approaches 100% for values of $L \gg d$, so low values of d are ideal to efficiently extract holes. However, as d decreases, the loading of dye and therefore α decreases. The optimal thickness is therefore representative of the point at which maximum dye-loading is observed without significantly increasing the thickness above the effective hole diffusion length – this limits recombination of charge carriers. Values of L can be obtained by conducting IPCE experiments with backside and frontside illumination and comparing the spectral response; this has proven effective in determination of photocurrent-limiting aspects of DSSCs.²⁶⁴

Although the steady state photocurrent limitations are explained by changes in thickness and loading, there are additional physical factors involved in increasing the thickness that impact performance. The thicker films display a lower transparency, therefore dye molecules loaded close to the back-contact will not undergo excitation when the electrode is illuminated from the front. Furthermore, the quality of 700 nm thick films was not ideal as observed in SEM images (**Figure 2.4**), therefore contributions to the lower photocurrent due to cracked films and disconnected islands cannot be ruled out with thicker films. The combination of these effects resulted in the best photocurrents for the film thickness of 500 nm with sol-gel synthesised CuCrO_2 . The 500 nm films were used for all further experiments in this study.

Linear sweep voltammetry (LSV) measurements showed that the photocurrent for NiO|DPP-P electrodes plateaued at voltages more negative than +0.4 V vs. RHE but with CuCrO₂|DPP-P electrodes continued growth of photocurrent was observed up to -0.2 V vs. RHE (**Figure 2.10**). The discrepancy may be related to different recombination kinetics in the two p-SCs. NiO exhibits a bias-dependent multiple-pathway recombination mechanism, where at more negative potentials, the contribution from trap states becomes more prominent.²⁵¹ Trap state contributions have been known to limit photocurrents in NiO-based systems,^{217,265} and methods to passivate them have proven successful.^{215,216} One possible phenomenon arising from a high density of traps at the surface is Fermi level pinning, where the Fermi level of the p-SC is pinned to these surface states.^{266–268} Decreasing the potential does not increase driving force for hole injection as it only results in charging of these states in the p-SC, placing an upper limit on achievable photocurrent. The continued rise in photocurrent with decreasing potential for the CuCrO₂ electrode suggests that this problem is not as apparent, and hints towards a lower density of surface states for this system. However, in-depth impedance and transient spectroscopic analysis is required to further support this theory.

The dark current exhibited by CuCrO₂ electrodes grows with decreasing applied potential. This is discussed in more detail in Section 2.5 with respect to the fully assembled photocathode.

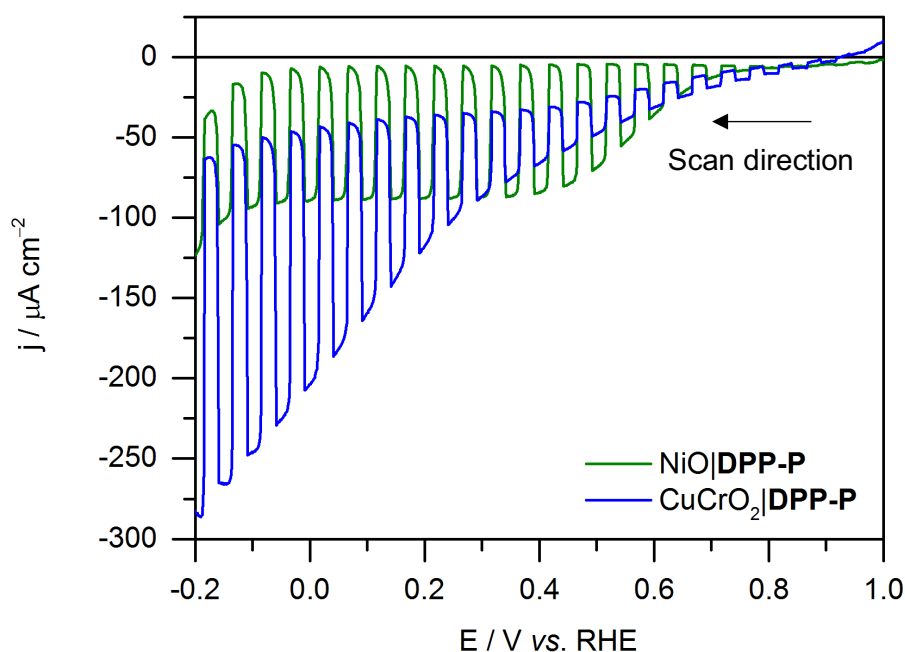


Figure 2.10 – LSVs of DPP-P-sensitised CuCrO₂ (500 nm, blue) and NiO (green) electrodes under chopped light illumination (100 mW cm^{-2} , AM 1.5G, $\lambda > 420 \text{ nm}$) in the presence of DTDP (5 mM in 0.1 M Na₂SO₄, pH 4.6). Electrode active area of 0.25 cm^2 was used in all cases and a scan rate of 5 mV s^{-1} .

2.5. Photoelectrochemistry with Co-Immobilised DPP-P and NiP

NiP was co-immobilised with **DPP-P** on CuCrO_2 using a 2:1 ratio of dye to catalyst in the same soaking bath (0.5 mM **NiP**, 1 mM **DPP-P**, DMF). This ratio was optimal for obtaining a higher proportion of dye than catalyst on the surface. Electrodes were soaked for 15 h and rinsed with DMF and water before use. Inductively coupled plasma-optical emission spectroscopy (ICP-OES) was used to determine the amount of **NiP** immobilised on the electrodes, and **DPP-P** loading was determined using UV-Vis spectroscopy following desorption in basic solution (see experimental section for more details). The amount of dye immobilised was higher than that of the catalyst (**NiP** = $0.75 \pm 0.40 \text{ nmol cm}^{-2}$, **DPP-P** = $2.55 \pm 0.66 \text{ nmol cm}^{-2}$).

LSVs and chronoamperometry results showed that CuCrO_2 |**DPP-P/NiP** electrodes gave around five times the photocurrent of the bare CuCrO_2 electrodes, achieving $-15 \mu\text{A cm}^{-2}$ at 0.0 V vs. RHE in aqueous Na_2SO_4 (0.1 M, pH 3) (**Figure 2.12**). A NiO photoelectrode featuring the same components gave photocurrents of $-5.8 \mu\text{A cm}^{-2}$ at 0.0 V vs. RHE, again demonstrating the higher ability of CuCrO_2 to function in a DSPC. The photocurrent onset potential for the CuCrO_2 photocathode is between +0.75 and +0.85 V vs. RHE owing to the positive VB (**Figure 2.11**).

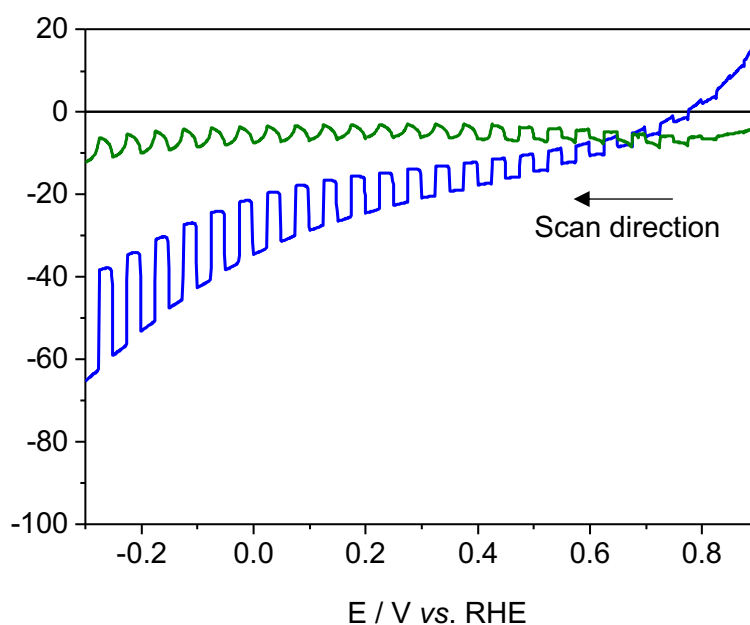


Figure 2.11 – LSVs under chopped light illumination (100 mW cm^{-2} , AM 1.5G, $\lambda > 420 \text{ nm}$) for CuCrO_2 |**DPP/NiP** (blue) and NiO |**DPP-P/NiP** (green) electrodes conducted in aqueous Na_2SO_4 (0.1 M, pH 3) using a 0.25 cm^2 active electrode area with a scan rate of 5 mV s^{-1} .

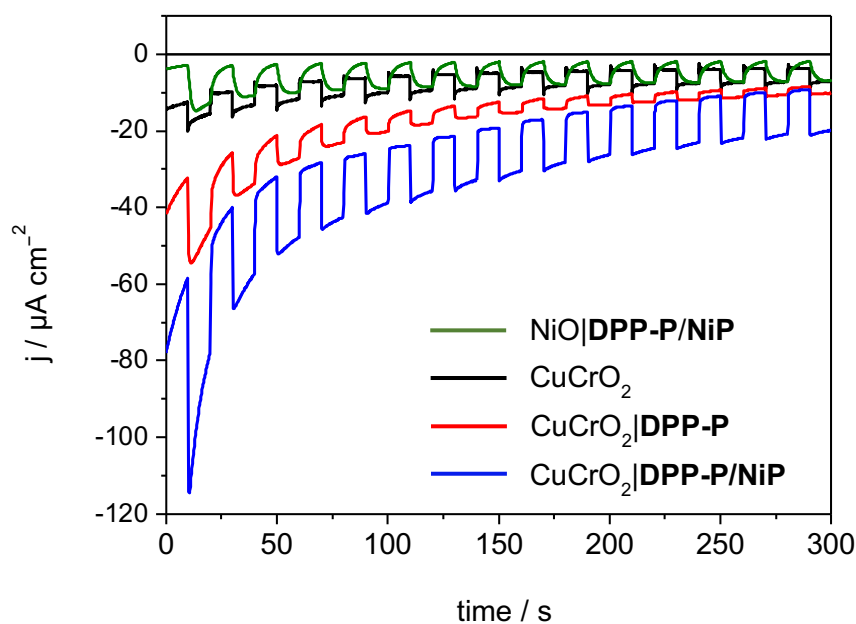


Figure 2.12 – Chronoamperometry measurements under chopped light illumination (100 mW cm^{-2} , AM 1.5G, $\lambda > 420 \text{ nm}$) for CuCrO_2 , $\text{CuCrO}_2|\text{DPP-P}$, $\text{CuCrO}_2|\text{DPP-NiP}$, and $\text{NiO}|\text{DPP-P/NiP}$ electrodes conducted in aqueous Na_2SO_4 (0.1 M, pH 3) at an applied potential of 0.0 V vs. RHE using a 0.25 cm^2 active electrode area.

A high dark current was observed for CuCrO_2 -based electrodes in the potential range used. The dark current is attributed to several factors that are dependent on both the material preparation method and the conditions used for PEC studies. Cyclic voltammograms showed a quasi-reversible redox feature at +0.5 V vs. RHE, which is assigned to a $\text{Cu}^{\text{II/I}}$ redox couple with associated oxygen intercalation,²⁶⁹ as well as persistent non-Faradaic current associated with film capacitance (**Figure 2.13**). Scanning to more negative potentials creates an oxidation peak at roughly +0.5 V vs. RHE, which disappears upon cycling at potentials more anodic than 0.0 V vs. RHE. Recent studies with CuGaO_2 have described similar results in agreement with this theory, suggesting that the redox couple arises from Cu^{2+} surface defects in contact with hydroxides.²⁷⁰ Although it is beyond the scope of this study, it is interesting to note that further understanding how these defects arise and determining ways to manipulate them could improve device performance. With NiO, understanding the nature of surface states and establishing procedures to passivate them has enhanced device performance and a similar protocol could be applied to delafossite materials.^{215–217}

Incident photon-to-current efficiency (IPCE) measurements confirmed the positive and vital role of the dye species, displaying a peak at the wavelength of maximum absorption for **DPP-P** ($\lambda_{\text{max}} = 496 \text{ nm}$), whereas the bare CuCrO_2 showed no peak in photocurrent at this wavelength (**Figure 2.14**).

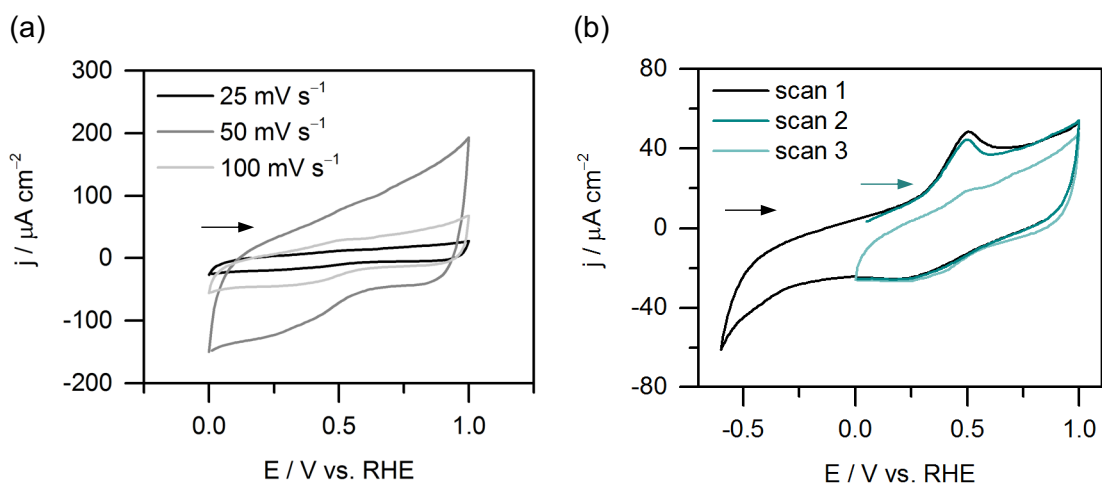


Figure 2.13 – Cyclic voltammograms of a CuCrO_2 electrode recorded in 0.1 M KCl (pH 7) with a) varying scan rate and b) scan rate = 25 mV s^{-1} : scan 1 = blank CuCrO_2 electrode, scan 2 = potential held at -0.5 V vs. RHE for 30 s prior to scan, scan 3 = directly following scan 2.

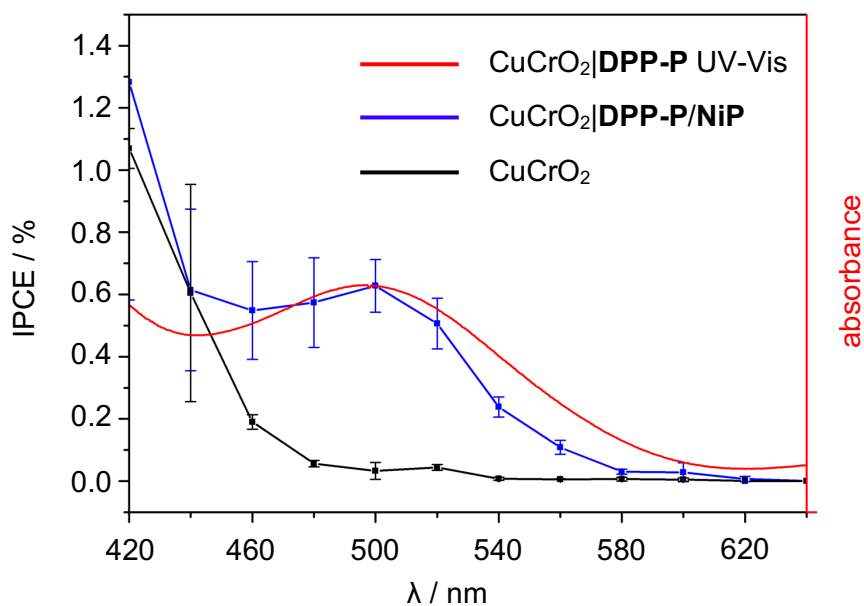


Figure 2.14 – Incident photon-to-current efficiency measurements for CuCrO_2 (black) and $\text{CuCrO}_2|\text{DPP-P}/\text{NiP}$ (blue) electrodes with a $\text{CuCrO}_2|\text{DPP-P UV-Vis}$ spectrum (red) measured in Na_2SO_4 (0.1 M, pH 3) with light intensity of 0.8 mW cm^{-2} and the applied potential maintained at 0.0 V vs. RHE .

Controlled potential photoelectrolysis (CPPE) under constant visible light illumination at an applied potential of 0.0 V vs. RHE was used to confirm H₂ generation (**Figure 2.15**). The photocurrent density for these 1 cm² electrodes was lower than expected from chronoamperometry experiments with 0.25 cm² electrodes, which is partly attributed to a higher sheet resistance in these larger films. However, the transient photocurrent upon light excitation, which decays over the course of minutes matches well with photocurrents recorded in the shorter timescale chronoamperograms. Photocurrent analysis at shorter timescales (ten of seconds) is consequently still representative of electrode performance and is valid for comparison. CuCrO₂|**DPP-P/NiP** photocathodes produced 94 ± 10 nmol cm⁻² H₂ as confirmed using gas chromatography (GC) analysis. The turnover number (TON) for **NiP** (126 ± 13) was determined using the loading quantity from ICP-OES measurements. A FE of (34 ± 8)% was obtained for the full photoelectrode, which although low, is common for such DSPCs. NiO|**DPP-P/NiP** electrodes generated 35 ± 2 nmol H₂ with a FE of (31 ± 8)%, confirming the superior performance of CuCrO₂-based photoelectrodes. It should be noted that although the loadings of dye and catalyst were not obtained for NiO electrodes, the structure was optimised for dye-sensitisation, and therefore the two electrodes are comparable in terms of overall performance. Importantly, no H₂ was detected for bare CuCrO₂, CuCrO₂|**DPP-P**, or CuCrO₂|**NiP** electrodes either under illumination or in the dark, highlighting the essential role of the dye/catalyst assembly.

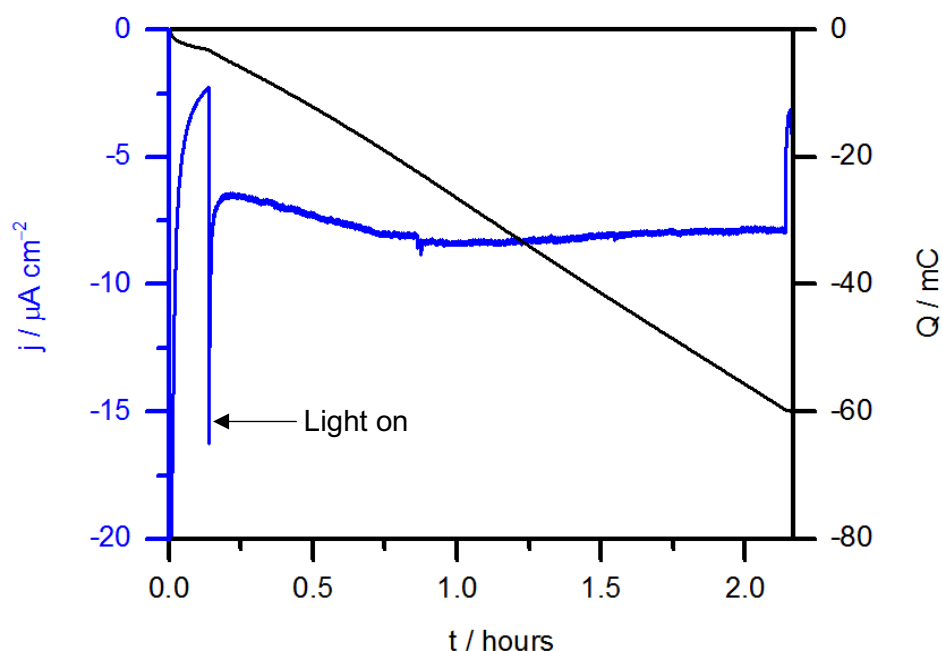


Figure 2.15 – Controlled potential photoelectrolysis of a CuCrO₂|**DPP-P/NiP** electrode over the course of 2 h under illumination (100 mW cm⁻², AM1.5G, λ > 420 nm) in aqueous Na₂SO₄ (0.1 M, pH 3) at an applied potential of 0.0 V vs. RHE using a 1 cm² active electrode area.

There are several explanations for the low FE. A dominant factor is the high dark current observed throughout electrolysis, the likely source of which is Cu^{2+} reduction to Cu^+ and oxygen deintercalation discussed above, as has previously been reported.^{269,271} Additionally, recent work has revealed problems with product detection for low photocurrent systems due to H_2 remaining in the solution phase – this is probable in the current system.¹⁹⁸ A method to improve the detection is the use of a Clark-type electrode for solution-based H_2 , however increasing the amount of H_2 generated is more ideal. Therefore, improvement of performance of such systems is key to understanding FE losses at this stage in DSPC development.

ICP-OES characterisation following CPPE showed that only $\approx 50\%$ of **NiP** was retained on the surface; this is in part due to the low loadings of dye and catalyst species, but also highlights some fundamental drawbacks associated with phosphonate anchoring groups in aqueous conditions.^{272,273} To prevent desorption, coating of surface-bound molecular species using atomic layer deposition,^{148,274–276} or through formation of polymeric catalyst assemblies have proven effective.^{277–280} Nanostructuring the surface would enhance loading and effectively trap surface bound species preventing dissociation; this would also prove beneficial in improving performance as enhanced loading of both catalyst and dye species should also improve photocurrents.

The work presented here shows some clear benefits of adopting CuCrO_2 as the p-SC in DSPCs. The TON of 126 ± 13 was the highest reported for such systems at the time of development, however this has been recently surpassed by a molecular Ru-Pt dyad, which generated a TON of 147 at an applied potential of -0.23 V vs. RHE.¹³¹ The previously highest reported TONs were ≈ 20 for a DSPC incorporating **NiP** in a supramolecular assembly with a Ru dye on ITO using a donor linker,¹²² and ≈ 16 for a similar assembly on NiO featuring doped bilayers,¹³⁷ however both systems were capable of generating higher amounts of H_2 , reflecting the higher loadings of catalyst and dye species on the surface. Co-immobilised molecular catalyst/dye combinations on NiO achieved a maximum TON ≤ 3 using a coumarin 343 dye with a bimetallic Fe catalyst.¹⁵¹ CuCrO_2 enabled high TONs with the co-immobilisation strategy, thereby enhancing the accessibility of DSPCs for solar H_2 generation. The amount of H_2 generated was noticeably higher in DSPCs assembled using CdSe quantum dots (QDs) with a cobaloxime catalyst;²¹¹ this is a promising route to explore for future DSPCs incorporating CuCrO_2 .

2.6. Conclusions

Immobilisation of an organic dye (**DPP-P**) and a molecular nickel catalyst (**NiP**) on the surface of CuCrO_2 resulted in a functional H_2 -generating photoelectrode. The photocathode gave a photocurrent of $-15 \mu\text{A cm}^{-2}$ at 0.0 V vs. RHE and produced $94 \pm 10 \text{ nmol H}_2$ over the course of 2 h CPPE under UV-filtered illumination in aqueous solution. The assembly reports a high TON of 126 ± 13 , demonstrating appreciable catalyst activity, and a comparative study with a benchmark NiO electrode demonstrated the superior performance of CuCrO_2 . The fully-assembled system does not contain any precious metals, demonstrating sustainable proton reduction. Co-immobilisation of the molecular components on the electrode proved sufficient for effective electron transfer between the dye and catalyst, taking advantage of an uncomplicated self-assembly strategy and avoiding the need for complex synthesis and challenging optimisation of dyad species.

The advances presented here demonstrate that replacing NiO with CuCrO_2 as the p-SC employed in DSPCs has a positive impact on PEC performance. Synthesis of CuCrO_2 using a solution processed technique and characterisation of the physical and electrochemical properties of the system as a whole, provides a framework for future optimisation and integration of various visible light absorbers and molecular catalysts.

2.7. Experimental Section

Materials and Methods

NiP⁹⁷ and **DPP-P**⁸⁰ were synthesised as previously reported. Milli-Q[®] H₂O (R > 18.2 MΩ cm) was used for all electrochemical and analytical measurements. Cu(acetate)₂·H₂O (ACROS Organics, ACS reagent), Cr(NO₃)₃·9H₂O (Sigma-Aldrich, ≥99%), and triethanolamine (Sigma-Aldrich, ≥99.5%) were used for CuCrO₂ film preparation. ITO-coated glass sheets (Vision Tek Systems Ltd., R = 12 Ω cm⁻², thickness of 1.1 mm) were cut into 3 × 3 cm² slides then scored into 1 × 1.5 cm² segments prior to cleaning. DTDP (Sigma-Aldrich, 98%) was used as an electron acceptor; the addition of this to pH 3 Na₂SO₄ solution at a concentration of 5 mM resulted in a pH shift from 3 to 4.6.

Physical Characterisation

SEM analysis was conducted using a FEI Phillips XL30 sFEG microscope. XRD measurements were taken with a PANalytical BV X'Pert Pro X-Ray Diffractometer. UV-Vis absorption spectra were acquired using a Varian Cary 50 spectrophotometer operated in transmission mode. N₂ gas adsorption measurements were carried out using a Micromeritics 3 Flex (Micromeritics, Norcross, GA, USA) with powder scraped from the surface of glass slides. Samples were degassed for 10 h at 100 °C, and measurements were carried out in liquid N₂. BET specific surface area values were obtained from fitting N₂ isotherms using the Microactive software.

Mott-Schottky Analysis

Electrochemical impedance measurements were carried out using an IviumStat potentiostat in a 3-necked round-bottomed flask at 25 °C in the dark. A three-electrode setup was used with a Ag/AgCl/KCl_{sat} reference, a Pt-mesh counter, and a CuCrO₂ working electrode (0.25 cm² active area). The electrolyte solution was Na₂SO₄ (0.1 M, pH 3) for all measurements. An excitation voltage of 10 mV was chosen with a frequency range of 10 kHz to 0.01 Hz. Nyquist plots were obtained for applied potential between 1.1 V to 0.3 V vs. RHE (15 mV step size) and fitted to a Randles circuit, featuring a constant phase element, in parallel with a charge transfer resistance element, in series with a solution resistance element, using ZView[®] software (Scribner Associates Inc.). The Mott-Schottky equation was used to estimate E_{fb} by plotting 1/C_{sc}² vs. E_{applied}, where the x-intercept is equal to E_{fb} + k_BT/e.

Preparation of CuCrO₂ Electrodes

ITO glass substrates were cleaned with successive sonication in isopropanol, ethanol, and acetone, for 15 min, then dried at 100 °C in air. A solution of Cu(acetate)₂·H₂O (0.2 M) and triethanolamine (0.2 M), in absolute ethanol was stirred for 1 h before the addition of Cr(NO₃)₃·9H₂O (0.2 M). The solution was stirred for 15 h before spin coating on to ITO slides (Laurell WS-650MZ spin coater, 1500 rpm, 15 s, 3000 rpm s⁻¹ acceleration, 0.4 mL volume). The samples were annealed in a chamber furnace (Carbolite Gero) to 400 °C with a ramp rate of 10 °C min⁻¹ for 45 min, then the spin-coating and annealing steps repeated for a total of 6 layers. The 6-layer samples were annealed in a tube furnace fitted with a quartz tube, end seals, and insulation plugs (Carbolite Gero) to 600 °C with a 5 °C min⁻¹ ramp rate for 45 min under N₂ flow (150 SCCM), forming CuCrO₂ electrodes.

Electrochemical Measurements of DPP-P

The reduction potential of **DPP-P**, $E_{(S/S^-)}$, was determined using CV. A 3-electrode setup was used with a glassy carbon working, a Ag wire reference, and a Pt-mesh counter electrode, with a scan rate of 50 mV s⁻¹. An electrolyte solution of tetrabutylammonium tetrafluoroborate (0.1 M) in dry DMF with **DPP-P** (\approx 1 mM) was used to determine the half-wave potential. The excited state reduction potential, $E_{(S^*/S^-)}$, was estimated by addition of E_{00} to $E_{(S/S^-)}$.

Dye and Catalyst Immobilisation

The dye and catalyst species were co-immobilised through soaking in a bath containing **DPP-P** (1 mM) and **NiP** (0.5 mM) for 15 h in DMF. A concentration of 1 mM was used for CuCrO₂|**NiP** and CuCrO₂|**DPP-P** electrodes. All electrodes were rinsed with DMF and water before being dried in air.

Quantification of Immobilised DPP-P and NiP

DPP-P was quantified using UV-Vis spectroscopy following desorption from CuCrO₂|**DPP-P**/**NiP** electrodes with tetrabutylammonium hydroxide 30-hydrate (0.1 M, DMF, 1 mL, 30 min). Higher concentrations and longer soaking times led to decomposition of the dye species and caused a shift in absorption. The absorption at 500 nm was determined for 4 electrodes and fitted to a calibration curve obtained using the desorption solution and soaking times to ensure degradation or effects of solvatochromism did not interfere with the determination of loadings. **NiP** loading was determined by ICP-OES following overnight

digestion of electrodes (1 cm^2) in aqueous HNO_3 (70%, 1 mL) and subsequent dilution to 10% v/v with MilliQ[®] H_2O . Values for nitric acid solution, CuCrO_2 , $\text{CuCrO}_2|\text{DPP-P}$, and pre- and post-electrolysis $\text{CuCrO}_2|\text{DPP-P/NiP}$ electrodes were determined in triplicate.

IPCE Measurements

A 3-electrode setup with a Pt-counter, $\text{Ag}/\text{AgCl}/\text{KCl}_{\text{sat}}$ reference, and a CuCrO_2 -based working electrode was used in a custom 3-necked cell with a flat borosilicate glass window for IPCE measurements. The electrolyte solution was Na_2SO_4 (0.1 M, pH 3) and an applied potential of 0.0 V vs. RHE was maintained for all measurements. Monochromatic light was supplied with a 300 W Xenon lamp solar light simulator connected to a monochromator (MSH300, LOT Quantum design). The intensity was calibrated to 0.8 mW cm^{-2} for each individual wavelength and experiments with CuCrO_2 and $\text{CuCrO}_2|\text{DPP-P/NiP}$ electrodes were conducted in triplicate with different electrodes with an active area of 0.25 cm^2 .

Photoelectrochemical Measurements

PEC measurements were conducted using an Ivium CompactStat potentiostat in a one-compartment 3-necked custom cell featuring a flat borosilicate window. A three-electrode setup was used with a Pt-counter, $\text{Ag}/\text{AgCl}/\text{KCl}_{\text{sat}}$ reference, and a CuCrO_2 -based working electrode (0.25 cm^2 active area). N_2 -purged (15 min) aqueous Na_2SO_4 electrolyte solution (0.1 M, pH 3) was used for all measurements. Electrodes were illuminated from the front using a calibrated Newport Oriel solar light simulator (150 W, 100 mW cm^{-2} , AM 1.5G) with an IR water filter and a UQG Optics UV-Filter ($\lambda > 420 \text{ nm}$).

CPPE experiments were conducted in triplicate at 0.0 V vs. RHE in a custom two-compartment electrochemical cell featuring a flat quartz window and a Nafion membrane divider. The working compartment volume was 12 mL with a gas headspace of 5 mL and the counter compartment contained 4.5 mL solution and a 3.5 mL headspace. Both compartments were purged with 2% CH_4 in N_2 for 30 min prior to electrolysis and the amount of H_2 determined using an Agilent 7890A series gas chromatograph with a 5 \AA molecular sieve column and a thermal conductivity detector. The flow rate was maintained at 3 mL min^{-1} and the oven temperature was set to $45 \text{ }^\circ\text{C}$. The partial pressure of H_2 was calculated to account for dissolved gas in the solution and this was added to the amount of H_2 detected to obtain the FE.

Chapter 3

Photoelectrochemical Hydrogen Generation with ZnSe Nanorods

*This chapter forms the basis of the following publication: ZnSe nanorods as a visible-light-absorber for photocatalytic and photoelectrochemical H₂ evolution in water, M. F. Kuehnel[†], C. E. Creissen[†], C. D. Sahn[†], D. Wielend, A. Schlosser, K. L. Orchard, E. Reisner, *Angew. Chem. Int. Ed.*, 2019, **58**, 5059 - 5063 ([†] denotes equal contribution). All experiments were conducted by the author with the exceptions stated here. Photoelectrochemical experiments were shared with Constantin Sahn. Photocatalytic experiments and ZnSe synthesis and characterisation were carried out by Dr. Moritz Kuehnel and Dominik Wielend.*

3.1. Introduction

Chapter 1 identified quantum dots (QDs) as ideal candidates for photocatalytic applications and Chapter 2 introduced CuCrO₂ as a suitable p-type semiconductor (p-SC) for DSPCs. This chapter aims to highlight the applicability of ZnSe QDs in photoelectrochemical (PEC) H₂ generation using CuCrO₂ as the p-type semiconductor (p-SC).

The photoreduction of aqueous protons to H₂ can be enabled using a wide range of photocatalysts.²⁰ In particular, semiconductor nanocrystals have emerged as highly active and simply synthesised candidates, often consisting of non-precious metal elements.^{87,175,176} Easy capping ligand modification on the surface of these nanocrystals and tuneable optical properties through size variation makes them highly adaptable for photocatalysis.^{169,172,175,177} Chalcogenide nanocrystals in particular have shown good promise for proton reduction in water – among these, Cd-based QDs are the most commonly employed.^{57,92,178–180} High activity and stability of such QDs in aqueous conditions has enabled reports of high quantum yields for H₂ production, however the toxic nature and carcinogenic properties of cadmium currently constrains extensive applicability.²⁸¹ Efforts to translate the high performance exhibited by Cd-QDs to carbon-based materials has produced some promising results in colloidal H₂-generating systems – carbon nitride,^{22,78,183} carbon dots,^{40,184–186,282} and organic polymers,^{181,182,283,284} being dominant examples – however their performance remains comparatively low. In the search for Cd-free chalcogenide QDs, ZnSe has surfaced as a suitable alternative.¹⁷⁴

ZnSe is an n-type semiconductor with a direct bandgap of 2.7 eV exhibiting high electron mobility ($610 \text{ cm}^2 \text{ V}^{-1} \text{ s}^{-1}$) and a highly negative conduction band ($E_{\text{CB}} = -1.1 \text{ V vs. RHE}$), making it a suitable candidate for solar driven catalysis.^{285–287} ZnSe has previously been employed for CO_2 reduction to CO with a Ni-cyclam catalyst but the aim of the hybrid colloidal system was to limit proton reduction through functionalisation of the surface with a mercaptopropionic acid capping ligand.¹⁷⁴ Until recently, photocatalytic H_2 generation with ZnSe was previously restricted to examples displaying poor performance or requiring Cd components to function effectively.^{187–189} However, ZnSe nanorods (NRs) were recently developed in our group to enhance H_2 generation in a photocatalytic system using a sacrificial electron donor (SED). Here, optimised ZnSe-NRs were integrated with p-type CuCrO_2 , forming a QD-sensitised photocathode thus removing the need for the SED. Construction of such a system aims to combine the beneficial photochemistry of nanoparticulate light absorbers with a p-SC to facilitate photocathodic charge transport (**Figure 3.1**). This presents a novel functional photocathode that operates in aqueous solution without the requirement of a co-catalyst or a SED.

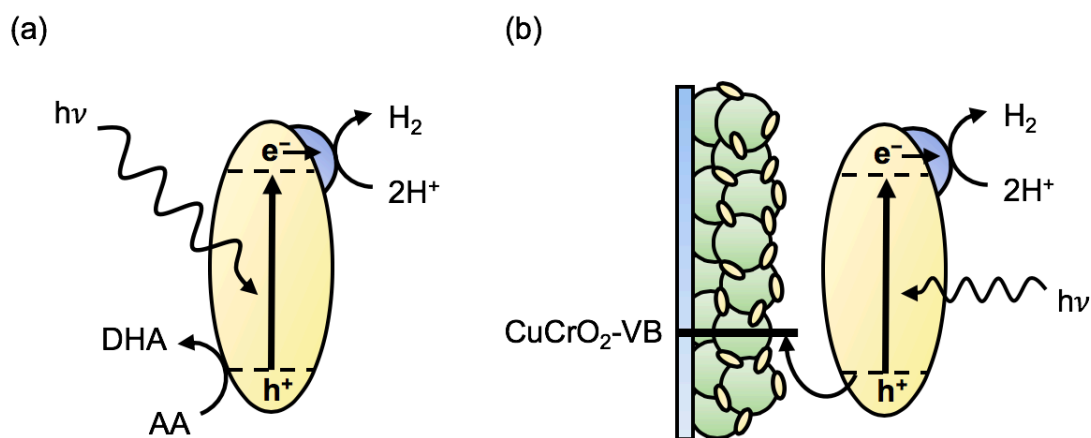


Figure 3.1 – Illustration of a) photocatalytic proton reduction with a sacrificial electron donor, and b) photoelectrochemical hydrogen generation with ZnSe-sensitised CuCrO_2 . e^- = electrons, h^+ = holes, AA = ascorbic acid, and DHA = dehydroascorbic acid. Blue circles represent the catalytic site.

3.2. ZnSe Nanorods

3.2.1. Synthesis and Characterisation

ZnSe-NRs were prepared through a 'ligand stripping' procedure previously shown to enhance catalytic activity with CdS.¹⁷³ Stearate-capped ZnSe-NRs (ZnSe-St) were initially prepared through a hot injection method as previously reported.²⁸⁸ Reactive ligand removal with $[\text{Me}_3\text{O}][\text{BF}_4]$ gave ZnSe-BF₄, so called 'ligand-stripped' NRs (see experimental section for full details). TEM analysis showed that NRs with diameter 5.2 ± 0.6 nm and length 30 ± 4.8 nm (aspect ratio 5.8 ± 0.9) were obtained and XRD analysis confirmed a mixture of wurtzite and zincblende polymorphs, as observed previously with a similar synthetic procedure. UV-Vis spectroscopy showed absorption in the visible region at wavelengths less than 450 nm (Figure 3.2).²⁸⁹

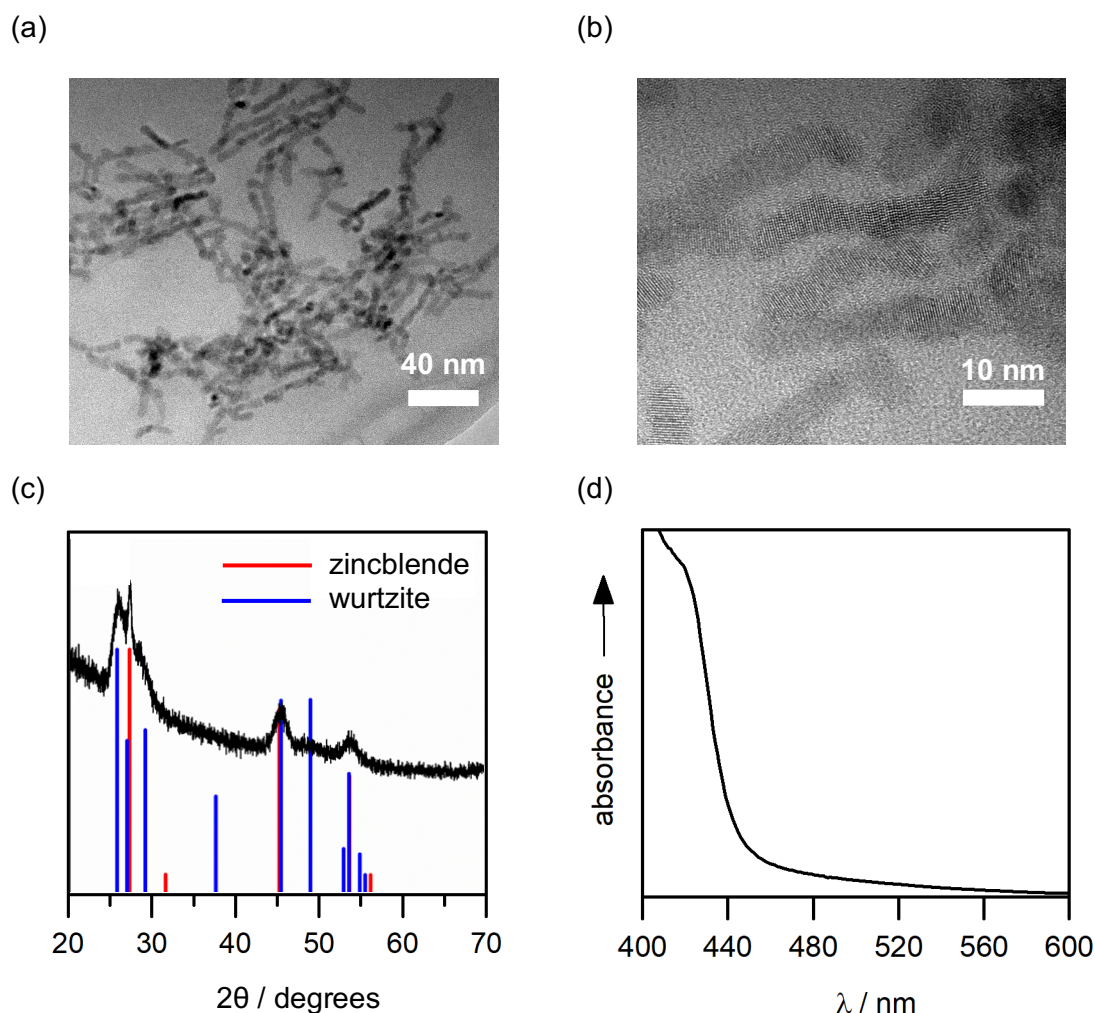


Figure 3.2 – a) and b) TEM images of the ZnSe-BF₄ nanorods, c) a powder XRD pattern for ZnSe-BF₄ with reference patterns for zincblende (PDF 01-0715977 37-1463) and wurtzite (PDF 01-089-2940 15-105) ZnSe crystal structures, d) UV-Vis spectrum of ZnSe-BF₄ in DMF.

3.2.2. Photocatalytic Properties

Suspension systems using sacrificial reagents are valuable in assessing the photocatalytic ability of colloidal nanocrystals to facilitate redox reactions under illumination. ZnSe-NRs exhibit a high ability to evolve H₂ in such systems when using ascorbic acid (AA) as the SED. Photogenerated holes are transferred to AA, which is readily oxidised to dehydroascorbic acid (DHA) in two separate electron transfer steps involving the radical anion semidehydroascorbate (**Appendix, Figure A1**), and photoexcited electrons generate H₂ at a catalytic site. The activity of ZnSe-BF₄ was significantly higher than the corresponding ZnSe-St and mercaptopropionic acid-capped ZnSe (ZnSe-MPA) NRs, using simulated solar light illumination ($\lambda > 400\text{nm}$, 100 mW cm^{-2} , AM 1.5G) under optimised conditions (pH 4.5, 0.4 M AA, 50 mg L^{-1} ZnSe) (**Appendix, Figure A2**). Addition of Ni(BF₄)₂ with 20 μM concentration increased the activity in all cases, suggesting *in situ* formation of a heterogeneous Ni catalyst, capable of enhancing proton reduction.⁸⁴ Additionally, long term experiments showed that ZnSe-BF₄ QDs were stable for up to 40 hours, the reduction in rate at longer times being attributed to depletion of AA and build-up of DHA, which is a known inhibitor for H₂ generation (**Figure 3.3**).^{40,41}

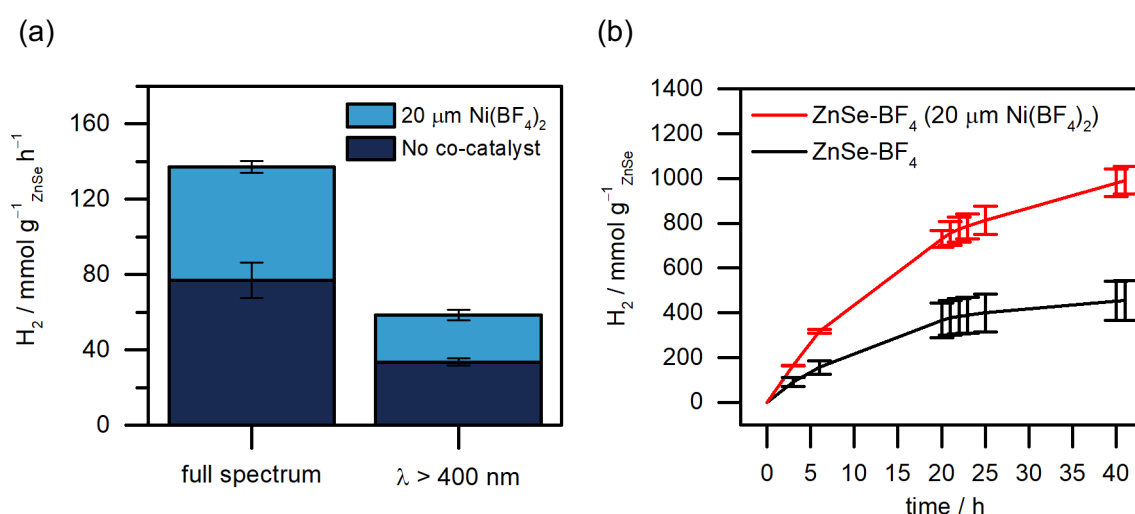


Figure 3.3 – a) The rate of H₂ generation after 3 h irradiation in the presence and absence of 20 μM Ni(BF₄)₂ under full spectrum and UV-filtered light ($\lambda > 400\text{ nm}$), b) long-term photocatalysis with ZnSe-BF₄-NRs ($\lambda > 400\text{ nm}$). Conditions: 50 mg L^{-1} ZnSe, 0.4 M AA, pH 4.5, 25 °C, 100 mW cm^{-2} , AM 1.5G.

In comparison to previous reports with ZnSe-based photocatalysts, these NRs showed a higher activity.^{187,188} The ZnSe-BF₄ NRs reported here are much closer in activity to Cd-based QDs without the addition of a co-catalyst.^{290,291} The high performance reflects the clear catalytic ability of ZnSe to reduce aqueous protons to H₂ and demonstrates that ligand

stripping enhances photocatalytic activity, which is likely due to an increased number of exposed active surface sites, as observed in other similar systems.^{173,292–294} Catalyst-free H₂ generation with ZnSe QDs enhances the viability of solution-based photocatalytic systems, however the need for a SED limits expansion. Although certain examples of photocatalysis using waste products as the electron donor exist,^{24,26} kinetic limitations on the oxidative side restrict material choice, blocking the scope for current expansion.²⁹⁵ The additional problem of DHA accumulation and AA depletion can be avoided by replacement with a p-SC to accept photogenerated holes from ZnSe. CuCrO₂ represents suitable p-SC to replace the SED.

3.3. Assembly and Characterisation of CuCrO₂|ZnSe Photoelectrodes

Several deposition techniques for different QDs have been proposed including *in situ* and *ex situ* methods.²⁹⁶ Photocatalytic experiments showed that ligand-stripped ZnSe-NRs displayed high activity, therefore alterations to synthetic procedure would likely affect the performance. Consequently, an *ex situ* deposition method was required. Several techniques were investigated including drop casting; cross-linking dots on the surface with ethanedithiol; and ligand modification of the CuCrO₂ surface with thiols featuring different metal oxide anchoring groups followed by NR deposition. PEC screening to identify the most promising deposition method was conducted in aqueous Na₂SO₄ (0.1 M, pH 5.5) under illumination (100 mW cm⁻², AM 1.5G, λ > 400 nm) at 0.0 V vs. RHE. Results showed that of the tested methods, the most promising was direct drop casting on the CuCrO₂ electrode (**Figure 3.4**).

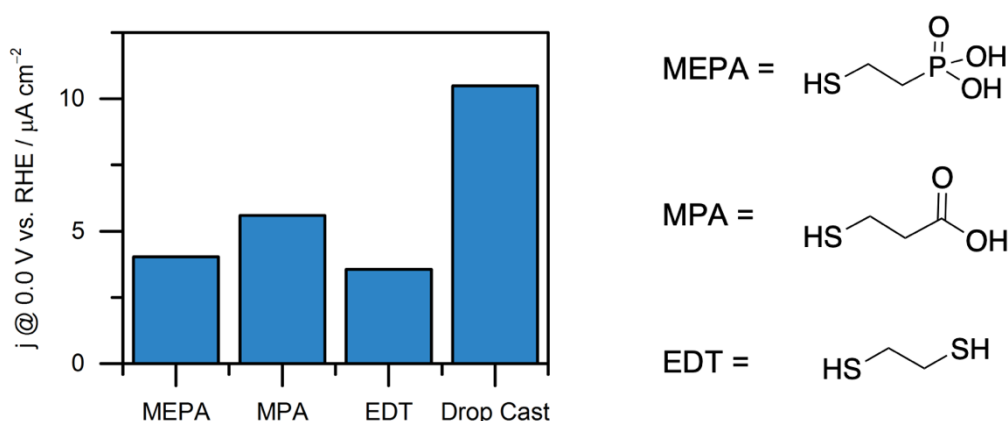


Figure 3.4 – Photocurrent comparison of different strategies to form ZnSe layers on CuCrO₂ with ligand structures highlighted. Electrodes soaked 15 h in ligand solution (1 mM, DMF) then in ZnSe-NRs (1.66 mg mL⁻¹, DMF, 2 h), or ZnSe-NRs were drop cast directly on CuCrO₂ (8 μL cm⁻², 1.66 mg mL⁻¹). Conditions: aqueous Na₂SO₄ (0.1 M, pH 5.5), 0.0 V vs. RHE, 100 mW cm⁻², AM 1.5G, λ > 400 nm.

The drop casting method limited exposure of ZnSe-QDs to oxygen and was capable of forming homogeneous layers without long soaking periods or alteration of the capping ligand. It should be noted that a recent report using CdSe-sensitised NiO with a thiol-based linker highlighted that the capping ligand can in fact act as a hole trap which limits activity.²¹² Therefore, for linker-assisted metal oxide modification with QDs, an exploration of alternative anchoring groups is required. The results also support the observed improvement in photocatalytic activity of ligand-stripped NRs, validating the theory that exposed surface sites enhances catalysis.

CuCrO₂|ZnSe electrodes were prepared through drop casting a ZnSe-BF₄ solution (8 μL cm⁻², 1.66 mg mL⁻¹, acetonitrile) on freshly prepared CuCrO₂ electrodes. Acetonitrile was used to enable fast-drying, avoiding oxidation and aggregation of NRs, which was observed with DMF. CuCrO₂ electrodes were synthesised as previously reported (Chapter 2),²⁹⁷ but with only 3 layers as opposed to 6 to give a thickness of 300 nm. The thinner layer was ideal as it limited unwanted absorption from the CuCrO₂ film close to the region in which ZnSe absorbs most light. Furthermore, charge transport through the p-SC film is less restricted due to the shorter distance holes must travel in thinner samples – this ensures that the effective diffusion length of holes is much greater than the film thickness (see Chapter 2, Section 2.4).

Deposition led to a ZnSe layer on the surface around 80 – 100 nm thick as shown using SEM analysis (**Figure 3.5**). Energy-dispersive X-Ray spectroscopy (EDS) confirmed the composition of CuCrO₂ films for bare and ZnSe-immobilised areas, showing a homogeneous distribution across the film (**Figure 3.6**), however mapping across the cross-section was not possible due to the large interaction volume associated with the high energy of the incident beam. The absorption properties were verified using UV-vis spectroscopy, where enhanced absorbance between 410 – 440 nm was observed for CuCrO₂|ZnSe electrodes over the blank CuCrO₂, matching well with the ITO|ZnSe spectrum (**Figure 3.7**). The amount of ZnSe immobilised on the surface was determined to be 13.4 ± 0.53 μg cm⁻² from ICP-OES measurements.

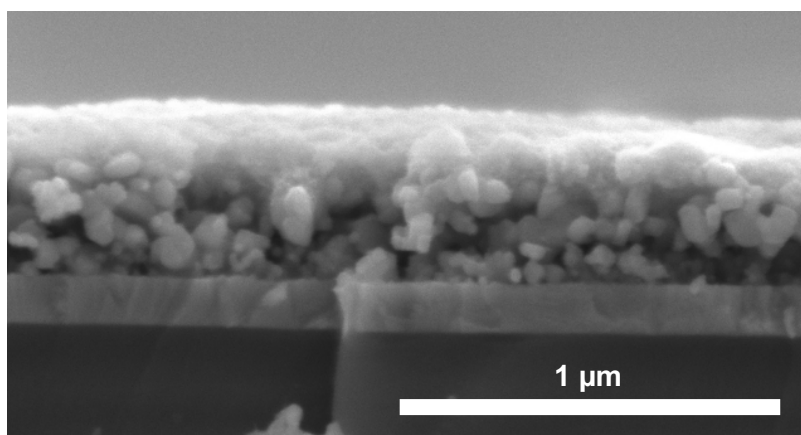


Figure 3.5 – Cross-sectional SEM image of a CuCrO₂|ZnSe electrode.

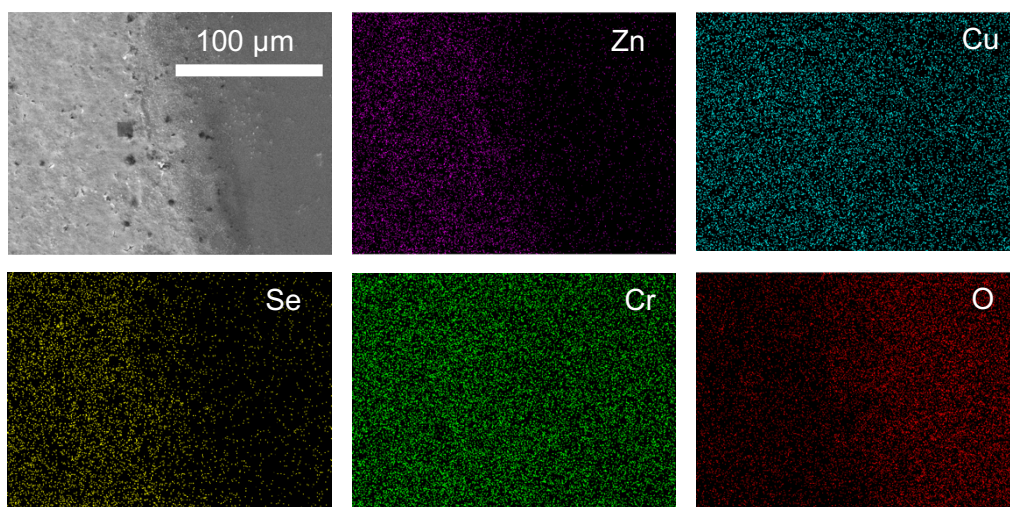


Figure 3.6 – EDS elemental map of the CuCrO₂/CuCrO₂|ZnSe edge.

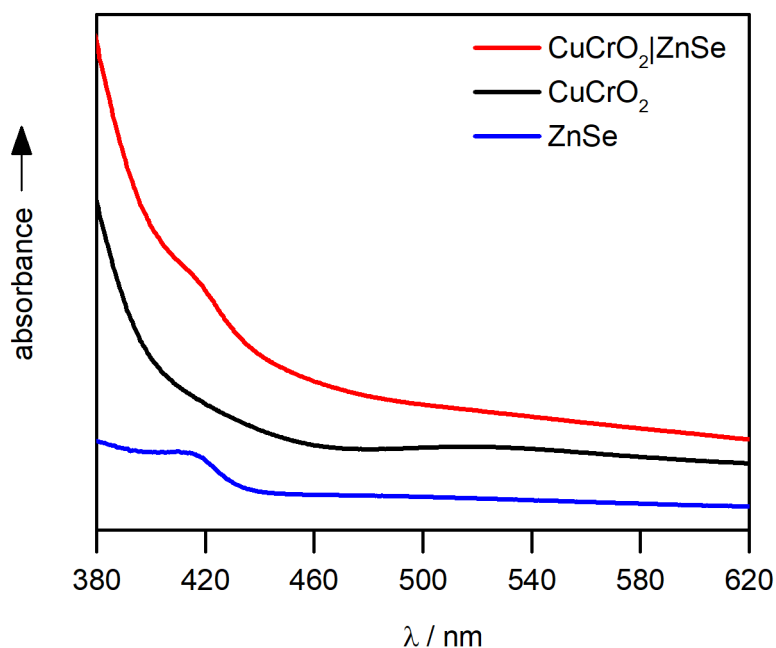


Figure 3.7 – Transmission mode UV-Vis spectra of ZnSe, CuCrO₂, and CuCrO₂|ZnSe electrodes with the ITO-glass background subtracted.

3.4. H₂ Generation with CuCrO₂|ZnSe Electrodes

PEC measurements were conducted to assess the ability of ZnSe to inject holes into the valence band of CuCrO₂. Owing to the high thermodynamic driving force and catalytic proficiency of ZnSe-NRs, a sacrificial electron acceptor was not required, and instead pure aqueous conditions were used. Linear sweep voltammograms (LSVs) in Na₂SO₄ (0.1 M, pH 5.5, $\lambda > 400$ nm, 100 mW cm⁻², AM 1.5G) displayed an increasing photocathodic current at potentials more negative than +0.75 V vs. RHE (**Figure 3.8**). ITO|ZnSe electrodes showed a low photoanodic response throughout the entire scan region (**Appendix, Figure A3**). Chronoamperograms of CuCrO₂ and CuCrO₂|ZnSe electrodes held at 0.0 V vs. RHE gave photocurrents of -3 and -10 $\mu\text{A cm}^{-2}$ respectively showing a clear enhancement upon immobilisation of ZnSe, which is representative of the capability of the ZnSe-based photoelectrode to reduce aqueous protons to H₂ (**Figure 3.9**).

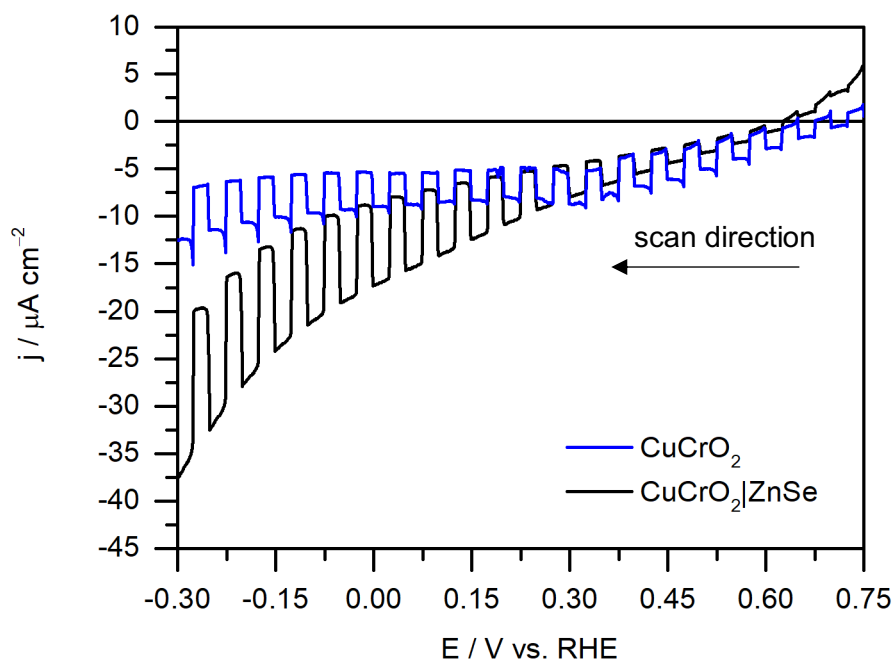


Figure 3.8 – LSVs under chopped light illumination (100 mW cm^{-2} , AM 1.5G, $\lambda > 400 \text{ nm}$) for CuCrO_2 and $\text{CuCrO}_2|\text{ZnSe}$ electrodes conducted in aqueous Na_2SO_4 (0.1 M, pH 5.5) using a 0.25 cm^2 active electrode area with a scan rate of 5 mV s^{-1} .

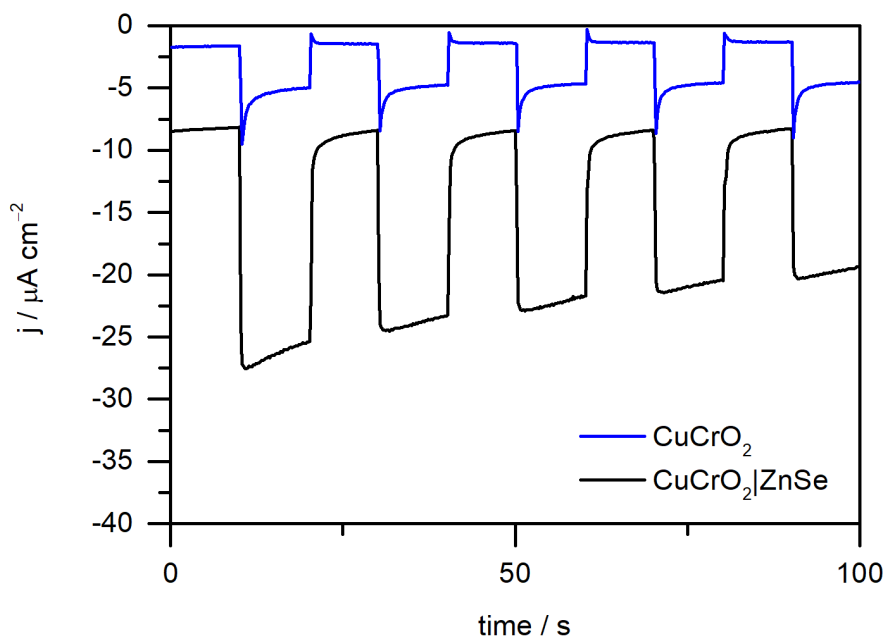


Figure 3.9 – Chronoamperograms under chopped light illumination (100 mW cm^{-2} , AM 1.5G, $\lambda > 400 \text{ nm}$) for CuCrO_2 and $\text{CuCrO}_2|\text{ZnSe}$ electrodes conducted in aqueous Na_2SO_4 (0.1 M, pH 5.5) using a 0.25 cm^2 active electrode area at an applied potential of 0.0 V vs. RHE .

Interestingly, the dark current increased upon immobilisation of ZnSe suggesting that the connection between the NRs and the CuCrO₂ surface is not ideal. The increase could be due to increased capacitance as the NRs could plausibly store charge in mid-gap or surface trap states.^{298,299} Trapping was observed for ZnSe-QDs with an immobilised Ni-cyclam but fast charge transfer to the catalyst meant that in fact these traps facilitated CO₂ reduction.¹⁷⁴ Reductive degradation of ZnSe-NRs is also possible, however this is less likely considering the high stability in solution-based photocatalysis. The anisotropic shape of the ZnSe-NRs was retained following photocatalysis, therefore any distinct morphological changes were ruled out. The disappearance of transient photocurrent spikes upon immobilisation of ZnSe-NRs is indicative of more efficient charge transport. Similar spikes have been reported in several systems, which are typically assigned to accumulation of charge at the p-SC/solution interface, therefore indirectly representing recombination and catalysis rates.^{49,98,135,148} The loss of spikes infers that either proton reduction is kinetically less limited in the CuCrO₂|ZnSe system than with the bare CuCrO₂ electrode, as accumulated charge carriers are dissipated faster, or that recombination between photogenerated electrons and the p-SC is not significant.

Incident photon to current efficiency (IPCE) plots of the bare and ZnSe-sensitised CuCrO₂ electrodes confirmed that the dominant contribution to photocurrent originated from the region between 400 – 420 nm, corresponding well with the absorption spectrum of ZnSe-BF₄ NRs in solution (**Figure 3.10**). The major portion of photocurrent is therefore representative of the photoinduced catalysis from ZnSe-NRs. Bare CuCrO₂ electrodes showed some contribution to the IPCE values at wavelengths below 420 nm, which could be associated with a small degree of light-excitation and slow catalysis as reflected by the transient spikes, or photodegradation as has been observed with narrow-bandgap delafossite materials.^{219,222,300} To rule out significant contribution to H₂ generation from CuCrO₂, controlled potential photoelectrolysis (CPPE) is required.

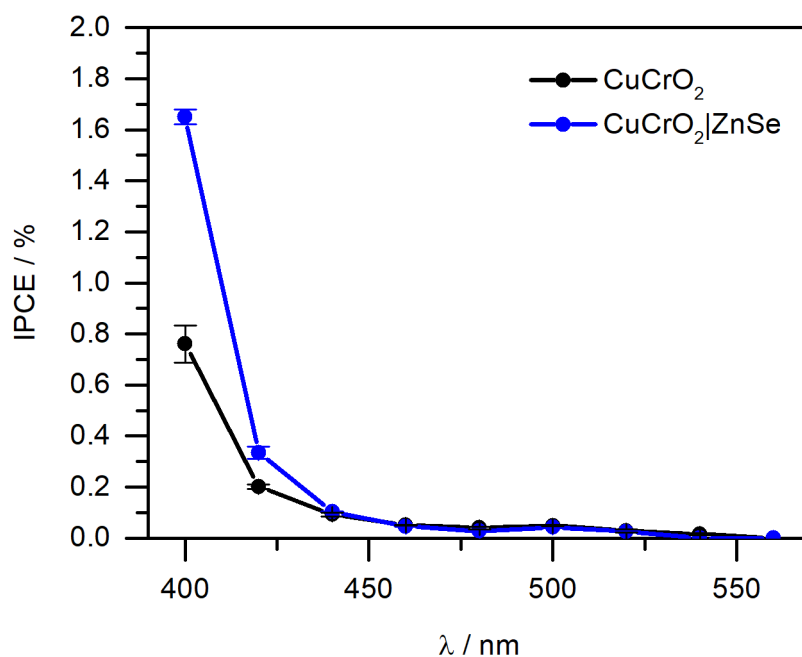


Figure 3.10 – IPCE measurements for CuCrO₂ (black) and CuCrO₂|ZnSe (blue) electrodes measured in Na₂SO₄ (0.1 M, pH 5.5) with light intensity of 1 mW cm⁻² and the applied potential maintained at 0.0 V vs. RHE.

To confirm the catalytic activity of CuCrO₂|ZnSe electrodes, CPPE was conducted in aqueous Na₂SO₄ (pH 5.5, 0.1 M, N₂ purged). CuCrO₂|ZnSe photoelectrodes generated 33.5 ± 3.1 nmol H₂ in 4 h under constant illumination (λ > 400 nm, 100 mW cm⁻², AM 1.5G) with a Faradaic efficiency (FE) of (7.3 ± 1.9)% (**Figure 3.11**). CuCrO₂ electrodes without ZnSe produced no detectable H₂ under the same conditions, supporting the assumption that photocurrents produced were not related to catalysis, or that H₂ generation without the NRs is negligible (**Appendix, Figure A4**). As expected, addition of Ni(BF₄)₂ to the solution (20 μM) showed a slight enhancement, producing 47.8 nmol H₂ over the course of 4 h with a FE of 9.7%. This represents a 40% enhancement over the catalyst-free ZnSe, and as in the photocatalytic system, is likely due to the *in situ* formation of a heterogeneous Ni catalyst.⁸⁴

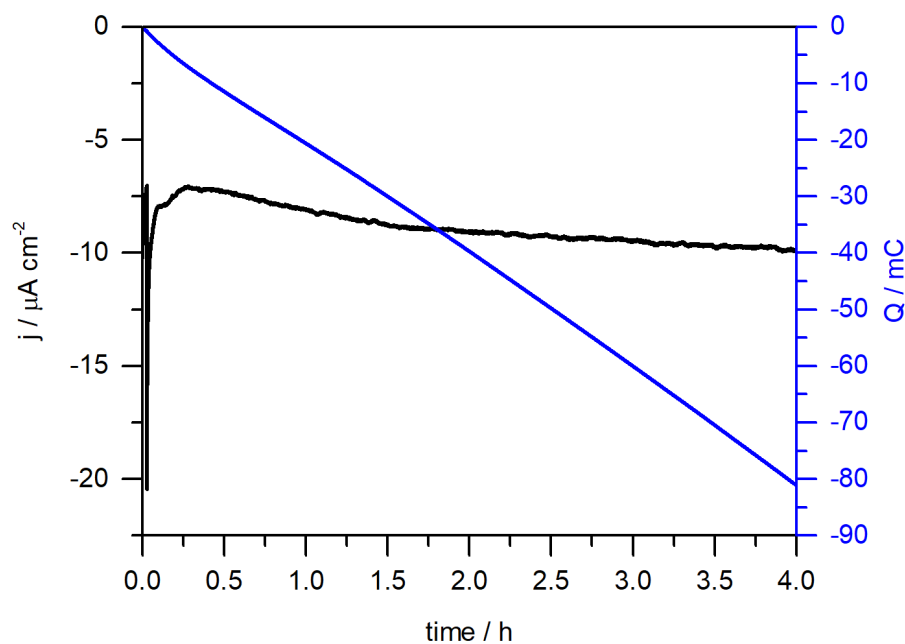


Figure 3.11 – Controlled potential photoelectrolysis of a $\text{CuCrO}_2|\text{ZnSe}$ electrode over the course of 4 h under illumination (100 mW cm^{-2} , AM 1.5G, $\lambda > 400 \text{ nm}$) in aqueous Na_2SO_4 (0.1 M, pH 5.5) at an applied potential of 0.0 V vs. RHE using a 1 cm^2 active electrode area.

The low FE is attributed in part to the high dark current stemming from CuCrO_2 electrodes synthesised using this method (Chapter 2, Section 1.2.6).²⁹⁷ However, for low photocurrent-generating systems the high amount of H_2 that remains in solution is also a contributing factor.¹⁹⁸ Although the PEC cells were left to equilibrate for 2 h following electrolysis prior to GC analysis, there was only a slight change in H_2 detected, suggesting that in fact non-Faradaic processes are substantial in the photocathodes.

The work presented here is the first demonstration of H_2 generation with a ZnSe-sensitised photocathode. $\text{CuCrO}_2|\text{ZnSe}$ photocathodes achieved $-10 \text{ } \mu\text{A cm}^{-2}$ at 0.0 V vs. RHE applied potential without the addition of a co-catalyst. Previous catalyst-free QD-sensitised photocathodes have reported higher photocurrents of $-60 \text{ } \mu\text{A cm}^{-2}$ at 0.3 V vs. RHE with MPA-modified CdSe,²¹³ and $-180 \text{ } \mu\text{A cm}^{-2}$ at 0.5 V vs. RHE using a phenothiazine hole-accepting ligand with CdSe,²¹⁴ both using NiO as the p-SC. However, this is also associated with the better-suited absorption profile of CdSe, which lies further into the visible region. Although the activity of these Cd-based photocathodes is higher than that exhibited by the $\text{CuCrO}_2|\text{ZnSe}$ photocathode, the removal of carcinogenic components provides a framework for future development. There are some clear routes to improvement of Cd-free photocatalytic and DSPEC systems. Some examples that have proven beneficial in Cd-based systems are outlined below.

Addition of a heterogenous co-catalyst ($\text{Ni}(\text{BF}_4)_2$) in this system enhanced the amount of H_2 generated demonstrating that ZnSe is not an ideal catalyst on its own. Alteration of the catalyst used to better suit the photoelectrode could yield higher photocurrents. A bimetallic Fe complex ($\text{Fe}_2\text{S}_2(\text{CO}_6)$) was integrated with CdSe QDs on a NiO electrode and showed a clear photocurrent enhancement with associated H_2 generation,²¹⁰ and a phosphonic acid-bearing cobaloxime was co-immobilised with CdSe on NiO generating photocurrents up to $-100 \mu\text{A cm}^{-2}$ at $+0.4 \text{ V vs. RHE}$.^{211,212} ZnSe can be used to drive more thermodynamically challenging reactions such as CO_2 reduction as has been demonstrated in colloidal suspension systems with an immobilised Ni(cyclam).¹⁷⁴ Having established the capability of ZnSe to function as a photosensitiser, the scope for integration of different catalysts and further development of the interface has been expanded.

Assembly methods using beneficial characteristics of capping ligands to control charge transfer also shows some promise.¹⁷² Studies have shown that deposition of QDs can passivate surface states in some cases, thereby limiting recombination.²⁵² In the system presented here, it is likely that a limitation arises from surface traps in both the p-SC and the NRs themselves. Previous work has shown that in some cases traps can assist catalytic activity,¹⁷⁴ however that is unlikely to be the case with the catalyst-free ZnSe-NRs used here. Passivating traps could prove effective in limiting recombination of charge carriers and has been effective in the development of colloidal QD-based solar cells.^{299,301}

Hydrophilic and conjugated ligands for effective hole transfer have been explored with CdSe,³⁰² and recent work has highlighted how surface-bound anthracenes can facilitate efficient hole injection into NiO.³⁰³ Hole trapping with thiol-based ligands has been shown to limit effective charge transport observed in NiO-based systems,²¹² therefore exploration of alternative capping ligands could enhance activity. The higher activity observed here with ligand-stripped dots over MPA- or St-capped ZnSe further confirms the impact of surface structure and capping ligand on catalysis. A recent investigation of the impact of S^{2-} in CdSe QDs showed that internal sulfide acts to assist electron transfer to a co-catalyst, whereas the surface sulfide, which forms as a capping ligand, facilitates hole injection to the SED.²⁹⁴ These studies can be used as basic guidelines for future integration of ZnSe with p-SCs, however the interface in each case must be evaluated using spectroscopic and electrochemical techniques. Improving the interface between the CuCrO_2 and ZnSe-NRs would limit recombination and enhance photocurrents. Nanostructuring the CuCrO_2 surface is one route improve the interaction to enable a higher rate of H_2 generation in similar DSPCs.

3.5. Conclusions

The results presented here demonstrate that ZnSe-NRs are a competitive alternative to conventional Cd-based QDs for photoelectrochemical H₂ generation in water. Ligand-stripped ZnSe-NRs were immobilised on CuCrO₂ to form a photocathode, effectively replacing the SED component. CuCrO₂|ZnSe photoelectrodes achieved photocurrents of $-10 \mu\text{A cm}^{-2}$ at 0.0 V vs. RHE and produced $33.5 \pm 3.1 \text{ nmol H}_2$ in 4 h under illumination ($\lambda > 400 \text{ nm}$) with a FE of $(7.3 \pm 1.9)\%$. This study establishes ZnSe QDs as highly efficient photosensitiser and highlights the versatility of CuCrO₂ electrodes as a wide-bandgap p-SC for QD-sensitised H₂ generation. The results pave the way for future integration of QDs as stable, non-carcinogenic light absorbers that do not require an immobilised co-catalyst to operate effectively.

3.6. Experimental Section

Materials

Zinc stearate (purum, Sigma-Aldrich), octadecane (99%, Sigma-Aldrich), trioctylphosphine (90%, Sigma-Aldrich), selenium powder (99%, Sigma-Aldrich), *n*-heptane (99%, Sigma-Aldrich), methanol (99.8%, Fisher-scientific), acetone (laboratory reagent grade, Fisher-scientific), 1-butanol (99%, Alfa Aesar), trimethyloxonium tetrafluoroborate (96%, Sigma-Aldrich), tetramethyl ammonium hydroxide pentahydrate (99%, Sigma-Aldrich), 3-mercaptopropionic acid (MPA, $\geq 99\%$, Sigma-Aldrich), and $\text{Ni}(\text{BF}_4)_2 \cdot 6\text{H}_2\text{O}$ (99%, Acros) were used as received. Diethyl 2-bromoethylphosphonate (97%, Sigma-Aldrich), potassium thioacetate (98%, Sigma-Aldrich), and bromotrimethylsilane (97%, Sigma-Aldrich) were used for the synthesis of MEPA. Anhydrous solvents were purchased from Acros Organics with the following purities: CHCl_3 (99.9%), *N,N*-dimethylformamide (DMF, 99.8%), acetonitrile (ACN, 99.9%). $\text{Cu}(\text{acetate})_2 \cdot \text{H}_2\text{O}$ (ACROS Organics, ACS reagent), $\text{Cr}(\text{NO}_3)_3 \cdot 9\text{H}_2\text{O}$ (Sigma-Aldrich, $\geq 99\%$), and triethanolamine (TEOA, Sigma-Aldrich, $\geq 99.5\%$) were used for CuCrO_2 film preparation. ITO-coated glass sheets (Vision Tek Systems Ltd., $R = 12 \Omega \text{ cm}^{-2}$, thickness of 1.1 mm) were cut into $3 \times 3 \text{ cm}^2$ slides then scored into $1 \times 1.5 \text{ cm}^2$ segments before use. All aqueous experimental solutions were prepared with distilled water and all aqueous analytical samples were prepared with ultrapure water (Milli-Q[®], 18.2 M Ω cm).

ZnSe-St Nanorod Synthesis

Zinc stearate (1 mmol) was stirred in octadecane (8 g) under N_2 at 50 °C for 2 h before raising the temperature to 300 °C. Selenium powder (1 mmol) in trioctylphosphine (2.5 mL) was heated to 100 °C then quickly injected into the zinc precursor solution. The reaction mixture was stirred for 25 min then quenched by cooling in a cold oil bath; *n*-heptane (40 mL) was added when the temperature reached 55 °C to prevent the octadecane solidifying. The final mixture was divided into four parts and MeOH (10 mL) was added to each part to precipitate Zn-St then acetone (2 x 10 mL). Sequential washing and centrifugation in CHCl_3 obtained a ZnSe-St solution. The precipitate was removed and washed sequentially in 1-butanol and MeOH before being dissolved in CHCl_3 (3-4 mL) and re-centrifuged. The cloudy upper layer and precipitate were discarded, and the clear middle layer stored as a stock solution at 4 °C.

ZnSe-BF₄ Nanorod Synthesis

Solvent was removed *in vacuo* from ZnSe-St QDs (6-10 mL stock solution), the residue re-dissolved in CHCl₃ (3 mL) and anhydrous DMF (0.2 mL) added under N₂. [Me₃O][BF₄] (1 M, acetonitrile, 3-5 mL) was added dropwise to form a precipitate. The precipitate was centrifuged, and the supernatant discarded, then re-dispersed in DMF and centrifuged to obtain a clear supernatant consisting of ZnSe-BF₄ nanorods. This solution was degassed by two freeze-pump-thaw cycles and stored under N₂ at 4 °C.

Mercaptoethylphosphonic Acid Synthesis

Diethyl 2-bromoethylphosphonate (4.08 mmol) was added to potassium thioacetate (4.49 mmol) and stirred under N₂ at room temperature for 5 min. 5 mL acetonitrile was added and the solution was stirred for 15 h under N₂. Bromotrimethylsilane in dry CHCl₃ was added (38 mmol, 2.2 equivalents) and the solution was stirred for 10 h under N₂. The obtained product was washed with methanol three times and dried, then re-dissolved and dried from toluene to obtain MEPA.

CuCrO₂|ZnSe Film Preparation

CuCrO₂ electrodes were prepared as outlined in Chapter 2 but with only 3 layers to give a film thickness of 300 nm. ZnSe was immobilized through dropcasting 8 μL cm⁻² of a stock solution (1.66 mg/mL, acetonitrile) and drying in air. CuCrO₂|ZnSe photoelectrodes were used directly after preparation with no further modification. ZnSe-MPA, ZnSe-MEPA, cross-linked EDT electrodes were formed through soaking for 15 h in ligand solution (1 mM, DMF) then in ZnSe-NRs (1.66 mg mL⁻¹, DMF, 2 h) followed by rinsing with DMF, H₂O, then were dried under N₂.

Physical Characterisation

SEM analysis was conducted using Tescan MIRA3 FEG-SEM. Energy-dispersive X-ray spectra were recorded with an Oxford Instruments Aztec Energy X-maxN 80 EDX system (20 kV, 15 mm working distance). TEM analysis was conducted using a FEI Phillips Technai F20-G2 TEM, operating at an accelerating voltage of 200 kV (Electron Microscopy Suite, Cavendish Laboratory, University of Cambridge). XRD measurements were taken with a PANalytical BV X'Pert Pro X-Ray Diffractometer. UV-Vis absorption spectra were acquired using a Varian Cary 50 spectrophotometer operated in transmission mode.

ICP-OES

ZnSe loading on CuCrO₂|ZnSe was determined using ICP-OES (Zn and Se quantification) following overnight digestion of electrodes (1 cm²) in aqueous HNO₃ (70%, 1 mL) and subsequent dilution to 10% v/v with MilliQ[®] H₂O. Triplicate results were obtained including solution and CuCrO₂ electrode blanks. The concentration of all stock solutions was determined from the Zn²⁺ concentration following digestion in HNO₃ and dilution. Solution blanks were recorded as the background concentration.

IPCE Measurements

A 3-electrode setup using an Ivium CompactStat potentiostat with a Pt-counter, Ag/AgCl/KCl_{sat} reference, and a CuCrO₂-based working electrode in a custom 3-necked cell with a flat borosilicate glass window was used for IPCE measurements. The electrolyte solution was Na₂SO₄ (0.1 M, pH 5.5) and an applied potential of 0.0 V vs. RHE maintained for all measurements. Monochromatic light was supplied with a 300 W Xenon lamp solar light simulator connected to a monochromator (MSH300, LOT Quantum design). The intensity was calibrated to 1 mW cm⁻² for each individual wavelength and experiments with CuCrO₂ and CuCrO₂|ZnSe electrodes were conducted in triplicate with different electrodes with an active area of 0.25 cm². Error bars represent standard deviation from the mean.

Photoelectrochemical Measurements

PEC measurements were conducted using an Ivium CompactStat potentiostat in a one-compartment 3-necked custom cell featuring a flat borosilicate window. A three-electrode setup was used with a Pt-counter, Ag/AgCl/KCl_{sat} reference, and a CuCrO₂-based working electrode (0.25 cm² active area). N₂-purged (15 min) aqueous Na₂SO₄ electrolyte solution (0.1 M, pH 5.5) was used for all measurements. Electrodes were illuminated from the front using a calibrated Newport Oriel solar light simulator (150 W, 100 mW cm⁻², AM 1.5G) with an IR water filter and a UQG Optics UV-Filter ($\lambda > 400$ nm).

CPPE experiments were conducted in triplicate at 0.0 V vs. RHE in a custom two-compartment electrochemical cell featuring a flat quartz window and a Nafion membrane divider. The working compartment volume was 11 mL with a gas headspace of 6 mL and the counter compartment contained 4.5 mL solution and a 3.5 mL headspace. Both compartments were purged with 2% CH₄ in N₂ for 30 min prior to electrolysis and the amount of H₂ determined using a Shimadzu Tracera GC2010 Plus gas chromatograph using a barrier ionisation

discharge (BID) detector and a molsieve column (kept at 130 °C) with He as the carrier gas. All PEC cells were left for 2 h following electrolysis to allow solution dissolved H₂ to equilibrate with the gas headspace. The partial pressure of H₂ was calculated to account for dissolved gas in the solution using Henry's law and this was added to the amount of H₂ to obtain the Faradaic efficiency.

Chapter 4

Next Generation CuCrO₂ Photocathodes for Dye-Sensitised H₂ Production

*This chapter forms the basis of a publication in preparation at the time of writing: 'Next Generation CuCrO₂ Photocathodes for Dye-Sensitised H₂ Production', In Preparation, C. E. Creissen, J. Warnan, D. Antón-García, F. Odobel and E. Reisner. All results presented were conducted solely by the author with contributions outlined. **DPP-P** was synthesised and characterised by Dr. Julian Warnan, **NiP** was synthesised by Daniel Antón-García, and **PMI-P** was synthesised and characterised by Dr. Yoann Farré in the group of Professor Fabrice Odobel (Université de Nantes).*

4.1. Introduction

In Chapters 2 and 3, mesoporous CuCrO₂ was shown to be an effective p-type semiconductor (p-SC) in dye-sensitised photocathodes (DSPCs). Production of only small amounts of H₂ in the molecular system was attributed to low catalyst and dye loadings – this chapter outlines a route to address the issue through nanostructuring. Two photocathodes formed using different organic photosensitisers with a co-immobilised molecular Ni catalyst are presented to highlight the influence of semiconductor morphology and molecular dye structure in DSPCs.

Incorporation of dye and catalyst molecules on metal oxides benefit from highly nanostructured electrodes that can accommodate a large number of surface-bound species. Studies have shown that orientation-dependent charge transfer of surface-immobilised species and packing of dye and catalyst components on the surface can influence activity,^{59,152,304} therefore, surface morphology is an important factor to consider when developing photocathode materials. Template-assisted bottom up approaches starting from nanoparticulate materials offer a straightforward route to nanostructuring, providing the nanoparticles (NPs) are dispersible; stable in mixtures with the template; and can be sintered to form interconnected networks.³⁰⁵ Development of hierarchical inverse opal (IO) structures has previously proven effective for incorporation of dye and catalyst components with metal oxide surfaces.^{122,137,306–313} Recently CuCrO₂ has been successfully employed as a platform for the development of quantum dot- and dye-sensitised electrodes for H₂ generation in water.^{190,297} However, low loadings of catalyst and dye on the surface has so far limited activity. Here, a method used to form metal oxide-based IOs was adapted to incorporate pre-formed

CuCrO₂-NPs.^{307,308} The hydrothermal procedure for CuCrO₂ is also likely to alter physical properties of the p-SC, therefore a comparison with sol-gel derived CuCrO₂ is made to evaluate the effect on performance.

Two organic dyes (**DPP-P** and **PMI-P**), based on diketopyrrolopyrrole (DPP) and perylene monoimide (PMI) structures were chosen for construction of IO-CuCrO₂ DSPCs with a co-immobilised Dubois-type Ni catalyst (**NiP**) (**Figure 4.1**). **DPP-P** has been successfully incorporated with **NiP** in a dye-sensitised photocatalysis (DSP) system with TiO₂-NPs⁸⁰ and in a molecular DSPC employing CuCrO₂ as the p-SC, outperforming an analogous NiO photocathode and generating a high TON for H₂ production (Chapter 2).²⁹⁷ **PMI-P** was recently used for H₂ generation in a DSP arrangement with **NiP**, where the phosphonic acid group enabled effective immobilisation.⁷⁹ Previous PMI-based photocathodes for H₂ generation have been established with heterogeneous catalysts¹⁴⁶ and with molecular catalysts in solution¹⁴⁸ but no current examples with an immobilised molecular catalyst exist. H₂ generation has been shown with perylene-dye-sensitised NiO electrodes in the absence of a catalyst,^{148,149} however catalysis was assigned to dissolution of Ni²⁺ from the NiO film and subsequent formation of a heterogeneous catalyst.¹⁴⁷ The problem with unintentionally introduced catalyst components can be avoided through immobilisation on CuCrO₂ with a well-defined and stable molecular catalyst.

Here, two organic dyes were co-immobilised on IO-CuCrO₂ structures with a molecular Ni catalyst to evaluate the influence of p-SC morphology and molecular dye structure on DSPC activity. Routes to formation of IO-CuCrO₂ electrodes are outlined with physical and electrochemical characterisation to provide an accessible p-SC architecture for DSPCs. Immobilisation of the molecular species and photoelectrochemical (PEC) analysis with H₂ generation provides insights into the factors that govern charge transfer in co-immobilised DSPCs. Future prospects for CuCrO₂-based DSPCs are outlined.

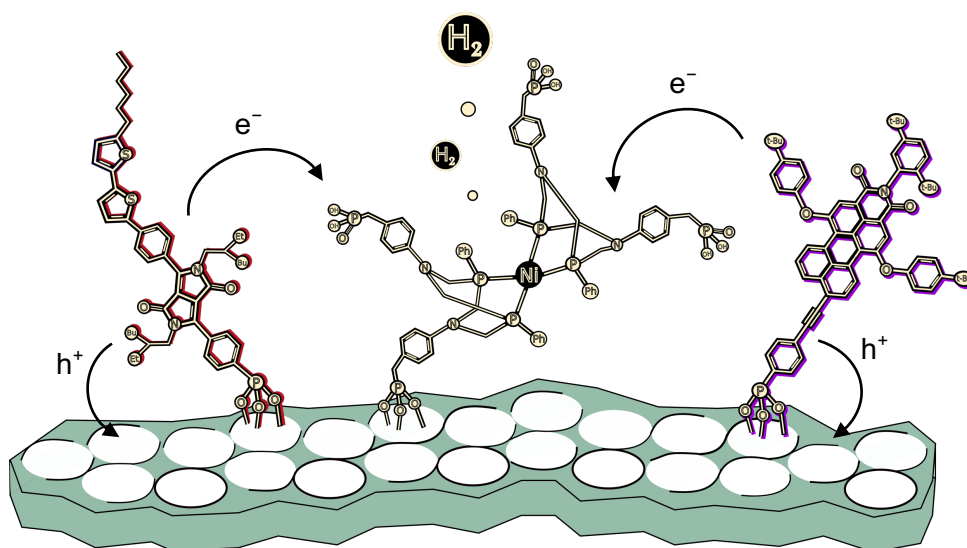


Figure 4.1 – Illustration of the two different dye structures (**DPP-P** and **PMI-P**) with co-immobilised **NiP** on IO-CuCrO₂.

4.2. Development of Inverse Opal Structures

A common method to construct IO electrodes uses evaporation-induced self-assembly of organic or silica microspheres. The template can be pre-assembled and infiltrated with a precursor solution for the material of choice, or a mixture of nanoparticles with the microspheres can be co-deposited on a substrate to construct the electrode.^{305,314–316} The template is subsequently removed to leave the IO-structured material. Silica requires etching in hydrofluoric acid, which precludes direct formation on ITO-glass substrates, therefore organic microspheres were required in this case. Conventionally, metal oxide IOs are formed by combustion of the organic template at high temperatures,³¹⁵ but with CuCrO₂ this was not possible due to the unfavourable formation of spinel phase CuCr₂O₄ in the presence of O₂.²²⁸ Instead, solvent dissolution of the template was used as previously reported with other metal oxide IO structures.³¹⁷ Here, a co-assembly method using CuCrO₂-NPs dispersed with polystyrene (PS) microspheres to form opal structures is outlined. Template removal using toluene and sintering under inert conditions enabled the construction of IO-CuCrO₂ electrodes.

4.2.1. CuCrO₂ Nanoparticle Synthesis and Characterisation

A previously reported hydrothermal synthesis was used to form CuCrO₂-NPs.²²⁸ A stoichiometric ratio of Cu(NO₃)₂·3H₂O and Cr(NO₃)₃·9H₂O were stirred in MilliQ[®] H₂O and NaOH added as a mineraliser. NaOH acts to increase the solubility of the solid constituents

and results in the formation of hydroxide species, $[\text{Cu}(\text{OH})_2]^-$ and $[\text{Cr}(\text{OH})_4]^-$, that react to form the delafossite structure.²⁴⁰ The resulting solution was added to a PTFE-lined autoclave and heated to 240 °C for 60 h. The particles were washed consecutively with dilute HCl and EtOH three times then dried *in vacuo*. The as-prepared nanoparticles were ground to a fine powder using a pestle and mortar before use.

Transmission electron microscopy (TEM) images of the CuCrO_2 -NPs showed highly crystalline particles with an average length of 15 ± 2 nm and diameter of 5.5 ± 0.5 nm (**Figure 4.2**). X-Ray diffraction (XRD) patterns displayed only peaks for the 3R ($R\bar{3}m$) delafossite polytype (**Figure 4.6**) and BET measurements gave a surface area of approximately $86 \text{ m}^2 \text{ g}^{-1}$, in line with reports using the same procedure.²²⁸

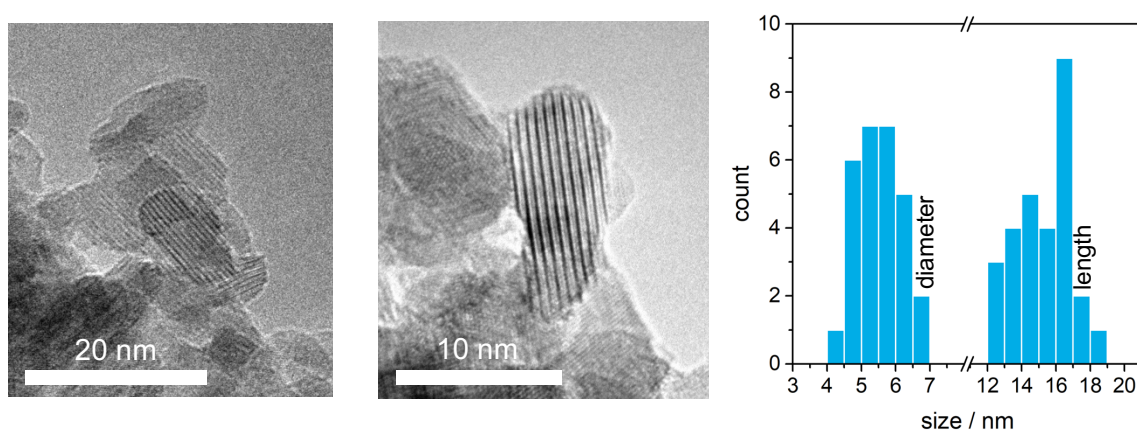


Figure 4.2 – TEM images and measured particle size distribution of CuCrO_2 -NPs.

4.2.2. CuCrO_2 Inverse Opal Structures

IO structured electrodes were prepared using a templating method through co-deposition of PS mixtures with CuCrO_2 -NPs. Key parameters for the development of IO structures were: the solvent mixture used to disperse the CuCrO_2 -NPs; the ratio of PS to CuCrO_2 ; and the deposition volume used. Room temperature was used for all optimisation studies to avoid problems associated with uneven heating. The basic protocol involved washing of the PS beads to remove the natant surfactant and addition of the CuCrO_2 -NP mixture followed by sonication (< 10 °C) to form a good dispersion. The dispersion was drop cast on pre-cleaned ITO-coated glass confined to a circular area (0.5 cm^2) with parafilm and left to dry in ambient conditions. The parafilm was removed and the PS template was dissolved in toluene. The resulting films were washed with acetone, then dried *in vacuo* (**Figure 4.3**). Post annealing at

500 °C under argon was required to sinter films and form the final IO-CuCrO₂ electrodes (see experimental section for full details).

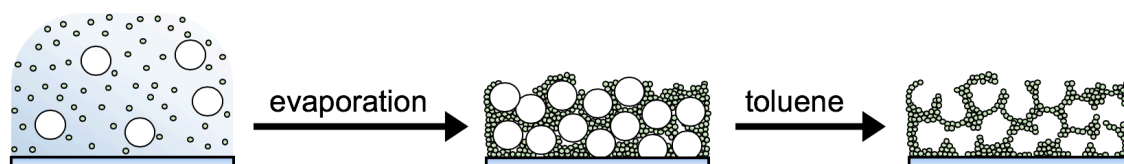


Figure 4.3 – Illustration of the co-deposition templating procedure and solvent removal steps used for the development of IO-CuCrO₂ films.

Methanol mixtures are capable of forming good dispersions with CuCrO₂-NPs, as has recently been reported with NPs synthesised using the same method.^{318,319} A ratio of 4:1 H₂O:MeOH provided the best mixture with PS beads in this case. Electrodes formed using this dispersion at high concentrations of CuCrO₂ (15 wt%) showed good structural integrity and clear interconnected pores. However, the thickness of these films was too high which prevented substantial light penetration, precluding usage in DSPCs (**Figure 4.4**). A lower concentration of CuCrO₂-NPs (7.5 wt%) was effective in affording thinner films. SEM images showed IO structure with interconnected pores (diameter of approximately 750 nm) and uniform thickness of 2 µm or 4 µm for drop casting volumes of 4 µL and 6 µL respectively (**Figure 4.5**).

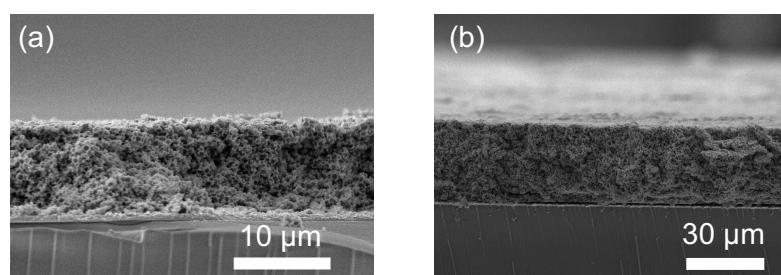


Figure 4.4 – Cross-sectional SEM images of IO-CuCrO₂ films formed using 15 wt% dispersions of CuCrO₂-NPs with a drop casting volume of a) 5 µL and b) 10 µL.

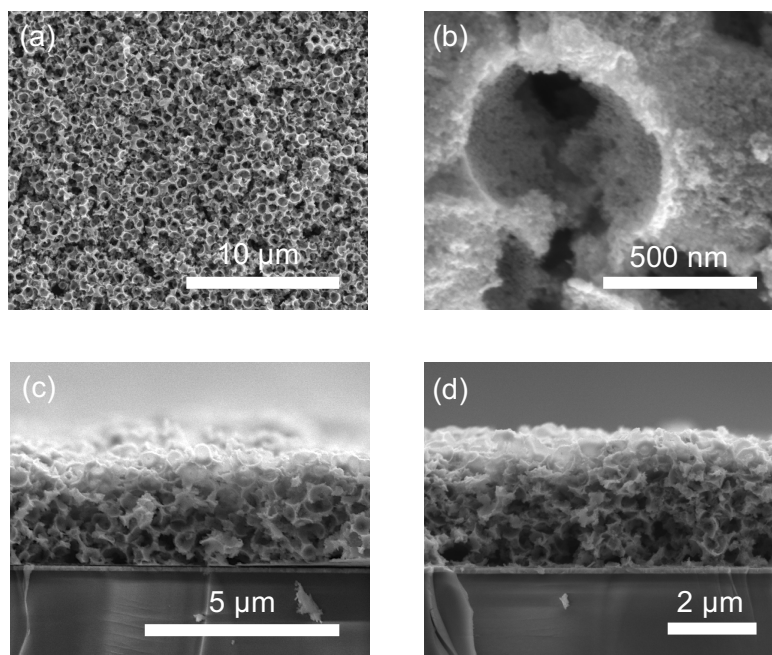


Figure 4.5 – SEM images of IO-CuCrO₂ films formed using 7.5 wt% dispersions of CuCrO₂-NPs: a) top-down SEM of the electrode, b) an isolated pore, c) drop casting volume of 4 μL, and d) drop casting volume of 6 μL.

XRD patterns displayed a dominant (006) peak, corresponding to preferential orientation with (00*l*) planes parallel to the ITO-glass as has previously been reported for preparation methods with similar delafossite structures (**Figure 4.6**).^{228,270,297} Upon formation of IO-CuCrO₂ films a narrowing of the XRD peaks was observed, consistent with crystal growth as expected from the sintering step.

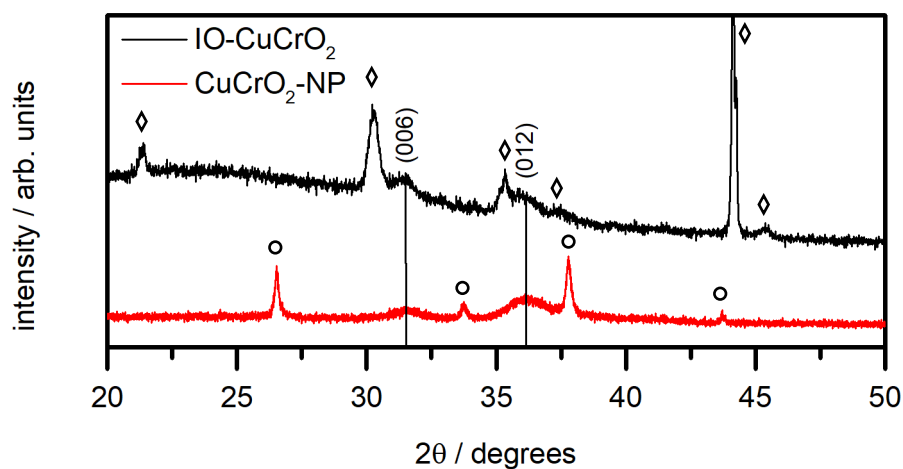


Figure 4.6 – XRD patterns for CuCrO₂-NPs (red) and IO-CuCrO₂ films (black) with peaks corresponding to the (006) and (012) 3R CuCrO₂ polytype labelled (ICSD collection code 026676). All other peaks are assigned to the ITO-glass (diamonds) SiO₂ (circles).

4.3. Photosensitiser Properties

The two dyes employed in this study are derivatives of PMI and DPP dyes featuring phosphonic acid groups that enable strong anchoring to metal oxide surfaces (**Figure 4.7**). The core structures of these dyes are particularly suited for sensitisation of p-SCs and both types of dye have previously been successfully incorporated in DSPCs.^{146–148,150,297}

Charge transfer between dye and semiconductor components is a proximity dependent process, where a higher degree of separation results in a lower rate.^{58,59,320} Therefore, with DSPCs it is important to locate the HOMO of the dye close to the anchoring group to ensure rapid hole injection from the photoexcited dye to the p-SC, but to also limit the recombination process between the photo-reduced dye and the p-SC by spatially removing the LUMO from the surface. Often recombination between the dye anion and holes in the p-SC is the dominant limiting factor, with rapid hole injection typically observed with organic dyes.^{124,152,206,321–323}

The core bicyclic lactam ring in **DPP-P** is electron withdrawing so acts as an internal acceptor unit and spatially removes the LUMO from the p-SC. Therefore, a lower susceptibility to recombination is expected as has been observed with similar structures.^{119,256} Additional structural features are also beneficial including the long alkyl chain to prevent desorption in H₂O, the thiophene rings that increase conjugation pushing the absorption profile towards longer wavelengths, and the side chains that prevent significant aggregation (see Chapter 2). The electron density distribution is dictated by acceptor and donor components of the molecular dye, which enable intramolecular charge transfer and assist charge separation.

In **PMI-P**, the LUMO is located preferentially on the PMI moiety, which is spatially removed from the p-SC, reducing the probability of recombination. **PMI-P** also features an ethynyl spacer, which couples the phosphonic acid anchoring group with the π -aromatic PMI structure – this ensures good overlap between the HOMO of the dye and p-SC, supporting fast hole injection. Therefore, **PMI-P** possesses key features for both hole injection and limited recombination making it highly suitable for coupling with CuCrO₂. The electron density distribution for HOMO and LUMO is centred mainly around the PMI unit, however the ethynyl bridge partially delocalises the HOMO producing a sizeable intramolecular charge transfer character as has been confirmed with DFT calculations.³²⁴

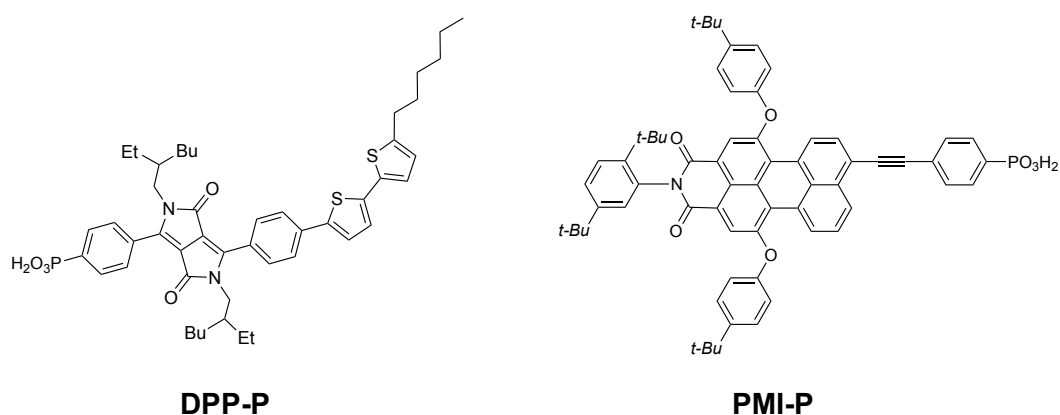


Figure 4.7 – Molecular structures of **DPP-P** and **PMI-P**.

UV-Vis spectra of both dyes were recorded in DMF. **PMI-P** shows a broad and intense signal from 450 – 600 nm with an absorption maximum at 536 nm ($\epsilon_{\max} = 3.8 \times 10^4 \text{ M}^{-1} \text{ cm}^{-1}$) and a shoulder at 500 nm. **DPP-P** also showed a broad signal (425 – 550 nm) with an absorption maximum centred at 496 nm ($\epsilon_{\max} = 2.6 \times 10^4 \text{ M}^{-1} \text{ cm}^{-1}$) (**Figure 4.8**, **Table 4.1**). The E_{00} values obtained from the intersection between the normalised absorption and emission spectra in DMF were 2.20 eV and 2.27 eV for **PMI-P** and **DPP-P** respectively (**Appendix**, **Figure A5**).

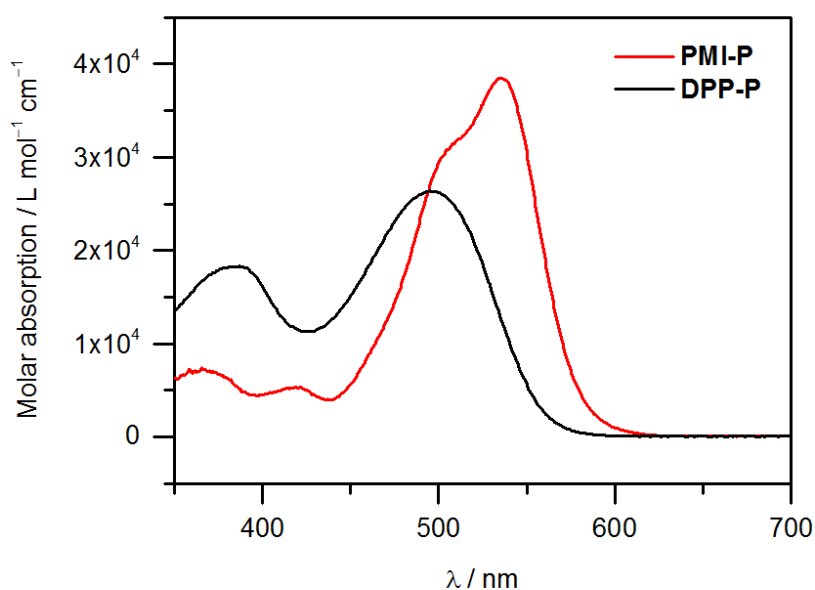


Figure 4.8 – UV-Vis spectra of **DPP-P** and **PMI-P** recorded in DMF.

Dyes generally tend to undergo reductive quenching when immobilised on p-SCs, whereby initial light excitation is followed by hole injection to generate a reduced dye species that can transfer an electron to the immobilised catalyst. **DPP-P** and **PMI-P** exhibit similar ground state reduction potentials (E_{S/S^-}) of approximately -0.7 V vs. NHE, providing sufficient driving force for reduction of **NiP** to a catalytically active state (**NiP** onset potential = -0.21 V vs. RHE).⁹⁷ **DPP-P** displays a more positive excited state reduction potential (E_{S^*/S^-}) than **PMI-P** by 100 mV indicating that hole injection into the valence band of CuCrO_2 ($E_{\text{fb}} = +1.0$ V vs. RHE) is slightly more thermodynamically favourable, but both exhibit sufficiently anodic potentials for hole injection (**Table 4.1**).

Table 4.1 – Maximum absorption wavelength (λ_{max}) with corresponding extinction coefficient (ϵ), zero-zero excitation energy (E_{00}), excited state reduction potential (E_{S^*/S^-}), and ground state reduction potential (E_{S/S^-}) for **PMI-P** and **DPP-P**.

Dye	λ_{max} (nm)	ϵ ($\text{M}^{-1} \text{cm}^{-1}$)	E_{00} (eV)	E_{S^*/S^-} (V vs. NHE)	E_{S/S^-} (V vs. NHE)
PMI-P	536	3.8×10^4	2.20	1.47	-0.73
DPP-P	496	2.6×10^4	2.27	1.57	-0.70

4.4. Photoelectrode Assembly and Characterisation

Photocathodes were assembled using a two-step procedure where initial anchoring of the dye was followed catalyst immobilisation. IO- CuCrO_2 electrodes were soaked in a solution of **PMI-P** (0.2 mM, DMF, 15 h) or **DPP-P** (0.2 mM, DMF, 15 h) before rinsing with DMF then H_2O . The resulting IO- CuCrO_2 |**dye** electrodes were dried under N_2 then immersed in a **NiP** solution (1 mM, MeOH) for 3 h in a N_2 atmosphere to form IO- CuCrO_2 |**dye/NiP** electrodes.

The colour change from light green to red and orange for IO- CuCrO_2 |**PMI-P/NiP** and IO- CuCrO_2 |**DPP-P/NiP** electrodes respectively, confirms successful dye anchoring through the phosphonic acid groups (**Figure 4.9**). The amount of anchored dye was determined using UV-vis spectroscopy following desorption of the dye in tetrabutylammonium hydroxide 30-hydrate (TBAOH, 0.1 M, DMF, see experimental section). The amount of **NiP** immobilised was determined using ICP-OES following digestion in nitric acid. The IO structure enables higher loading of both catalyst and dye species than with sol-gel derived CuCrO_2 , emphasising the key advantage of higher surface area structures for DSPCs (**Table 4.2**).

Table 4.2 – Dye and catalyst loadings for IO-CuCrO₂ and mesoporous CuCrO₂ electrodes.

Photocathode	Dye Loading (nmol cm ⁻²)	NiP Loading (nmol cm ⁻²)
IO-CuCrO ₂ PMI-P/NiP	11.4 ± 1.8	4.5 ± 0.9
IO-CuCrO ₂ DPP-P/NiP	14.8 ± 1.6	4.5 ± 0.4
CuCrO ₂ DPP-P/NiP ^a	2.6 ± 0.7	0.8 ± 0.4

^a Taken from previous work (Chapter 2).²⁹⁷

UV-Vis spectra of IO-CuCrO₂|**dye/NiP** samples displayed a clear enhancement in absorption in the visible region over the bare IO-CuCrO₂ films (**Figure 4.9**). The inversion of intensities of the absorption maxima at 500 and 536 nm for IO-CuCrO₂|**PMI-P** electrodes is representative of aggregation which is known to alter vibronic peak intensities.^{79,325}

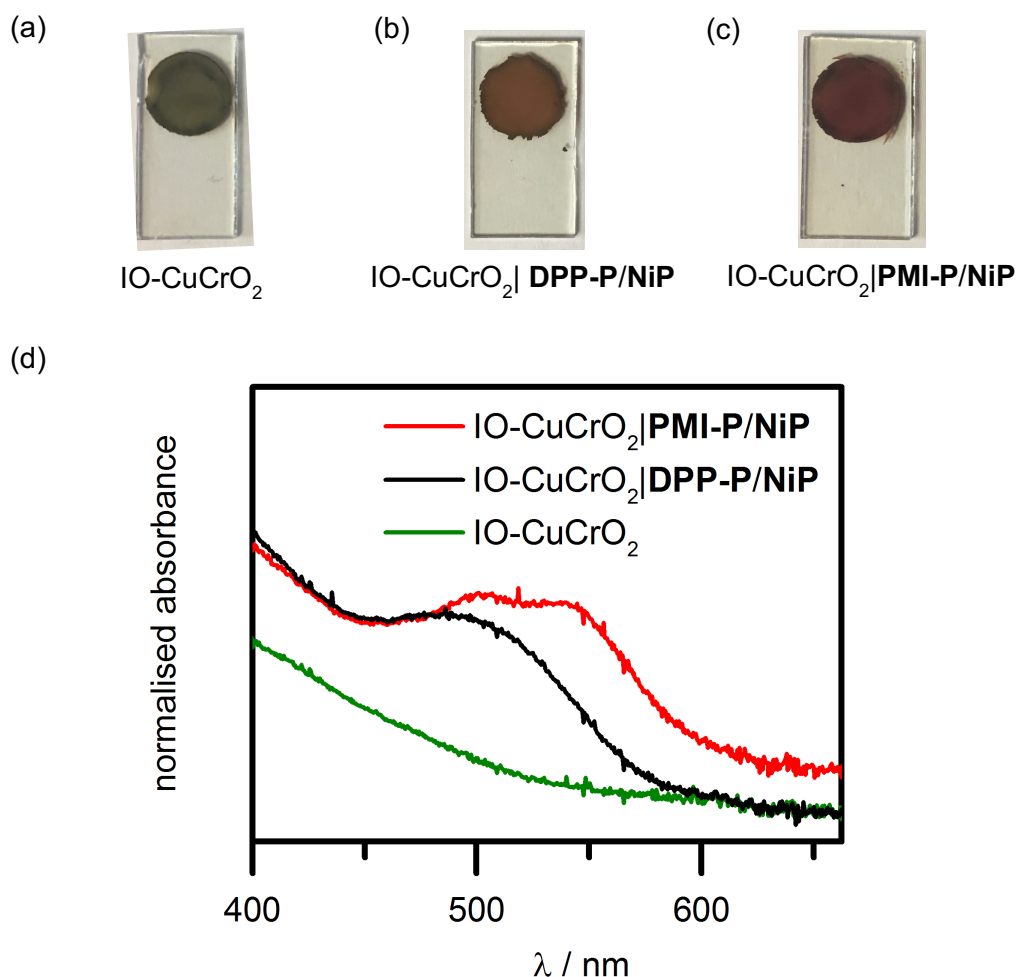


Figure 4.9 – Photographs of a) IO-CuCrO₂, b) IO-CuCrO₂|DPP-P/NiP, and c) IO-CuCrO₂|PMI-P/NiP electrodes, d) corresponding UV-Vis spectra of each photocathode obtained using a diffuse reflectance accessory.

4.5. IO-CuCrO₂ Acceptor Studies

To probe the IO-CuCrO₂|**dye** interface, tests with a sacrificial electron acceptor (SEA) in solution were conducted. The photocurrent is highly representative of the hole injection efficiency, as the transfer of electrons from the dye to the acceptor should be less kinetically limited than the corresponding charge transfer to a surface-bound catalyst. A maximum theoretical photocurrent for this reduction reaction infers a higher possibility of reducing a molecular catalyst, disregarding the specific dye/catalyst interaction. 4,4'-dithiodipyridine (DTDP) was chosen as the SEA due to the accessible reduction potential (-0.06 V vs. RHE) and its previous use in a CuCrO₂|**DPP-P** system.²⁹⁷

4.5.1. Thickness Variation with DPP-P

Chronoamperometry experiments were conducted at +0.3 V and 0.0 V vs. RHE in the presence of DTDP using IO-CuCrO₂|**DPP-P** electrodes with two different thickness (2 and 4 μm). The highest photocurrents were observed with 2 μm thick samples, achieving up to -160 μA cm⁻² at 0.0 V vs. RHE and -135 μA cm⁻² at +0.3 V vs. RHE. The 4 μm thick samples gave significantly lower photocurrents of -100 μA cm⁻² at 0.0 V vs. RHE and -80 μA cm⁻² at +0.3 V vs. RHE (**Figure 4.10**). As outlined in Chapter 2, Section 2.4, the beneficial loading of dye in thicker films is counteracted by a decrease in the charge collection efficiency owing to the film thickness becoming larger than the effective diffusion length of holes, hence increasing the rate of recombination. Furthermore, the decrease in transparency limits excitation and subsequent hole injection from dye molecules immobilised throughout the film. The hydrophobicity of the dye-sensitised electrodes is also extremely high in IO structures, which may limit significant penetration of the SEA throughout the entirety of the film in the thicker samples (**Appendix, Figure A6**). The combination of these factors resulted in the best performance with 2 μm thick films. These IO-CuCrO₂ electrodes were used for all further experiments.

The increase in dark current at more cathodic potentials is associated with Cu²⁺ reduction to Cu⁺ and oxygen deintercalation as observed with sol-gel derived CuCrO₂ (Chapter 2). Thicker films also showed a larger dark current, reflective of the higher proportion of Cu²⁺ defects in contact with the electrolyte solution as well as an associated increase in capacitance. This is discussed in more detail with respect to the full photocathodes in Section 4.6.

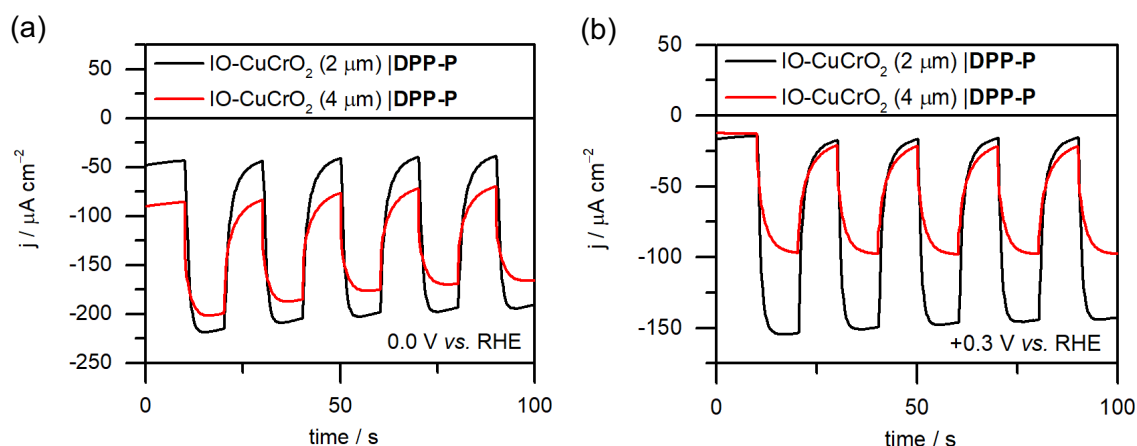


Figure 4.10 – Chronoamperometry experiments at applied potentials of a) 0.0 V and b) +0.3 V vs. RHE with IO-CuCrO₂|DPP-P electrodes under chopped light illumination (100 mW cm⁻², AM 1.5G, $\lambda > 420$ nm) in the presence of DTDP (5 mM in 0.1 M Na₂SO₄, pH 4.6). Electrode active area of 0.25 cm² was used in all cases.

4.5.2. Comparison of PMI-P and DPP-P

Chronoamperometry experiments at an applied potential of +0.3 V vs. RHE showed similar performance for IO-CuCrO₂|PMI-P and IO-CuCrO₂|DPP-P electrodes ($j \approx -135 \mu\text{A cm}^{-2}$). However, at 0.0 V vs. RHE, the PMI-P-sensitised electrodes displayed higher photocurrents ($j \approx -180 \mu\text{A cm}^{-2}$) than the corresponding DPP-P-sensitised electrodes ($j \approx -160 \mu\text{A cm}^{-2}$) (Figure 4.11).

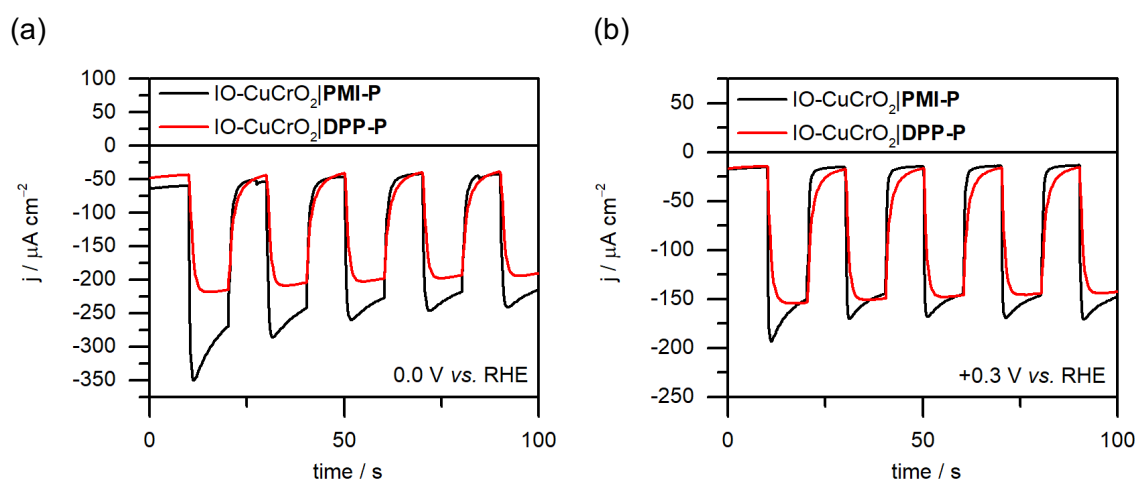


Figure 4.11 – Chronoamperometry experiments at applied potentials of a) 0.0 V and b) +0.3 V vs. RHE with IO-CuCrO₂|DPP-P and IO-CuCrO₂|PMI-P electrodes under chopped light illumination (100 mW cm⁻², AM 1.5G, $\lambda > 420$ nm) in the presence of DTDP (5 mM in 0.1 M Na₂SO₄, pH 4.6). Electrode active area of 0.25 cm² was used in all cases.

These results suggest that **PMI-P** is capable of generating higher photocurrents than **DPP-P** when integrated with IO-CuCrO₂. The better performance is associated in part to the higher extinction coefficient and longer λ_{max} for **PMI-P**, which enables absorption of a higher portion of the visible region. As more cathodic potentials are applied, the photocurrent rapidly grows for IO-CuCrO₂|**PMI-P** electrodes, suggesting slower recombination with decreased driving force. This corresponds well with previous studies on NiO, where PMI dyes are known to exhibit Marcus normal behaviour.²⁴⁸

A dominant factor contributing to low performance of DSPCs is fast recombination between the photoexcited hole in the semiconductor and the reduced sensitizer.^{130,249} With IO-CuCrO₂|**DPP-P** and IO-CuCrO₂|**PMI-P** electrodes, the high photocurrents suggest that rapid transfer of photoexcited holes is possible when an efficient electron acceptor is present, reflecting the beneficial structural features of these dyes for sensitisation of p-SCs. However, the ability of each dye to reduce an immobilised catalyst is not represented here as specific dye/catalyst interactions are not accounted for with a SEA in solution. Additionally, recombination between the reduced catalyst and the p-SC is not represented, which is known to negatively impact performance.^{121,152,205–207} Therefore, to establish working DSPC architectures with these dyes, **NiP** was co-immobilised on the IO surface.

4.6. Photoelectrochemical H₂ Generation

PEC experiments were conducted in aqueous conditions (Na₂SO₄, 0.1 M, pH 3) using IO-CuCrO₂|**dye/NiP** electrodes. Linear sweep voltammograms (LSVs) under chopped light illumination (100 mW cm⁻², AM 1.5G, $\lambda > 420$ nm) showed that cathodic photocurrents were obtained using both dyes with an onset potential located at approximately +0.8 V vs. RHE (**Figure 4.12**).

Chronoamperometry experiments conducted at an applied potential of +0.3 V vs. RHE showed only slightly higher photocurrents for IO-CuCrO₂|**PMI-P/NiP** ($j \approx -15 \mu\text{A cm}^{-2}$) than IO-CuCrO₂|**DPP-P/NiP** ($j \approx -12 \mu\text{A cm}^{-2}$) electrodes (**Figure 4.13**). However, at 0.0 V vs. RHE, IO-CuCrO₂|**PMI-P/NiP** electrodes generated much higher photocurrents ($j \approx -25 \mu\text{A cm}^{-2}$) than IO-CuCrO₂|**DPP-P/NiP** electrodes ($j \approx -18 \mu\text{A cm}^{-2}$) (**Figure 4.14**). These results correspond well with photocurrents obtained using a SEA, where increasing potential has a greater effect on **PMI-P**-sensitised electrodes than on the corresponding **DPP-P** electrodes, again hinting at Marcus normal behaviour of the PMI dye.²⁴⁸ This is also representative of the greater driving force for hole injection exhibited by the DPP dye (**Table 4.1**), which causes the current to plateau at more anodic potentials.

In all cases, the dark current stemming from CuCrO_2 increases with decreasing potential as was observed with mesoporous CuCrO_2 films (see Chapter 2).²⁹⁷ **PMI-P**-sensitised electrodes showed large transient photocurrent spikes, which have previously been attributed to accumulation of electrons at the catalyst in similar systems.⁹⁸ However, these spikes are not present when DTDP is used, suggesting that the cause is more likely related to charge transfer processes relating to the dye/p-SC or p-SC/solution interface. Other possible causes include trapped holes, high transport resistance, and fast charge recombination between the catalyst and holes in the p-SC, all of which are possible in the current system.⁴⁹ Further assignment of these photocurrent spikes could reveal catalysis-limiting processes in the system, however this requires transient spectroscopic analysis and is beyond the scope of the current work.

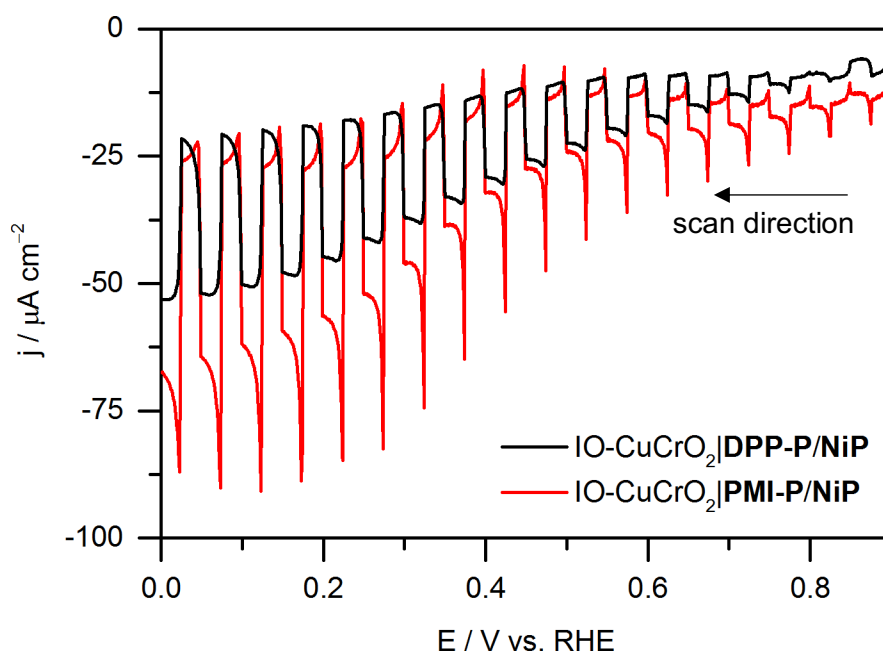


Figure 4.12 – LSVs of $\text{IO-CuCrO}_2|\text{DPP-P/NiP}$ and $\text{IO-CuCrO}_2|\text{PMI-P/NiP}$ electrodes under chopped light illumination (100 mW cm^{-2} , AM 1.5G, $\lambda > 420 \text{ nm}$) in Na_2SO_4 , (0.1 M, pH 3) with a scan rate of 5 mV s^{-1} . Electrode active area of 0.25 cm^2 was used in both cases.

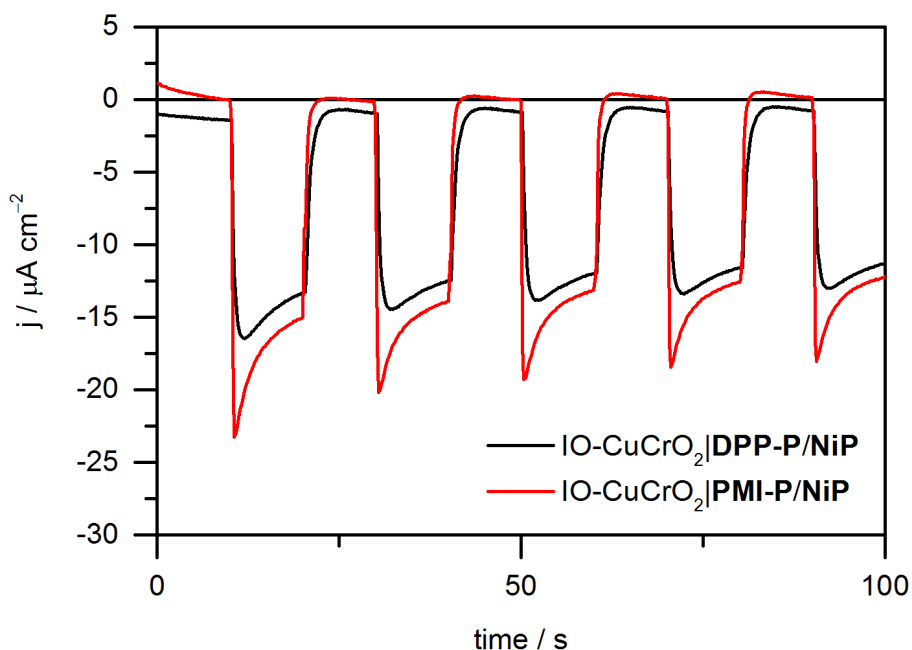


Figure 4.13 – Chronoamperometry experiments at an applied potential of +0.3 V vs. RHE with IO-CuCrO₂|DPP-P/NiP and IO-CuCrO₂|PMI-P/NiP electrodes under chopped light illumination (100 mW cm⁻², AM 1.5G, λ > 420 nm) in Na₂SO₄, (0.1 M, pH 3). Electrode active area of 0.25 cm² was used in both cases.

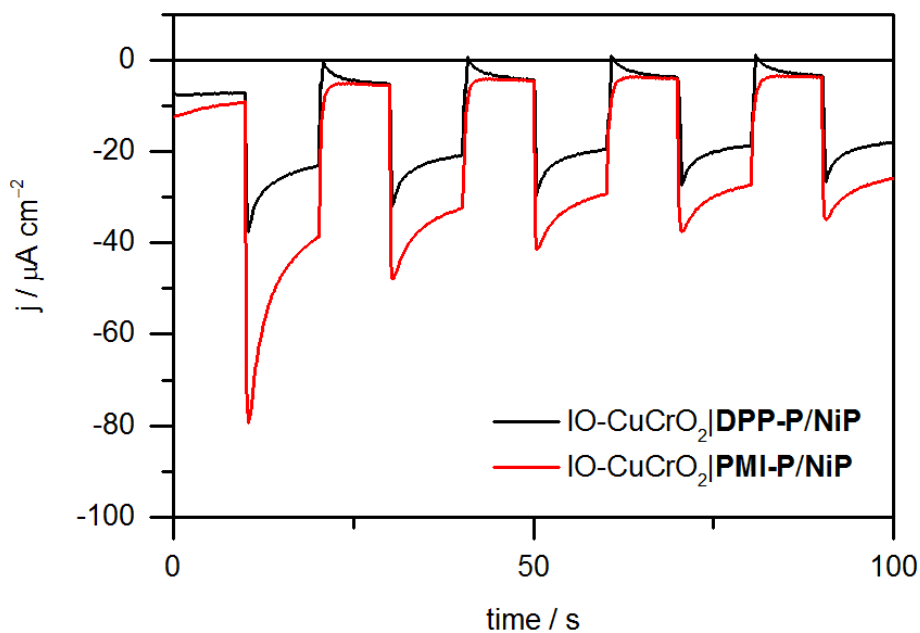


Figure 4.14 – Chronoamperometry experiments at an applied potential of 0.0 V vs. RHE with IO-CuCrO₂|DPP-P/NiP and IO-CuCrO₂|PMI-P/NiP electrodes under chopped light illumination (100 mW cm⁻², AM 1.5G, λ > 420 nm) in Na₂SO₄, (0.1 M, pH 3). Electrode active area of 0.25 cm² was used in both cases.

Low photocurrents ($< -5 \mu\text{A cm}^{-2}$ at 0.0 V vs. RHE) were observed for all IO-CuCrO₂ and IO-CuCrO₂|**dye** electrodes (**Figure 4.15**). Interestingly, the dark current was shown to decrease upon immobilisation of the molecular components in both systems. To probe if this was an effect of the anchoring group or related to the removal of capacitive current due to poor catalysis, an insulating organic molecule (phenylphosphonic acid) was immobilised on bare IO-CuCrO₂. Electrolysis under dark conditions with an IO-CuCrO₂|phenylphosphonic acid electrode displayed a lower dark current than the corresponding IO-CuCrO₂ electrode at an applied potential of 0.0 V vs. RHE (**Figure 4.16**).

The result shows that phosphonic acid groups are capable of passivating sites responsible for dark electrochemical processes in IO-CuCrO₂ electrodes. Phosphonic acids anchor to metal oxides through stable M-O-P bonds³²⁶ and alkylphosphonic acids have previously shown good binding affinity for Cu-based surfaces.³²⁷ In this case, the suppression of dark current provides convincing evidence for the passivation of Cu(II) defects that are responsible for the Cu^{II}/Cu^I redox process, which becomes more prominent at cathodic potentials as identified in previous reports (Chapter 2).^{231,270,297}

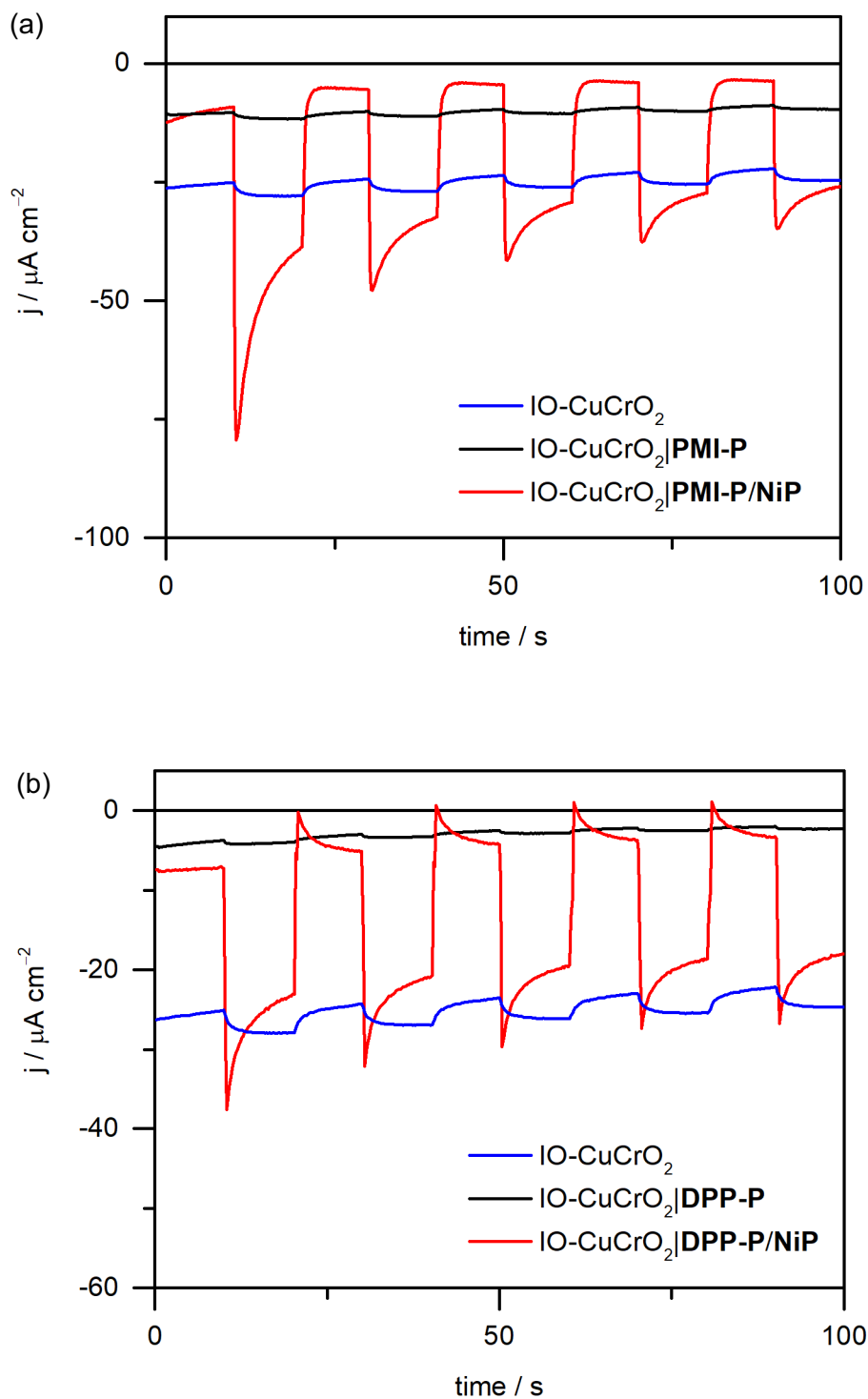


Figure 4.15 – Chronoamperometry experiments at an applied potential of 0.0 V vs. RHE with a) IO-CuCrO₂, IO-CuCrO₂|PMI-P, and IO-CuCrO₂|PMI-P/NiP electrodes and b) IO-CuCrO₂, IO-CuCrO₂|DPP-P, and IO-CuCrO₂|DPP-P/NiP electrodes under chopped light illumination (100 mW cm⁻², AM 1.5G, $\lambda > 420$ nm) in Na₂SO₄, (0.1 M, pH 3). Electrode active area of 0.25 cm² was used in all cases.

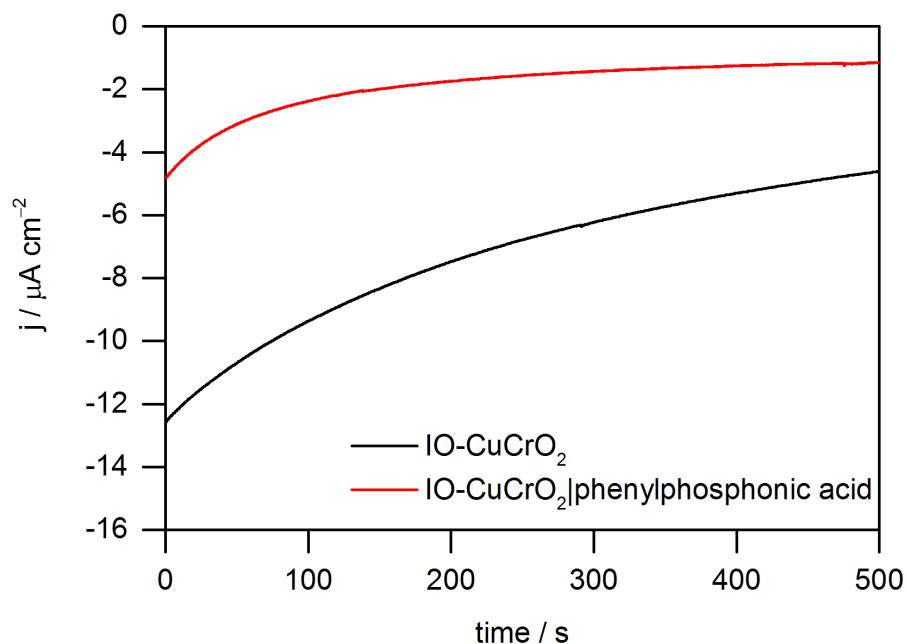


Figure 4.16 – Dark electrolysis of IO-CuCrO₂ and IO-CuCrO₂|phenylphosphonic acid electrodes. Conditions: aqueous Na₂SO₄ (0.1 M, pH 3), 0.0 V vs. RHE, 0.25 cm² active electrode area.

Incident photon-to-current efficiency (IPCE) measurements were conducted at +0.3 V vs. RHE for IO-CuCrO₂, IO-CuCrO₂|DPP-P/NiP, and IO-CuCrO₂|PMI-P/NiP electrodes (**Figure 4.17**). The broader range and higher values obtained with **PMI-P** reflect the higher capacity to absorb visible light and transfer a photoexcited electron to the immobilised catalyst. IO-CuCrO₂|**PMI-P/NiP** electrodes show an inversion of the maxima indicating that aggregates may contribute to photocurrent. The IPCE spectra correspond well with photocurrents observed in chronoamperometry experiments, with **PMI-P**-sensitised electrodes showing higher performance than the corresponding **DPP-P**-sensitised electrodes. The small IPCE values for IO-CuCrO₂ electrodes at $\lambda < 420$ nm are associated with light absorption in the p-SC itself, but lack of H₂ detection with blank electrodes points to photodegradation of the material itself or highly limited catalysis, which generates negligible amounts of H₂.

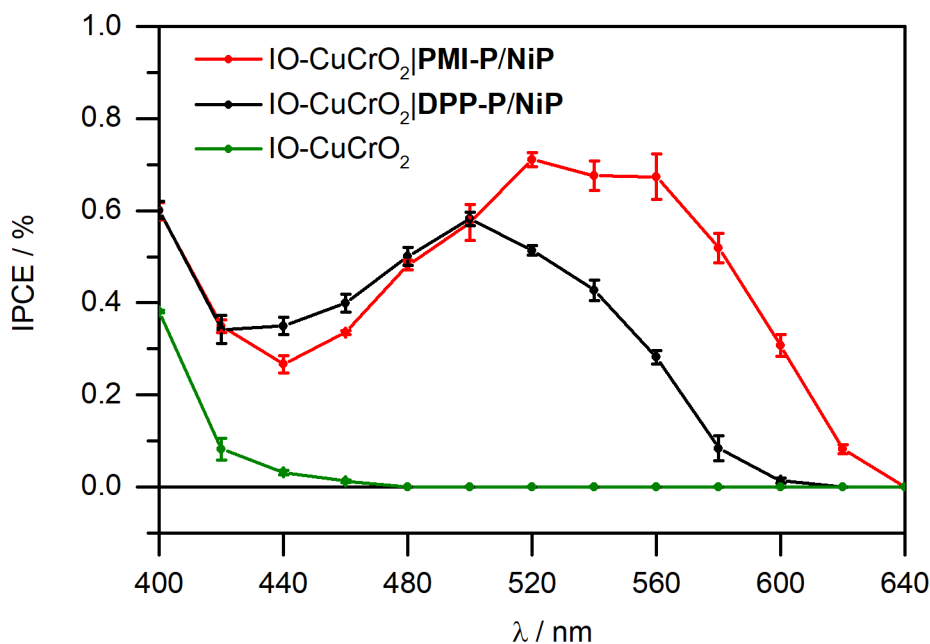


Figure 4.17 – Incident photon-to-current efficiency measurements for IO-CuCrO₂ (green), IO-CuCrO₂|DPP-P/NiP (black), and IO-CuCrO₂|PMI-P/NiP (red) electrodes measured in Na₂SO₄ (0.1 M, pH 3) with light intensity of 0.8 mW cm⁻² and the applied potential maintained at +0.3 V vs. RHE.

H₂ evolution was evaluated following controlled potential photoelectrolysis (CPPE) conducted with each IO-CuCrO₂|dye/NiP electrode at applied potentials of +0.3 V and 0.0 V vs. RHE for 2 h under simulated solar illumination (100 mW cm⁻², AM 1.5G, λ > 420 nm) (**Figure 4.18**). Each cell was left to equilibrate for 2 h following electrolysis to allow the maximum amount of H₂ to enter the headspace prior to gas chromatography (GC) analysis. Product analysis showed that at +0.3 V vs. RHE, IO-CuCrO₂|PMI-P/NiP electrodes generated 184 ± 22 nmol_{H₂} cm⁻² (FE = (45 ± 6)%) and IO-CuCrO₂|DPP-P/NiP electrodes produced 72 ± 25 nmol_{H₂} cm⁻² (FE = (25 ± 2)%). At 0.0 V vs. RHE the amount of H₂ increased for both electrodes (IO-CuCrO₂|PMI-P/NiP: 215 ± 10 nmol_{H₂} cm⁻², FE = (41 ± 8)%, TON_{NiP} = 48 ± 2 and IO-CuCrO₂|DPP-P/NiP: 160 ± 24 nmol_{H₂} cm⁻², FE = (40 ± 14)%, TON_{NiP} = 36 ± 5), indicating a higher ability of the DSPCs to function at more cathodic applied potentials (**Figure 4.19**, **Table 4.3**). No H₂ was observed in the absence of dye and/or catalyst at either potential, confirming the need for both molecular species in order for the photocathode to operate. Bare IO-CuCrO₂ electrodes showed a small photocurrent response (**Appendix**, **Figure A7**) but the lack of H₂ indicates that either negligible H₂ is generated below the detection limit of the GC instrument, or that the photocurrent is representative of degradation of the material itself as has been observed with other delafossite materials.^{222,300}

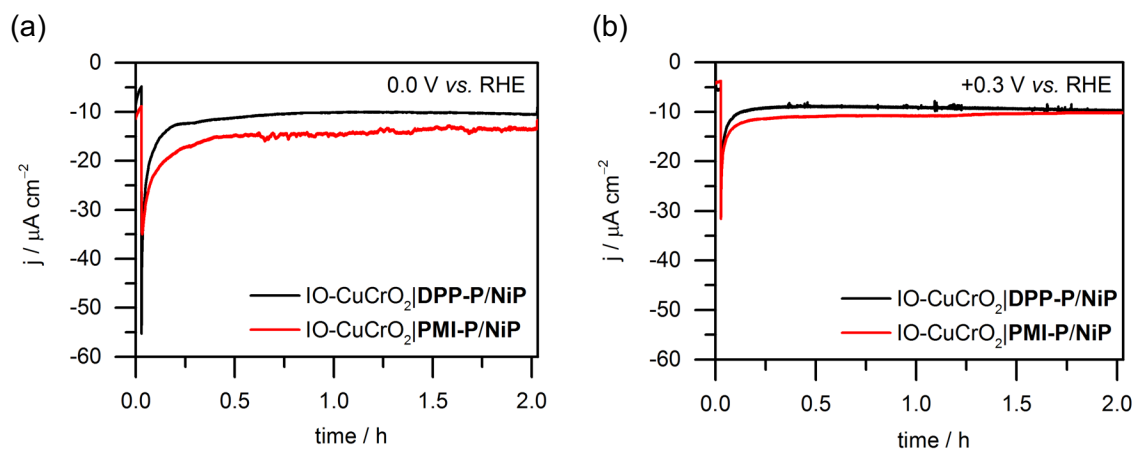


Figure 4.18 – CPPE over 2 h at an applied potential of a) 0.0 V vs. RHE and b) +0.3 V vs. RHE with IO-CuCrO₂|DPP-P/NiP and IO-CuCrO₂|PMI-P/NiP electrodes under visible light illumination (100 mW cm⁻², AM 1.5G, $\lambda > 420$ nm) in Na₂SO₄, (0.1 M, pH 3). Electrode active area of 0.25 cm² was used in all cases.

Table 4.3 – Amount of H₂ generated, TON_{NiP}, and FE for each photoelectrode following CPPE at +0.3 V and 0.0 V vs. RHE for 2 h.

Applied Potential	+0.3 V vs. RHE			0 V vs. RHE			
	Electrode ^a	H ₂ (nmol cm ⁻²)	TON _{NiP} ^b	FE (%)	H ₂ (nmol cm ⁻²)	TON _{NiP} ^b	FE (%)
IO-CuCrO ₂	-	-	-	-	-	-	-
IO-CuCrO ₂ PMI-P	-	-	-	-	-	-	-
IO-CuCrO ₂ PMI-P/NiP	184 ± 22	41 ± 5	45 ± 6	215 ± 10	48 ± 2	41 ± 8	
IO-CuCrO ₂ DPP-P	-	-	-	-	-	-	
IO-CuCrO ₂ DPP-P/NiP	72 ± 9	16 ± 2	25 ± 1	160 ± 24	36 ± 5	40 ± 14	
CuCrO ₂ DPP-P/NiP ^d	<i>n.r</i> ^c	<i>n.r</i> ^c	<i>n.r</i> ^c	94 ± 10	126 ± 13	34 ± 8	

^a Conditions: aqueous Na₂SO₄ (0.1 M, pH 3), UV-filtered simulated solar light (100 mW cm⁻², AM 1.5G, $\lambda > 420$ nm, 25 °C), electrode active area of 0.25 cm². ^b Calculated using catalyst loading determined from ICP-OES, ^c *n.r* = not reported, ^d taken from previous report (Chapter 2).²⁹⁷

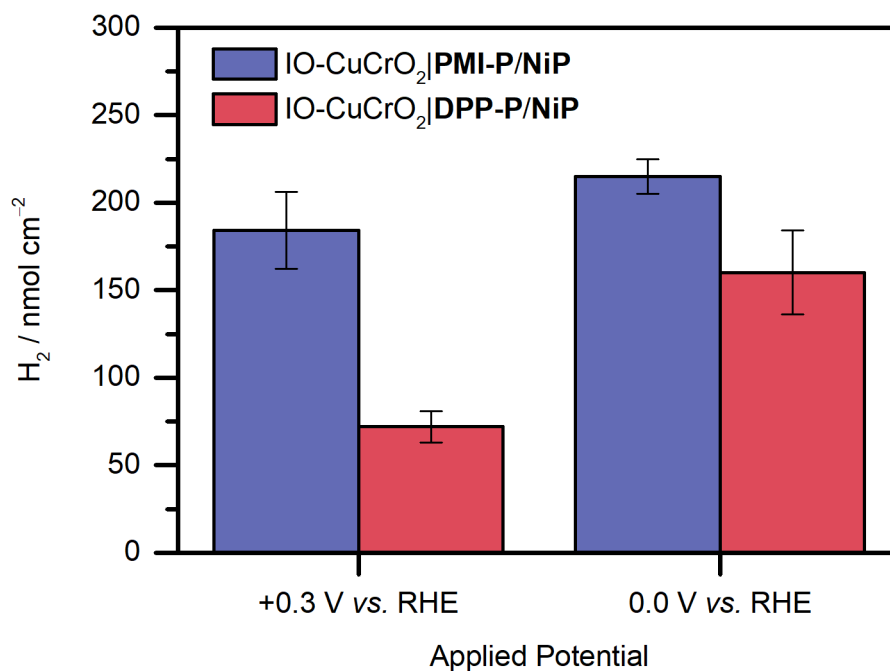


Figure 4.19 – Comparison of CPPE results at applied potentials of 0.0 V vs. RHE and +0.3 V vs. RHE with IO-CuCrO₂|DPP-P/NiP and IO-CuCrO₂|PMI-P/NiP electrodes. Conditions: visible light illumination (100 mW cm⁻², AM 1.5G, λ > 420 nm), aqueous Na₂SO₄ (0.1 M, pH 3), electrode active area of 0.25 cm². Error bars represent standard deviation from the mean.

The **DPP-P** sensitised inverse opal structures sustained higher long-term photocurrents ($-12 \mu\text{A cm}^{-2}$) than sol-gel CuCrO₂ films ($-7.5 \mu\text{A cm}^{-2}$) over 2 h CPPE at 0.0 V vs. RHE (**Figure 4.20**). Additionally, the dark current decrease accounts for the higher FE with IO electrodes. The overall amount of H₂ generated is improved by approximately 70% for the nanostructured electrodes. The results show that morphological alterations can have a direct impact on activity with identical catalyst and dye components. With IO-CuCrO₂, thicker films could be employed as direct channels for hole transport are available unlike with sol-gel films, where increasing the thickness beyond 500 nm decreased performance owing to the denser surface structure. This enabled higher loadings of catalyst and dye species and ultimately accounts for the improved performance.

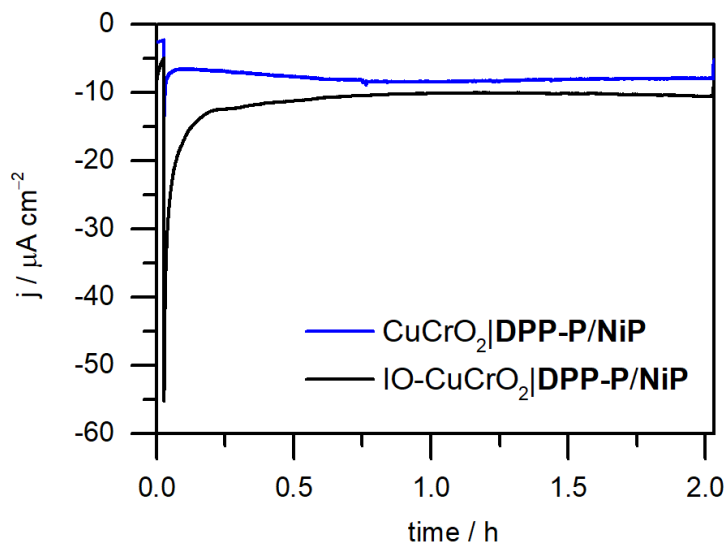


Figure 4.20 – CPPE over 2 h at an applied potential of a) 0.0 V vs. RHE IO-CuCrO₂|DPP-P/NiP and CuCrO₂|DPP-P/NiP (sol-gel) electrodes under visible light illumination (100 mW cm⁻², AM 1.5G, λ > 420 nm) in Na₂SO₄, (0.1 M, pH 3).

The results show that both **PMI-P** and **DPP-P** are effective dyes for sensitisation of IO-CuCrO₂. Good overall performance is attributed to properties of the nanostructured CuCrO₂, in which high surface area facilitates stable anchoring of relatively large amounts of molecular species. The effect of p-SC morphology is exemplified by the higher product yields obtained for IO-structured electrodes over the previously reported mesoporous films. Post-catalysis ICP-OES showed that approximately 85% and 75% of the catalyst was retained on the surface of IO-CuCrO₂|**PMI-P/NiP** and IO-CuCrO₂|**DPP-P/NiP** electrodes respectively following CPPE for 2 h at 0.0 V vs. RHE. Corresponding mesoporous CuCrO₂|**DPP-P/NiP** photocathodes retained around 50% of the catalyst, suggesting that the immobilised **NiP** is more stable in the IO-CuCrO₂ structures. The losses are reflective of shortcomings associated with phosphonate anchors in aqueous solutions, where hydrolysis and electrochemically assisted decomposition often results in cleavage of bound species.^{272,273} Recent reports using polymer assemblies³²⁸ and silane anchoring groups³²⁹ have shown high stability, offering routes to DSPEC devices with longer operational lifetimes.

The molecular dye structures are both well-suited for sensitisation of p-SCs. **DPP-P** has an internal acceptor unit that spatially removes the LUMO from the p-SC, limiting recombination between the reduced sensitiser with holes in CuCrO₂. **PMI-P** has a similar accepting effect with the PMI moiety, limiting recombination, but also has an additional functional feature in the ethynyl group which increases overlap between the dye's HOMO and the p-SC, enhancing hole injection. In general, IO-CuCrO₂|**PMI-P/NiP** photocathodes showed higher performance

than IO-CuCrO₂|**DPP-P**/NiP. This is attributed to the structural features discussed as well as the higher extinction coefficient, which enables absorption of a higher proportion of visible-light. Spectroscopic analysis of these systems to give some insight into the exact timescales for charge injection, recombination, and catalyst reduction, is currently underway.

The reported FE of approximately 40% for both systems is high for DSPCs with co-immobilised molecular components; this is partly representative of the high amounts of H₂ generated, which removes some inaccuracy related to detection of H₂ in the gas headspace.¹⁹⁸ However, a portion of the current is related to dark electrochemical processes associated with the CuCrO₂ electrodes themselves, which does not contribute to catalysis, as previously observed in similar systems.^{270,297} Methods to reduce or eliminate the non-Faradaic current would further improve the efficiency. Addressing issues with trap states in NiO has shown improvement in device performance,^{215,216} therefore similar understanding and passivation of such states in CuCrO₂ could prove effective. The adsorption of phenylphosphonic acid on bare IO-CuCrO₂ was shown to reduce the dark current in this case, suggesting that higher surface coverage reduced the non-Faradaic current. Similar analogues to block specific sites on the p-SC surface could improve performance of DSPCs, whilst simultaneously decreasing aggregation.

In both DSPCs, dye aggregates are highly probable. The **PMI-P**-sensitised electrodes show an inversion in absorption maxima, which is representative of aggregation (**Figure 4.9**).^{79,325} Although there is no clear evidence of aggregate formation in the UV-Vis spectrum of **DPP-P**, it is likely that π - π stacking occurs which is known to limit emission.^{256,330} Methods to reduce aggregation through co-immobilisation of chenodeoxycholic acid or other co-adsorbents have proven effective in other systems.^{142,225,331,332} These studies have also alluded to the benefits of co-adsorbents with regards to passivation of surface states that contribute to recombination,²²⁵ similar to the proposed passivation of Cu(II) defect sites in the systems presented here.

4.7. Conclusions

Photocathodes based on IO-CuCrO₂ were constructed using two different organic dyes with a co-immobilised molecular Ni-bis(diphosphine) catalyst. IO-CuCrO₂|**PMI-P/NiP** and IO-CuCrO₂|**DPP-P/NiP** electrodes generated photocurrents of $-25 \mu\text{A cm}^{-2}$ and $-18 \mu\text{A cm}^{-2}$ at 0.0 V vs. RHE under visible light illumination ($\lambda > 420 \text{ nm}$), with a photocurrent onset potential at around +0.8 V vs. RHE. **DPP-P** and **PMI-P**-sensitised photocathodes both generated appreciable amounts of H₂ over the course of 2 h CPPE. The performance of IO-CuCrO₂|**PMI-P/NiP** was the highest, producing $215 \pm 10 \text{ nmol}_{\text{H}_2} \text{ cm}^{-2}$ at 0.0 V vs. RHE with a FE of $(41 \pm 8)\%$ and a TON_{NiP} of 48 ± 2 , whereas under the same conditions IO-CuCrO₂|**DPP-P/NiP** generated $160 \pm 24 \text{ nmol}_{\text{H}_2} \text{ cm}^{-2}$ with a FE of $(40 \pm 14)\%$ and a TON_{NiP} of 36 ± 5 . The high performance of **PMI-P** reflects the molecular structure, which is well-suited for hole injection and charge separation. The broad and intense absorption profile ensures that a large portion of visible light can be effectively harvested, enhancing the achievable photocurrent.

High amounts of H₂ in these photocathodes demonstrates that co-immobilisation is a viable method to form DSPCs. Alteration of the CuCrO₂ electrode morphology through the development of IO structures was shown to enhance loadings of dye and catalyst, supporting proton reduction at a higher capacity. The novel IO-CuCrO₂ structure presented here provides a basis for development of efficient DSPCs and offers a platform for evaluation of molecular components in such systems.

4.8. Experimental Section

Materials and Methods

NiP,⁹⁷ **DPP-P**,⁸⁰ and **PMI-P**,⁷⁹ were synthesised as previously reported. Milli-Q[®] H₂O (R > 18.2 MΩ cm) was used for all electrochemical and analytical measurements. Cu(NO₃)₂·3H₂O (Sigma-Aldrich, ≥99%), Cr(NO₃)₃·9H₂O (Sigma-Aldrich, ≥99%), and anhydrous NaOH pellets (Sigma-Aldrich, ≥98%) were used for CuCrO₂-NP preparation.²²⁸ PS beads (Polysciences Inc., 750 nm, 2.6% w/v) were used for IO-CuCrO₂ synthesis. ITO-coated glass sheets (Vision Tek Systems Ltd., R = 12 Ω cm⁻², thickness of 1.1 mm) were cut into 1 × 3 cm² slides prior to cleaning.

Synthesis of CuCrO₂-NPs

Cu(NO₃)₂·3H₂O (1.51 g, 6.25 mmol) and Cr(NO₃)₃·6H₂O (2.50 g, 6.25 mmol) were stirred in MilliQ[®] H₂O (70 mL) and NaOH (5.0 g) was added (final solution pH = 13). The solution was stirred at room temperature for 2 h then 12 mL was decanted into a PTFE-lined autoclave (23 mL total volume). The autoclave was heated to 240 °C for 60 h before the CuCrO₂-NPs were removed. The particles were washed with HCl (0.1 M, 15 mL), centrifuged (8000 rpm, 5 min), and the supernatant removed. They were then washed with EtOH (15 mL), re-centrifuged, and the supernatant removed. The washing steps were repeated for a total of 3 washes before the CuCrO₂-NPs were dried *in vacuo*. The dry NPs were ground using a pestle and mortar and stored under vacuum before use.

Synthesis of IO-CuCrO₂ Electrodes

PS beads (750 nm, 2.6% w/v suspension in H₂O, Polysciences Inc., 0.5 mL) were centrifuged and the supernatant removed, then washed with MeOH and centrifuged again to give a PS pellet. A solution of CuCrO₂ (7.5 wt%, MeOH:H₂O = 1:4, 140 μL) was added to the PS pellet and sonicated (5 min at <10 °C). The solution was drop cast (4 μL) on ITO-coated glass (0.5 cm², confined with parafilm) and dried in air for 3 h. The parafilm was removed and the PS template dissolved in toluene for 15 h before being rinsed with acetone then H₂O and dried *in vacuo*. Post annealing under Ar (500 °C, 5 °C min⁻¹ ramp rate, 1 h, 150 SCCM flow rate) using a tube furnace fitted with a quartz tube, end seals, and insulation plugs (Carbolite Gero) was required to sinter the particles to form the final IO-CuCrO₂ structures.

Physical Characterisation

Tescan MIRA3 FEG-SEM. Energy-dispersive X-ray spectra were recorded with an Oxford Instruments Aztec Energy X-maxN 80 EDX system (20 kV, 15 mm working distance). TEM analysis was conducted using a FEI Phillips Technai F20-G2 TEM, operating at an accelerating voltage of 200 kV (Electron Microscopy Suite, Cavendish Laboratory, University of Cambridge). XRD measurements were taken with a PANalytical BV X'Pert Pro X-Ray Diffractometer. UV-Vis absorption spectra were acquired using a Varian Cary 50 spectrophotometer operated in transmission mode or with a diffuse reflectance accessory (Barrelino™) for powder samples. Emission spectra were recorded on a Fluoromax-4 Horiba Jobin Yvon spectrofluorimeter (PMI) or with an Edinburgh Instruments FS5 spectrofluorimeter (DPP). N₂ gas adsorption measurements were carried out using a Micromeritics 3 Flex (Micromeritics, Norcross, GA, USA) with powder samples. Samples were degassed for 10 h at 100 °C, and measurements were carried out in liquid N₂. BET specific surface area values were obtained from fitting N₂ isotherms using the Microactive software.

Molecule Immobilisation

The dye species were immobilised through soaking in a bath containing **DPP-P** (0.2 mM) or **PMI-P** (0.2 mM) for 15 h in DMF. The IO-CuCrO₂|**dye** electrodes were rinsed with DMF and water before being dried under N₂. These electrodes were then soaked in **NiP** (1 mM, MeOH) for 3 h in a N₂ atmosphere. The IO-CuCrO₂|**dye/NiP** electrodes were rinsed with MeOH then water and dried under N₂ in the dark. All electrodes were used directly after immobilisation. A bare IO-CuCrO₂ electrode was soaked in a solution of phenylphosphonic acid (0.5 M, DMF) for 2 h then rinsed with DMF and H₂O for the comparative dark current study.

Quantification of Immobilised DPP-P and NiP

DPP-P and **PMI-P** loadings were quantified using UV-Vis spectroscopy following desorption from IO-CuCrO₂|**dye/NiP** electrodes by scraping powder from the surface (0.25 cm²) and sonicating in tetrabutylammonium hydroxide 30-hydrate (0.1 M, DMF, 1 mL) for 30 min. Longer periods of soaking and higher concentrations of basic solution resulted in decomposition. It should be noted that using phenylphosphonic acid was not possible in this case as this resulted in incomplete desorption from the surface. The absorption maximum at 500 nm or 536 nm for **DPP-P** and **PMI-P** electrodes respectively was determined for 3 electrodes and fitted to a calibration curve to determine the loading values. **NiP** loading was determined by ICP-OES following overnight digestion of electrodes (0.25 cm²) in aqueous

HNO₃ (70%, 1 mL) and subsequent dilution to 10% v/v with MilliQ[®] H₂O. Values for nitric acid solution, IO-CuCrO₂, IO-CuCrO₂|**DPP-P**, IO-CuCrO₂|**PMI-P**, and pre- and post-electrolysis CuCrO₂|**DPP-P/NiP** and CuCrO₂|**PMI-P/NiP** electrodes were determined in triplicate.

IPCE Measurements

A 3-electrode setup with a Pt-counter, Ag/AgCl/KCl_{sat} reference, and an IO-CuCrO₂|**dye/NiP** or IO-CuCrO₂ working electrode was used in a custom 3-necked cell with a flat borosilicate glass window for IPCE measurements. The electrolyte solution was Na₂SO₄ (0.1 M, pH 3) and an applied potential of +0.3 V vs. RHE maintained for all measurements. Monochromatic light was supplied with a 300 W Xenon lamp solar light simulator connected to a monochromator (MSH300, LOT Quantum design). The intensity was calibrated to 0.8 mW cm⁻² for each individual wavelength and experiments with each electrode were conducted in triplicate with different electrodes using an active area of 0.25 cm². Photocurrents were determined at each recorded wavelength through light-chopping using an Ivium CompactStat potentiostat. Error bars represent standard deviation from the mean.

Photoelectrochemical Measurements

PEC measurements were conducted using an Ivium CompactStat potentiostat in a custom two-compartment electrochemical cell featuring a flat quartz window and a Nafion membrane divider. A three-electrode setup was used with a Pt-counter, Ag/AgCl/KCl_{sat} reference, and an IO-CuCrO₂-based working electrode (0.25 cm² active area). N₂-purged (15 min) aqueous Na₂SO₄ electrolyte solution (0.1 M, pH 3) was used for all measurements. Electrodes were illuminated from the front using a calibrated Newport Oriel solar light simulator (150 W, 100 mW cm⁻², AM 1.5G) with an IR water filter and a UQG Optics UV-Filter ($\lambda > 420$ nm).

CPPE experiments were conducted in triplicate at +0.3 V and 0.0 V vs. RHE in a custom two-compartment electrochemical cell featuring a flat quartz window and a Nafion membrane divider. The working compartment volume was 12 mL with a gas headspace of 5 mL and the counter compartment contained 4.5 mL solution and a 3.5 mL headspace. Both compartments were purged with 2% CH₄ in N₂ for 30 min prior to electrolysis and the amount of H₂ determined using a Shimadzu Tracera GC2010 Plus gas chromatograph using a barrier ionisation discharge (BID) detector and a molsieve column (kept at 130°C) with He as the carrier gas. All PEC cells were left for 2 h following electrolysis to allow solution dissolved H₂ to equilibrate with the gas headspace. The partial pressure of H₂ was calculated to account for dissolved gas in the solution and this was added to the amount of H₂ to obtain the Faradaic efficiency.

Chapter 5

Conclusions and Outlook

The aim of this thesis was to demonstrate the ability of delafossite CuCrO_2 to function as a p-type semiconductor (p-SC) in dye-sensitised photocathodes (DSPCs) for solar H_2 generation. The development of a range of photocathodes through incorporation of molecular dyes, quantum dots (QDs), and molecular catalysts, with CuCrO_2 , enabled improvement over previously reported systems. These advances realise dye-sensitised photoelectrochemical (DSPEC) cells as a sustainable route to solar fuel generation.

Prior to this research, NiO was the dominant wide-bandgap p-SC for dye-sensitisation. Despite success in the dye-sensitised solar cell community,^{61,199} application in DSPCs proved relatively ineffective. Problems such as fast recombination between the reduced catalyst with holes in NiO were attributed to material properties.²¹⁷ In arrangements where the catalyst was co-immobilised on NiO with the dye these issues were particularly prominent, which directed research towards dyad complexes¹⁴² and layer-by-layer assemblies.^{121,122} Modest catalytic activity with these complicated assemblies emphasised the need for a more suitable p-SC. In this work, CuCrO_2 was presented as one alternative to overcome some of the limitations of NiO. Two synthetic methods were explored for the synthesis and optimisation of CuCrO_2 electrodes: sol-gel and hydrothermal.

The sol-gel synthesis was the first method explored. Spin-coating a precursor sol on indium tin oxide-coated glass (ITO-glass) and subsequent annealing steps in firstly aerobic, then inert conditions, reproducibly generated mesoporous CuCrO_2 electrodes. Physical characterisation of the films showed that pure phase CuCrO_2 was obtained with the thickness being easily controlled by alteration of the number of layers deposited. Mott-Schottky analysis highlighted the p-type character and showed that the flatband potential of CuCrO_2 is more anodic than NiO, in line with previous reports, enabling an early onset of photocurrent.²²⁸

Immobilisation of an organic diketopyrrolopyrrole dye (**DPP-P**) through anchoring with a phosphonic acid group was successful. High photocurrents were achieved using a sacrificial electron acceptor (SEA) suggesting efficient hole injection from the dye into the valence band (VB) of CuCrO_2 . An analogous **DPP-P**-sensitised NiO electrode showed lower photocurrents suggesting that recombination between the reduced dye species and holes in the p-SC is

slower in CuCrO₂. Immobilisation of a Dubois-type nickel catalyst (**NiP**) alongside **DPP-P** generated enhanced photocurrents over bare CuCrO₂ electrodes and controlled potential photoelectrolysis (CPPE) confirmed that this architecture was capable of generating H₂ with a high turnover number (TON). H₂ production was greater with the CuCrO₂-based photocathode than the NiO system using the same molecular components, which suggests that recombination pathways are suppressed in CuCrO₂. The results demonstrated the advantages of switching to more suitable p-SCs in DSPCs.

Having established sol-gel derived CuCrO₂ films as a good scaffold for dye-sensitisation, the versatility of the p-SC was explored through development of a QD-immobilised photocathode. QDs are considered highly stable, easily synthesised, and extremely efficient light absorbers for photocatalytic H₂ generation.^{179,180} However, the majority of previous reports required carcinogenic Cd components to function, limiting widespread applicability. Recently, ZnSe-nanorods (NRs) for H₂ generation emerged as a good candidate to replace Cd-QDs.¹⁹⁰ ZnSe-NRs were deposited on CuCrO₂ electrodes through drop casting. This *ex situ* deposition method retained the ligand-stripped surface of the ZnSe-NRs, generating photocathodic current under illumination. CPPE confirmed the generation of H₂ without addition of a co-catalyst presenting the first example of a ZnSe-sensitised photocathode. The simple construction and modification of the system presented an alternative approach to H₂ generation, allowing routes to future development to be identified.

Sol-gel synthesised CuCrO₂ films were successful in generating H₂ with dye-catalyst and QD assemblies. The low yields of H₂ in these systems was attributed to the mesoporous structure, which was only capable of loading small amounts of molecular species. A hydrothermal method was explored to increase surface area and therefore molecule loading through formation of porous structures using previously developed CuCrO₂ nanoparticles (NPs).²²⁸ Inverse opal (IO) structures had previously been reported as a simple strategy to form metal oxide nanostructures from NPs,^{305,308} however the construction of IO-CuCrO₂ required alterations to suit the material. A bottom-up template-assisted assembly method was adapted to incorporate CuCrO₂. IO-CuCrO₂ electrodes with high porosity and uniform optimal thickness of 2 μm were obtained.

The reproducible, high surface area IO-CuCrO₂ electrodes made it possible to construct two different organic dye-based photocathodes. The previously established **DPP-P** dye was compared with a recently developed perylene monoimide dye, **PMI-P**. The two different dye structures exhibit favourable properties for sensitisation of p-SCs. Photophysical and electrochemical properties of the dyes in solution showed that both were suitable candidates

for coupling with IO-CuCrO₂. Both dyes possess a LUMO spatially removed from the p-SC, and **PMI-P** has an additional functional feature in the ethynyl spacer that couples the π -system of the PMI core with the anchoring group, facilitating hole injection. The absorption spectra displayed broad and intense profiles for both species in the visible region, however **PMI-P** displayed a higher molar extinction coefficient and a slightly red-shifted absorption, enabling harvesting of a larger portion of the solar spectrum. Immobilisation of **PMI-P** on IO-CuCrO₂ showed inversion of the absorption maxima, representative of agglomeration, which could be a photocurrent-limiting factor. High loadings of dye and catalyst were achieved with the IO-CuCrO₂ films, confirming the advantages of moving to nanostructured surfaces.

Photoelectrochemical (PEC) comparison using a SEA showed highest performance for **PMI-P**-sensitised electrodes over the corresponding **DPP-P**-based electrodes. The higher photocurrents for IO-CuCrO₂|**PMI-P** electrodes were attributed to lower susceptibility for recombination as well as the broad and more intense absorption profile. **NiP** was co-immobilised with each dye to form functional DSPECs for H₂ generation. High photocathodic currents were observed, outperforming the previously reported sol-gel CuCrO₂|**DPP-P/NiP** photocathodes. With the IO structured films, a greater thickness electrode could be used (2 μ m) as direct channels for diffusion of holes were opened up in the less dense surface. The higher surface area was beneficial in supporting a higher loading of dye and catalyst molecules, leading to the generation of appreciable amounts of H₂. Furthermore, IO-CuCrO₂|**PMI-P/NiP** photocathodes produced the most H₂, highlighting the beneficial properties of this dye for p-SC sensitisation. The results highlight that both dye structure and p-SC morphology has a significant impact on DSPEC performance.

In the molecular systems, co-assembly of dye and catalyst components on CuCrO₂ was effective in permitting high catalyst turnovers to generate H₂. This outcome is highly important for future development of DSPECs. The range of simply constructed photocathodes can be expanded, as complex synthesis to form dyad structures had previously limited availability. Successful H₂ generation using ZnSe as the photosensitiser also provides a basis for expansion to non-carcinogenic QDs, where a co-catalyst is not required for catalytic activity. The preparation methods were both capable of supporting catalytic reactions, and the IO-CuCrO₂ electrodes constructed using a hydrothermal method improved performance. The impact of morphology and surface area was emphasised as a key contributing factor for DSPECs.

The variety of dyes suited for sensitisation of p-SCs has grown over the past decade due to a better understanding of the charge transfer kinetics at the p-SC/dye interface.⁶¹ Incorporation

of two different dyes with different structural features suited for anchoring to p-SCs, highlights the importance of dye properties in DSPCs. The need for a spatially removed LUMO and a HOMO capable of rapid hole injection to generate the reduced dye species has been previously demonstrated for DSPCs using transient spectroscopic techniques.¹⁵² Here, the use of a modified PMI dye tailored for hole injection showed improved performance with a SEA and with an immobilised catalyst, supporting the proposed theory.

A major limitation in NiO systems is the recombination of the reduced catalyst with holes in the VB of the p-SC.¹²¹ The significant Faradaic efficiencies (FEs) and high amounts of H₂ generated with the IO-CuCrO₂|**dye/NiP** systems suggest that CuCrO₂ is a more suitable p-SC. The suggested dominant mechanism in NiO is trap-mediated recombination.²¹⁷ A suspected lower density of trap states around the VB for CuCrO₂ is likely responsible for the kinetically limited back reaction. Spectroscopic experiments to associate the observed performance with recombination routes in CuCrO₂ are currently being conducted in collaboration with the Hammarström group, Uppsala University. Insights into the catalysis-limiting processes will enable further improvement of CuCrO₂-based DSPCs.

With respect to alteration of the catalyst, there is a large scope for diversity. The Dubois-type catalyst used here is highly active and stable for H₂ generation.^{97,104} However, further kinetic limitation of recombination between the reduced catalyst and the p-SC could be exemplified using natural enzymes such as hydrogenase (H₂ase). Despite being costly to purify and susceptible to oxygen inhibition, they are good model catalysts, operating with high efficiency at the thermodynamic potential.^{333–335} Furthermore, their integration with IO structures has enhanced performance owing to the orientation dependent charge transfer, which requires the distal Fe-S cluster to be well connected with the electrode.³⁰⁸ H₂ases have been protected from O₂ inhibition with dye species in solution,³³⁶ but they have not yet been incorporated in DSPCs. Developing a functional system would not only extend routes to interfacing biological organisms and inorganic/organic artificial components, but also provide a flexible platform to investigate the mechanistic operation of such species.

Molecular catalysts for CO₂ could also be incorporated with CuCrO₂. Transition metal complexes have exhibited high performance for selective CO₂ reduction, rivalling their precious-metal-based counterparts.⁵⁷ Previous work has incorporated Ru-Re dyad systems in various DSPCs,^{138,139,328,329} but no co-immobilised molecular CO₂ reduction DSPCs currently exist. Tuning surface-bound molecular dyes or QDs for integration with such catalysts could improve selectivity over conventionally employed narrow-bandgap semiconductors and permit precious-metal-free components to be used. Specific control over the reductive driving force

can be achieved through choice of dye or QD to regulate product selectivity in molecular systems. Possible outcomes include direct SynGas formation or selective formate generation with molecular systems.

Finally, development of working tandem systems that are capable of carrying out bias-free redox reactions are of high interest. Although this encompasses water splitting in the short term, recent developments in organic oxidation reactions and photoreforming of biomass and waste have extended the substrate range.^{24,25,295} Transition of dye-sensitised systems from fuel generation to applications in organic photoredox catalysis further enhances the applicability of precisely-tuneable light absorption and directional charge transfer in DSPEC cells.^{337,338}

Chapter 6

References

- 1 D. Wuebbles, D. W. Fahey, K. A. Hibbard, B. DeAngelo, S. Doherty, K. Hayhoe, R. Horton, J. P. Kossin, P. C. Taylor, A. M. Waple and C. P. Weaver, *Climate Science Special Report: Fourth National Climate Assessment*, U.S Global Change Research Program, Washington DC, USA, 2017.
- 2 D. R. Reidmiller, C. W. Avery, D. R. Easterling, K. E. Kunkel, K. L. M. Lewis, T. K. Maycock and B. C. Stewart, *Impacts, Risks, and Adadptation in the United States: Fourth National Climate Assessment, Volume II*, U.S Global Change Research Program, Washington DC, USA, 2018.
- 3 *BP Statistical Review of World Energy, 67th Edition*, 2018.
- 4 C. Kost, S. Shammugam, V. Julch, H.-T. Nguyen and T. Schlegl, *Levelized Cost of Electricity - Renewable Energy Technologies*, Fraunhofer Institute for Solar Energy Systems ISE, 2018.
- 5 M. R. Shaner, S. J. Davis, N. S. Lewis and K. Caldeira, *Energy Environ. Sci.*, 2018, **11**, 914–925.
- 6 J. B. Goodenough, *ACS Catal.*, 2017, **7**, 1132–1135.
- 7 M. Kato, J. Z. Zhang, N. Paul and E. Reisner, *Chem. Soc. Rev.*, 2014, **43**, 6485–6497.
- 8 J. Barber, *Chem. Soc. Rev.*, 2009, **38**, 185–96.
- 9 Y. Tachibana, L. Vayssieres and J. R. Durrant, *Nat. Photonics*, 2012, **6**, 511–518.
- 10 L. Schlapbach and A. Züttel, *Nature*, 2001, **414**, 353–358.
- 11 T. R. Cook, D. K. Dogutan, S. Y. Reece, Y. Surendranath, T. S. Teets and D. G. Nocera, *Chem. Rev.*, 2010, **110**, 6474–6502.
- 12 O. Gröger, H. A. Gasteiger and J.-P. Suchsland, *J. Electrochem. Soc.*, 2015, **162**, A2605–A2622.
- 13 F. Jaouen, D. Jones, N. Coutard, V. Artero, P. Strasser and A. Kucernak, *Johnson Matthey Technol. Rev.*, 2018, **62**, 231–255.
- 14 A. Y. Khodakov, W. Chu and P. Fongarland, *Chem. Rev.*, 2007, **107**, 1692–1744.
- 15 T. da Silva Veras, T. S. Mozer, D. da Costa Rubim Messeder dos Santos and A. da Silva César, *Int. J. Hydrogen Energy*, 2017, **42**, 2018–2033.
- 16 J. W. W. Ager, M. R. R. Shaner, K. A. A. Walczak, I. D. D. Sharp and S. Ardo, *Energy Environ. Sci.*, 2015, **8**, 2811–2824.
- 17 B. A. Pinaud, J. D. Benck, L. C. Seitz, A. J. Forman, Z. Chen, T. G. Deutsch, B. D.

- James, K. N. Baum, G. N. Baum, S. Ardo, H. Wang, E. Miller and T. F. Jaramillo, *Energy Environ. Sci.*, 2013, **6**, 1983–2002.
- 18 J. H. Montoya, L. C. Seitz, P. Chakthranont, A. Vojvodic, T. F. Jaramillo and J. K. Nørskov, *Nat. Mater.*, 2017, **16**, 70–81.
- 19 S. Ardo, D. Fernandez Rivas, M. A. Modestino, V. Schulze Greiving, F. F. Abdi, E. Alarcon Llado, V. Artero, K. Ayers, C. Battaglia, J. P. Becker, D. Bederak, A. Berger, F. Buda, E. Chinello, B. Dam, V. Di Palma, T. Edvinsson, K. Fujii, H. Gardeniers, H. Geerlings, S. M. Hashemi, S. Haussener, F. Houle, J. Huskens, B. D. James, K. Konrad, A. Kudo, P. P. Kunturu, D. Lohse, B. Mei, E. L. Miller, G. F. Moore, J. Muller, K. L. Orchard, T. E. Rosser, F. H. Saadi, J. W. Schüttauf, B. Seger, S. W. Sheehan, W. A. Smith, J. Spurgeon, M. H. Tang, R. Van De Krol, P. C. K. Vesborg and P. Westerik, *Energy Environ. Sci.*, 2018, **11**, 2768–2783.
- 20 S. Chen, T. Takata and K. Domen, *Nat. Rev. Mater.*, 2017, **2**, 17050.
- 21 K. Maeda, *ACS Catal.*, 2013, **3**, 1486–1503.
- 22 H. Kasap, C. A. Caputo, B. C. M. Martindale, R. Godin, V. W. H. Lau, B. V. Lotsch, J. R. Durrant and E. Reisner, *J. Am. Chem. Soc.*, 2016, **138**, 9183–9192.
- 23 H. Kasap, D. S. Achilleos, A. Huang and E. Reisner, *J. Am. Chem. Soc.*, 2018, **140**, 11604–11607.
- 24 T. Uekert, M. F. Kuehnel, D. W. Wakerley and E. Reisner, *Energy Environ. Sci.*, 2018, **11**, 2853–2857.
- 25 M. F. Kuehnel and E. Reisner, *Angew. Chem. Int. Ed.*, 2018, **57**, 3290–3296.
- 26 D. W. Wakerley, M. F. Kuehnel, K. L. Orchard, K. H. Ly, T. E. Rosser and E. Reisner, *Nat. Energy*, 2017, **2**, 17021.
- 27 M. Carmo, D. L. Fritz, J. Mergel and D. Stolten, *Int. J. Hydrogen Energy*, 2013, **38**, 4901–4934.
- 28 M. A. Green, K. Emery, Y. Hishikawa, W. Warta, E. D. Dunlop, D. H. Levi and A. W. Y. Ho-Baillie, *Prog. Photovoltaics Res. Appl.*, 2017, **25**, 3–13.
- 29 J. Jia, L. C. Seitz, J. D. Benck, Y. Huo, Y. Chen, J. W. D. Ng, T. Bilir, J. S. Harris and T. F. Jaramillo, *Nat. Commun.*, 2016, **7**, 13237.
- 30 J.-W. Schüttauf, M. A. Modestino, E. Chinello, D. Lambelet, A. Delfino, D. Dominé, A. Faes, M. Despeisse, J. Bailat, D. Psaltis, C. Moser and C. Ballif, *J. Electrochem. Soc.*, 2016, **163**, F1177–F1181.
- 31 J. Newman, P. G. Hoertz, C. A. Bonino and J. A. Trainham, *J. Electrochem. Soc.*, 2012, **159**, A1722–A1729.
- 32 A. Rothschild and H. Dotan, *ACS Energy Lett.*, 2017, **2**, 45–51.
- 33 G. Segev, J. W. Beeman, J. B. Greenblatt and I. D. Sharp, *Nat. Mater.*, 2018, **17**, 1115–1121.

- 34 M. Paidar, V. Fateev and K. Bouzek, *Electrochim. Acta*, 2016, **209**, 737–756.
- 35 K. Sivula and M. S. Prevot, *J. Phys. Chem. C*, 2013, **117**, 17879–17893.
- 36 S. Hu, C. Xiang, S. Haussener, A. D. Berger and N. S. Lewis, *Energy Environ. Sci.*, 2013, **6**, 2984–2993.
- 37 N. S. Lewis, *Nat. Nanotechnol.*, 2016, **11**, 1010–1019.
- 38 M. G. Walter, E. L. Warren, J. R. McKone, S. W. Boettcher, Q. Mi, E. A. Santori and N. S. Lewis, *Chem. Rev.*, 2010, **110**, 6446–6473.
- 39 R. H. Coridan, A. C. Nielander, S. A. Francis, M. T. McDowell, V. Dix, S. M. Chatman and N. S. Lewis, *Energy Environ. Sci.*, 2015, **8**, 2886–2901.
- 40 B. C. M. Martindale, E. Joliat, C. Bachmann, R. Alberto and E. Reisner, *Angew. Chem. Int. Ed.*, 2016, **55**, 9402–9406.
- 41 M. Guttentag, A. Rodenberg, R. Kopelent, B. Probst, C. Buchwalder, M. Brandstätter, P. Hamm and R. Alberto, *Eur. J. Inorg. Chem.*, 2012, **2012**, 59–64.
- 42 J. Schneider and D. W. Bahnemann, *J. Phys. Chem. Lett.*, 2013, **4**, 3479–3483.
- 43 A. Paracchino, V. Laporte, K. Sivula, M. Grätzel and E. Thimsen, *Nat. Mater.*, 2011, **10**, 456–461.
- 44 V. Andrei, R. L. Z. L. Z. Hoye, M. Crespo-Quesada, M. Bajada, S. Ahmad, M. De Volder, R. Friend and E. Reisner, *Adv. Energy Mater.*, 2018, **8**, 1801403.
- 45 L. A. King, T. R. Hellstern, J. Park, R. Sinclair and T. F. Jaramillo, *ACS Appl. Mater. Interfaces*, 2017, **9**, 36792–36798.
- 46 J. Azevedo, S. D. Tilley, M. Schreier, M. Stefik, C. Sousa, J. P. Araújo, A. Mendes, M. Grätzel and M. T. Mayer, *Nano Energy*, 2016, **24**, 10–16.
- 47 J. J. Leung, J. Warnan, D. H. Nam, J. Z. Zhang, J. Willkomm and E. Reisner, *Chem. Sci.*, 2017, **8**, 5172–5180.
- 48 P. Xu, N. S. McCool and T. E. Mallouk, *Nano Today*, 2017, **14**, 42–58.
- 49 E. A. Gibson, *Chem. Soc. Rev.*, 2017, **46**, 6194–6209.
- 50 M. K. Brennaman, R. J. Dillon, L. Alibabaei, M. K. Gish, C. J. Dares, D. L. Ashford, R. L. House, G. J. Meyer, J. M. Papanikolas and T. J. Meyer, *J. Am. Chem. Soc.*, 2016, **138**, 13085–13102.
- 51 B. O'Regan and M. Grätzel, *Nature*, 1991, **353**, 737–740.
- 52 A. Hagfeldt, G. Boschloo, L. Sun, L. Kloo and H. Pettersson, *Chem. Rev.*, 2010, **110**, 6595–6663.
- 53 Z. Yu, F. Li and L. Sun, *Energy Environ. Sci.*, 2015, **8**, 760–775.
- 54 R. M. Bullock, A. K. Das and A. M. Appel, *Chem. Eur. J.*, 2017, **23**, 7626–7641.
- 55 N. Coutard, N. Kaeffer and V. Artero, *Chem. Commun.*, 2016, **52**, 13728–13748.
- 56 K. L. Materna, R. H. Crabtree and G. W. Brudvig, *Chem. Soc. Rev.*, 2017, **46**, 6099–6110.

- 57 K. E. Dalle, J. Warnan, J. J. Leung, B. Reuillard, I. S. Karmel and E. Reisner, *Chem. Rev.*, 2019, **119**, 2752–2875.
- 58 S. A. Haque, S. Handa, K. Peter, E. Palomares, M. Thelakkat and J. R. Durrant, *Angew. Chem. Int. Ed.*, 2005, **44**, 5740–5744.
- 59 K. Hu, A. D. Blair, E. J. Piechota, P. A. Schauer, R. N. Sampaio, F. G. L. Parlane, G. J. Meyer and C. P. Berlinguette, *Nat. Chem.*, 2016, **8**, 853–859.
- 60 A. Nattestad, A. J. Mozer, M. K. R. Fischer, Y. B. Cheng, A. Mishra, P. Bäuerle and U. Bach, *Nat. Mater.*, 2010, **9**, 31–35.
- 61 V. Nikolaou, A. Charisiadis, G. Charalambidis, A. G. G. Coutsolelos and F. Odobel, *J. Mater. Chem. A*, 2017, **5**, 21077–21113.
- 62 J. T. Kirner and R. G. Finke, *J. Mater. Chem. A*, 2017, **5**, 19560–19592.
- 63 S. Berardi, S. Drouet, L. Francàs, C. Gimbert-Suriñach, M. Guttentag, C. Richmond, T. Stoll and A. Llobet, *Chem. Soc. Rev.*, 2014, **43**, 7501–7519.
- 64 D. Gust, T. A. Moore and A. L. Moore, *Acc. Chem. Res.*, 2009, **42**, 1890–1898.
- 65 A. Bachmeier, S. Hall, S. W. Ragsdale and F. A. Armstrong, *J. Am. Chem. Soc.*, 2014, **136**, 13518–13521.
- 66 J. Greeley, *Annu. Rev. Chem. Biomol. Eng.*, 2016, **7**, 605–635.
- 67 I. Roger, M. A. Shipman and M. D. Symes, *Nat. Rev. Chem.*, 2017, **1**, 0003.
- 68 J. Greeley, T. F. Jaramillo, J. Bonde, I. Chorkendorff and J. K. Nørskov, *Nat. Mater.*, 2006, **5**, 909–913.
- 69 A. J. Medford, A. Vojvodic, J. S. Hummelshøj, J. Voss, F. Abild-Pedersen, F. Studt, T. Bligaard, A. Nilsson and J. K. Nørskov, *J. Catal.*, 2015, **328**, 36–42.
- 70 J. K. Nørskov, F. Abild-Pedersen, F. Studt and T. Bligaard, *Proc. Natl. Acad. Sci.*, 2011, **108**, 937–943.
- 71 J. K. Nørskov, T. Bligaard, J. Rossmeisl and C. H. Christensen, *Nat. Chem.*, 2009, **1**, 37–46.
- 72 J. R. McKone, B. F. Sadler, C. A. Werlang, N. S. Lewis and H. B. Gray, *ACS Catal.*, 2013, **3**, 166–169.
- 73 C. Fan, P. D., L., S. A. and P. P., *J. Electrochem. Soc.*, 1994, **141**, 382.
- 74 C. C. L. McCrory, S. Jung, I. M. Ferrer, S. M. Chatman, J. C. Peters and T. F. Jaramillo, *J. Am. Chem. Soc.*, 2015, **137**, 4347–4357.
- 75 J. Kibsgaard, Z. Chen, B. N. Reinecke and T. F. Jaramillo, *Nat. Mater.*, 2012, **11**, 963–969.
- 76 J. D. Benck, T. R. Hellstern, J. Kibsgaard, P. Chakthranont and T. F. Jaramillo, *ACS Catal.*, 2014, **4**, 3957–3971.
- 77 T. F. Jaramillo, K. P. Jørgensen, J. Bonde, J. H. Nielsen, S. Horch and I. Chorkendorff, *Science*, 2007, **317**, 100–102.

- 78 X. Wang, K. Maeda, A. Thomas, K. Takanebe, G. Xin, J. M. Carlsson, K. Domen and M. Antonietti, *Nat. Mater.*, 2009, **8**, 76–80.
- 79 J. Warnan, J. Willkomm, Y. Farre, Y. Pellegrin, M. Boujtita, F. Odobel and E. Reisner, *Chem. Sci.*, 2019, **10**, 2758–2766.
- 80 J. Warnan, J. Willkomm, J. N. Ng, R. Godin, S. Prantl, J. R. Durrant and E. Reisner, *Chem. Sci.*, 2017, **8**, 3070–3079.
- 81 K. L. Orchard, D. Hojo, K. P. Sokol, M.-J. Chan, N. Asao, T. Adschiri and E. Reisner, *Chem. Commun.*, 2017, **53**, 12638–12641.
- 82 H. Yan, J. Yang, G. Ma, G. Wu, X. Zong, Z. Lei, J. Shi and C. Li, *J. Catal.*, 2009, **266**, 165–168.
- 83 A. Indra, P. W. Menezes, K. Kailasam, D. Hollmann, M. Schröder, A. Thomas, A. Brückner and M. Driess, *Chem. Commun.*, 2016, **52**, 104–107.
- 84 T. Simon, N. Bouchonville, M. J. Berr, A. Vaneski, A. Adrovic, D. Volbers, R. Wyrwich, M. Döblinger, A. S. Susha, A. L. Rogach, F. Jäckel, J. K. Stolarczyk and J. Feldmann, *Nat. Mater.*, 2014, **13**, 1–6.
- 85 S. Cobo, J. Heidkamp, P.-A. Jacques, J. Fize, V. Fourmond, L. Guetaz, B. Joussetme, V. Ivanova, H. Dau, S. Palacin, M. Fontecave and V. Artero, *Nat. Mater.*, 2012, **11**, 802–807.
- 86 J. Dong, M. Wang, X. Li, L. Chen, Y. He and L. Sun, *ChemSusChem*, 2012, **5**, 2133–2138.
- 87 Z. Han, F. Qiu, R. Eisenberg, P. L. Holland and T. D. Krauss, *Science*, 2012, **338**, 1321–1324.
- 88 G. Sahara and O. Ishitani, *Inorg. Chem.*, 2015, **54**, 5096–5104.
- 89 M. P. Stewart, M. H. Ho, S. Wiese, M. Lou Lindstrom, C. E. Thogerson, S. Raugei, R. M. Bullock and M. L. Helm, *J. Am. Chem. Soc.*, 2013, **135**, 6033–6046.
- 90 D. Il Won, J. S. Lee, J. M. Ji, W. J. Jung, H. J. Son, C. Pac and S. O. Kang, *J. Am. Chem. Soc.*, 2015, **137**, 13679–13690.
- 91 B. Reuillard, K. H. Ly, T. E. Rosser, M. F. Kuehnel, I. Zebger and E. Reisner, *J. Am. Chem. Soc.*, 2017, **139**, 14425–14435.
- 92 M. F. Kuehnel, K. L. Orchard, K. E. Dalle and E. Reisner, *J. Am. Chem. Soc.*, 2017, **139**, 7217–7223.
- 93 J. Willkomm, N. M. Muresan and E. Reisner, *Chem. Sci.*, 2015, **6**, 2727–2736.
- 94 S. Roy, B. Sharma, J. Pécaut, P. Simon, M. Fontecave, P. D. Tran, E. Derat and V. Artero, *J. Am. Chem. Soc.*, 2017, **139**, 3685–3696.
- 95 T. Liu, M. Guo, A. Orthaber, R. Lomoth, M. Lundberg, S. Ott and L. Hammarström, *Nat. Chem.*, 2018, **10**, 881–887.
- 96 A. Dutta, D. L. DuBois, J. A. S. Roberts and W. J. Shaw, *Proc. Natl. Acad. Sci.*, 2014,

- 111**, 16286–16291.
- 97 M. A. Gross, A. Reynal, J. R. Durrant and E. Reisner, *J. Am. Chem. Soc.*, 2014, **136**, 356–366.
- 98 N. Kaeffer, C. D. Windle, R. Brisse, C. Gablin, D. Leonard, B. Joussetme, M. Chavarot-Kerlidou and V. Artero, *Chem. Sci.*, 2018, **9**, 6721–6738.
- 99 S. Bold, L. Zedler, Y. Zhang, J. Massin, V. Artero, M. Chavarot-Kerlidou and B. Dietzek, *Chem. Commun.*, 2018, **54**, 10594–10597.
- 100 T. E. Rosser and E. Reisner, *ACS Catal.*, 2017, **7**, 3131–3141.
- 101 M. L. Clark, P. L. Cheung, M. Lessio, E. A. Carter and C. P. Kubiak, *ACS Catal.*, 2018, **8**, 2021–2029.
- 102 K. J. Lee, N. Elgrishi, B. Kandemir and J. L. Dempsey, *Nat. Rev. Chem.*, 2017, **1**, 0039.
- 103 A. D. Wilson, R. H. Newell, M. J. McNevin, J. T. Muckerman, M. R. DuBois and D. L. DuBois, *J. Am. Chem. Soc.*, 2006, **128**, 358–366.
- 104 M. L. Helm, M. P. Stewart, R. M. Bullock, M. R. DuBois and D. L. DuBois, *Science*, 2011, **333**, 863–866.
- 105 R. M. Bullock, A. M. Appel and M. L. Helm, *Chem. Commun.*, 2014, **50**, 3125–3143.
- 106 D. L. Dubois, *Inorg. Chem.*, 2014, **53**, 3935–3960.
- 107 F. A. Armstrong and J. Hirst, *Proc. Natl. Acad. Sci.*, 2011, **108**, 14049–14054.
- 108 J. W. Wang, W. J. Liu, D. C. Zhong and T. B. Lu, *Coord. Chem. Rev.*, 2019, **378**, 237–261.
- 109 U. J. Kilgore, J. A. S. Roberts, D. H. Pool, A. M. Appel, M. P. Stewart, M. R. DuBois, W. G. Dougherty, W. S. Kassel, R. M. Bullock and D. L. DuBois, *J. Am. Chem. Soc.*, 2011, **133**, 5861–5872.
- 110 E. S. Rountree and J. L. Dempsey, *J. Am. Chem. Soc.*, 2015, **137**, 13371–13380.
- 111 S. Wiese, U. J. Kilgore, M. H. Ho, S. Raugei, D. L. Dubois, R. M. Bullock and M. L. Helm, *ACS Catal.*, 2013, **3**, 2527–2535.
- 112 S. Chen, M.-H. H. Ho, R. M. Bullock, D. L. DuBois, M. Dupuis, R. Rousseau and S. Raugei, *ACS Catal.*, 2014, **4**, 229–242.
- 113 M. Ohagan, M. H. Ho, J. Y. Yang, A. M. Appel, M. R. Dubois, S. Raugei, W. J. Shaw, D. L. Dubois and R. M. Bullock, *J. Am. Chem. Soc.*, 2012, **134**, 19409–19424.
- 114 T. J. Meyer, *J. Am. Chem. Soc.*, 1989, **22**, 163–170.
- 115 K. Kalyanasundaram, *Coord. Chem. Rev.*, 1982, **46**, 159–244.
- 116 B. Durham, J. V. Caspar, J. K. Nagle and T. J. Meyer, *J. Am. Chem. Soc.*, 1982, **104**, 4803–4810.
- 117 J. V. Caspar and T. J. Meyer, *J. Am. Chem. Soc.*, 1983, **105**, 5583–5590.
- 118 J. Willkomm, K. L. Orchard, A. Reynal, E. Pastor, J. R. Durrant and E. Reisner, *Chem.*

- Soc. Rev.*, 2015, **45**, 9–23.
- 119 X. Zhang, T. Peng and S. Song, *J. Mater. Chem. A*, 2016, **4**, 2365–2402.
- 120 M. Wang, Y. Yang, J. Shen, J. Jiang and L. Sun, *Sustain. Energy Fuels*, 2017, **1**, 1641–1663.
- 121 M. A. Gross, C. E. Creissen, K. L. Orchard and E. Reisner, *Chem. Sci.*, 2016, **7**, 242–247.
- 122 B. Shan, A. Das, S. L. Marquard, B. H. Farnum, D. Wang, R. M. M. Bullock and T. J. Meyer, *Energy Environ. Sci.*, 2016, **9**, 3693–3697.
- 123 Y. Han, R. J. Dillon, C. J. Flynn, E. S. Rountree, L. Alibabaei, J. F. Cahoon, J. M. Papanikolas and J. L. Dempsey, *Can. J. Chem.*, 2017, **10**, 1–10.
- 124 L. Zhang, L. Favereau, Y. Farré, E. Mijangos, Y. Pellegrin, E. Blart, F. Odobel and L. Hammarström, *Phys. Chem. Chem. Phys.*, 2016, **18**, 18515–18527.
- 125 A. Sinopoli, C. J. Wood, E. A. Gibson and P. I. P. Elliott, *Dye. Pigment.*, 2017, **140**, 269–277.
- 126 M. Gennari, F. Légalité, L. Zhang, Y. Pellegrin, E. Blart, J. Fortage, A. M. Brown, A. Deronzier, M. N. Collomb, M. Boujtita, D. Jacquemin, L. Hammarström and F. Odobel, *J. Phys. Chem. Lett.*, 2014, **5**, 2254–2258.
- 127 A. Sinopoli, C. J. Wood, E. A. Gibson and P. I. P. Elliott, *Eur. J. Inorg. Chem.*, 2016, **2016**, 2887–2890.
- 128 C. E. Castillo, M. Gennari, T. Stoll, J. Fortage, A. Deronzier, M. N. Collomb, M. Sandroni, F. Légalité, E. Blart, Y. Pellegrin, C. Delacote, M. Boujtita, F. Odobel, P. Rannou and S. Sadki, *J. Phys. Chem. C*, 2015, **119**, 5806–5818.
- 129 R. J. Dillon, L. Alibabaei, T. J. Meyer and J. M. Papanikolas, *ACS Appl. Mater. Interfaces*, 2017, **9**, 26786–26796.
- 130 N. Queyriaux, R. A. Wahyuno, J. Fize, C. Gablin, M. Wächtler, E. Martinez, D. Léonard, B. Dietzek, V. Artero and M. Chavarot-Kerlidou, *J. Phys. Chem. C*, 2017, **121**, 5891–5904.
- 131 N. Pöldme, L. O'Reilly, I. Fletcher, J. Portoles, I. V. Sazanovich, M. Towrie, C. Long, J. G. Vos, M. T. Pryce and E. A. Gibson, *Chem. Sci.*, 2019, **10**, 99–112.
- 132 N. Marinakis, C. Wobill, E. C. Constable and C. E. Housecroft, *Polyhedron*, 2018, **140**, 122–128.
- 133 Y. Pellegrin, L. Le Pleux, E. Blart, A. Renaud, B. Chavillon, N. Szuwarski, M. Boujtita, L. Cario, S. Jobic, D. Jacquemin and F. Odobel, *J. Photochem. Photobiol. A Chem.*, 2011, **219**, 235–242.
- 134 J. C. Freys, J. M. Gardner, L. D'Amario, A. M. Brown and L. Hammarström, *Dalt. Trans.*, 2012, **41**, 13105–13111.
- 135 Z. Ji and Y. Wu, *J. Phys. Chem. C*, 2013, **117**, 18315–18324.

- 136 C. J. Wood, K. C. D. Robson, P. I. P. Elliott, C. P. Berlinguette and E. A. Gibson, *RSC Adv.*, 2014, **4**, 5782–5791.
- 137 B. Shan, B. D. Sherman, C. M. Klug, A. Nayak, S. L. Marquard, Q. Liu, R. M. Bullock and T. J. Meyer, *J. Phys. Chem. Lett.*, 2017, **8**, 4374–4379.
- 138 G. Sahara, H. Kumagai, K. Maeda, N. Kaeffer, V. Artero, M. Higashi, R. Abe and O. Ishitani, *J. Am. Chem. Soc.*, 2016, **138**, 14152–14158.
- 139 H. Kumagai, G. Sahara, K. Maeda, M. Higashi, R. Abe and O. Ishitani, *Chem. Sci.*, 2017, **8**, 4242–4249.
- 140 Y. Ooyama and Y. Harima, *ChemPhysChem*, 2012, **13**, 4032–4080.
- 141 J. R. Swierk, D. D. Méndez-Hernández, N. S. McCool, P. Liddell, Y. Terazono, I. Pahk, J. J. Tomlin, N. V. Oster, T. A. Moore, A. L. Moore, D. Gust and T. E. Mallouk, *Proc. Natl. Acad. Sci.*, 2015, **112**, 1681–1686.
- 142 N. Kaeffer, J. Massin, C. Lebrun, O. Renault, M. Chavarot-Kerlidou and V. Artero, *J. Am. Chem. Soc.*, 2016, **138**, 12308–12311.
- 143 Y. Klein, N. Marinakis, E. Constable, C. Housecroft, Y. M. Klein, N. Marinakis, E. C. Constable and C. E. Housecroft, *Crystals*, 2018, **8**, 389.
- 144 F. Li, K. Fan, B. Xu, E. Gabrielsson, Q. Daniel, L. Li and L. Sun, *J. Am. Chem. Soc.*, 2015, **137**, 9153–9159.
- 145 C. J. Wood, G. H. Summers, C. A. Clark, N. Kaeffer, M. Braeutigam, L. R. Carbone, L. D’Amario, K. Fan, Y. Farré, S. Narbey, F. Oswald, L. A. Stevens, C. D. J. Parmenter, M. W. Fay, A. La Torre, C. E. Snape, B. Dietzek, D. Dini, L. Hammarström, Y. Pellegrin, F. Odobel, L. Sun, V. Artero and E. A. Gibson, *Phys. Chem. Chem. Phys.*, 2016, **18**, 10727–10738.
- 146 D. A. Hoogeveen, M. Fournier, S. A. Bonke, X. Y. Fang, A. J. Mozer, A. Mishra, P. Bäuerle, A. N. Simonov and L. Spiccia, *Electrochim. Acta*, 2016, **219**, 773–780.
- 147 D. A. Hoogeveen, M. Fournier, S. A. Bonke, A. Nattestad, A. Mishra, P. Bäuerle, L. Spiccia, A. J. Mozer and A. N. Simonov, *J. Phys. Chem. C*, 2017, **121**, 25836–25846.
- 148 R. J. Kamire, M. B. Majewski, W. L. Hoffeditz, B. T. Phelan, O. K. Farha, J. T. Hupp and M. R. Wasielewski, *Chem. Sci.*, 2017, **22**, 32–57.
- 149 L. Tong, A. Iwase, A. Nattestad, U. Bach, M. Weidener, G. Götz, A. Mishra, P. Bäuerle, R. Amal, G. G. Wallace and A. J. Mozer, *Energy Environ. Sci.*, 2012, **5**, 9472–9475.
- 150 B. Shan, A. Nayak, M. K. Brennaman, M. Liu, S. L. Marquard, M. S. Eberhart and T. J. Meyer, *J. Am. Chem. Soc.*, 2018, **140**, 6493–6500.
- 151 L. J. Antila, P. Ghamgosar, S. Maji, H. Tian, S. Ott and L. Hammarström, *ACS Energy Lett.*, 2016, **1**, 1106–1111.
- 152 M. Gilbert Gatty, S. Pullen, E. Sheibani, H. Tian, S. Ott and L. Hammarström, *Chem.*

- Sci.*, 2018, **9**, 4983–4991.
- 153 J. M. Gardner, M. Beyler, M. Karnahl, S. Tschierlei, S. Ott and L. Hammarström, *J. Am. Chem. Soc.*, 2012, **134**, 19322–19325.
- 154 L. Favereau, J. Warnan, Y. Pellegrin, E. Blart, M. Boujtita, D. Jacquemin and F. Odobel, *Chem. Commun.*, 2013, **49**, 8018–8020.
- 155 D. G. Farnum, G. Mehta, G. G. I. Moore and F. P. Siegal, *Tetrahedron Lett.*, 1974, **15**, 2549–2552.
- 156 Z. Hao and A. Iqbal, *Chem. Soc. Rev.*, 1997, **26**, 203–213.
- 157 W. Li, K. H. Hendriks, M. M. Wienk and R. A. J. Janssen, *Acc. Chem. Res.*, 2016, **49**, 78–85.
- 158 Y. Li, P. Sonar, L. Murphy and W. Hong, *Energy Environ. Sci.*, 2013, **6**, 1684–1710.
- 159 Y. Wu and W. Zhu, *Chem. Soc. Rev.*, 2013, **42**, 2039–2058.
- 160 H. Bronstein, Z. Chen, R. S. Ashraf, W. Zhang, J. Du, J. R. Durrant, P. Shakya Tuladhar, K. Song, S. E. Watkins, Y. Geerts, M. M. Wienk, R. A. J. Janssen, T. Anthopoulos, H. Sirringhaus, M. Heeney and I. McCulloch, *J. Am. Chem. Soc.*, 2011, **133**, 3272–3275.
- 161 J. C. Bijleveld, A. P. Zoombelt, S. G. J. Mathijssen, M. M. Wienk, M. Turbiez, D. M. De Leeuw and R. A. J. Janssen, *J. Am. Chem. Soc.*, 2009, **131**, 16616–16617.
- 162 Y. Farré, L. Zhang, Y. Pellegrin, A. Planchat, E. Blart, M. Boujtita, L. Hammarström, D. Jacquemin and F. Odobel, *J. Phys. Chem. C*, 2016, **120**, 7923–7940.
- 163 T. T. T. Pham, S. K. Saha, D. Provost, Y. Farré, M. Raissi, Y. Pellegrin, E. Blart, S. Vedraïne, B. Ratier, D. Aldakov, F. Odobel and J. Bouclé, *J. Phys. Chem. C*, 2017, **121**, 129–139.
- 164 Y. Farré, M. Raissi, A. Fihey, Y. Pellegrin, E. Blart, D. Jacquemin and F. Odobel, *ChemSusChem*, 2017, **10**, 2618–2625.
- 165 K. Yun, S. Zhang, F. Yu, H. Ye and J. Hua, *J. Energy Chem.*, 2018, **27**, 728–735.
- 166 K. A. Click, D. R. Beauchamp, Z. Huang, W. Chen and Y. Wu, *J. Am. Chem. Soc.*, 2016, **138**, 1174–1179.
- 167 D. V. Talapin, J. S. Lee, M. V. Kovalenko and E. V. Shevchenko, *Chem. Rev.*, 2010, **110**, 389–458.
- 168 H. Zhu, Y. Yang, K. Wu and T. Lian, *Annu. Rev. Phys. Chem.*, 2016, **67**, 259–281.
- 169 C. R. Kagan, E. Lifshitz, E. H. Sargent and D. V. Talapin, *Science*, 2016, **353**, 885–894.
- 170 G. H. Carey, A. L. Abdelhady, Z. Ning, S. M. Thon, O. M. Bakr and E. H. Sargent, *Chem. Rev.*, 2015, **115**, 12732–12763.
- 171 A. P. Alivisatos, *J. Phys. Chem.*, 1996, **100**, 13226–13239.
- 172 E. A. Weiss, *ACS Energy Lett.*, 2017, **2**, 1005–1013.

- 173 C. M. Chang, K. L. Orchard, B. C. M. Martindale and E. Reisner, *J. Mater. Chem. A*, 2016, **4**, 2856–2862.
- 174 M. F. Kuehnel, C. D. Sahm, G. Neri, J. R. Lee, K. L. Orchard, A. J. Cowan and E. Reisner, *Chem. Sci.*, 2018, **9**, 2501–2509.
- 175 M. S. Kodaimati, K. P. McClelland, C. He, S. Lian, Y. Jiang, Z. Zhang and E. A. Weiss, *Inorg. Chem.*, 2018, **57**, 3659–3670.
- 176 F. E. Osterloh, *Chem. Soc. Rev.*, 2013, **42**, 2294–2320.
- 177 P. V. Kamat, *Acc. Chem. Res.*, 2017, **50**, 527–531.
- 178 H. L. Wu, X. B. Li, C. H. Tung and L. Z. Wu, *Adv. Sci.*, 2018, **5**, 1700684.
- 179 X.-B. Li, C.-H. Tung and L.-Z. Wu, *Nat. Rev. Chem.*, 2018, **2**, 160–173.
- 180 Y. J. Yuan, D. Chen, Z. T. Yu and Z. G. Zou, *J. Mater. Chem. A*, 2018, **6**, 11606–11630.
- 181 V. S. Vyas, V. W. H. Lau and B. V. Lotsch, *Chem. Mater.*, 2016, **28**, 5191–5204.
- 182 L. Wang, Y. Zhang, L. Chen, H. Xu and Y. Xiong, *Adv. Mater.*, 2018, **30**, 1801955.
- 183 C. Cometto, R. Kuriki, L. Chen, K. Maeda, T.-C. Lau, O. Ishitani and M. Robert, *J. Am. Chem. Soc.*, 2018, **140**, 7437–7440.
- 184 B. C. M. Martindale, G. A. M. Hutton, C. A. Caputo, S. Prantl, R. Godin, J. R. Durrant and E. Reisner, *Angew. Chemie Int. Ed.*, 2017, **56**, 6459–6463.
- 185 G. A. M. Hutton, B. Reuillard, B. C. M. Martindale, C. A. Caputo, C. W. J. Lockwood, J. N. Butt and E. Reisner, *J. Am. Chem. Soc.*, 2016, **138**, 16722–16730.
- 186 B. C. M. Martindale, G. A. M. Hutton, C. A. Caputo and E. Reisner, *J. Am. Chem. Soc.*, 2015, **137**, 6018–6025.
- 187 A. F. Shaikh, S. S. Arbuj, M. S. Tamboli, S. D. Naik, S. B. Rane and B. B. Kale, *ChemistrySelect*, 2017, **2**, 9174–9180.
- 188 B. Qiu, Q. Zhu, M. Xing and J. Zhang, *Chem. Commun.*, 2017, **53**, 897–900.
- 189 Y. J. Gao, Y. Yang, X. B. Li, H. L. Wu, S. L. Meng, Y. Wang, Q. Guo, M. Y. Huang, C. H. Tung and L. Z. Wu, *Chem. Commun.*, 2018, **54**, 4858–4861.
- 190 M. F. Kuehnel, C. E. Creissen, C. D. Sahm, D. Wielend, A. Schlosser, K. L. Orchard and E. Reisner, *Angew. Chem. Int. Ed.*, 2019, **58**, 5059–5063.
- 191 N. W. Ashcroft and D. N. Mermin, *Solid State Physics*, Brooks/Cole, Delhi, 16th edn., 1976.
- 192 S. H. Simon, *The Oxford Solid State Basics*, Oxford University Press, Oxford, 1st edn., 2013.
- 193 R. Memming, *Semiconductor Electrochemistry*, Wiley-VCH, Weinheim, 2nd edn., 2015.
- 194 R. van de Krol, in *Photoelectrochemical Hydrogen Production*, ed. M. Gratzel, Springer, London, 1st edn., 2016, pp. 13–67.

- 195 H. Gerischer, *Surf. Sci.*, 1969, **18**, 97–122.
- 196 D. F. Watson and G. J. Meyer, *Annu. Rev. Phys. Chem.*, 2004, **56**, 119–156.
- 197 S. Ardo and G. J. Meyer, *Chem. Soc. Rev.*, 2009, **38**, 115–164.
- 198 C. D. Windle, J. Massin, M. Chavarot-Kerlidou and V. Artero, *Dalt. Trans.*, 2018, **47**, 10509–10516.
- 199 J. He, H. Lindström, A. Hagfeldt and S.-E. Lindquist, *J. Phys. Chem. B*, 1999, **103**, 8940–8943.
- 200 L. Li, L. Duan, F. Wen, C. Li, M. Wang, A. Hagfeldt and L. Sun, *Chem. Commun.*, 2012, **48**, 988–990.
- 201 K. Fan, F. S. Li, L. Wang, Q. Daniel, E. Gabrielsson and L. C. Sun, *Phys. Chem. Chem. Phys.*, 2014, **16**, 25234–25240.
- 202 P. B. Pati, L. Zhang, B. Philippe, R. Fernández-Terán, S. Ahmadi, L. Tian, H. Rensmo, L. Hammarström and H. Tian, *ChemSusChem*, 2017, **10**, 2480–2495.
- 203 Z. Ji, M. He, Z. Huang, U. Ozkan and Y. Wu, *J. Am. Chem. Soc.*, 2013, **135**, 11696–11699.
- 204 P.-A. Jacques, V. Artero, J. Pecaut and M. Fontecave, *Proc. Natl. Acad. Sci.*, 2009, **106**, 20627–20632.
- 205 J. M. Gardner, M. Beyler, M. Karnahl, S. Tschierlei, S. Ott and L. Hammarström, *J. Am. Chem. Soc.*, 2012, **134**, 19322–19325.
- 206 A. M. Brown, L. J. Antila, M. Mirmohades, S. Pullen, S. Ott and L. Hammarström, *J. Am. Chem. Soc.*, 2016, **138**, 8060–8063.
- 207 B. Van Den Bosch, J. A. Rombouts, R. V. A. Orru, J. N. H. Reek and R. J. Detz, *ChemCatChem*, 2016, **8**, 1392–1398.
- 208 B. H. Farnum, K.-R. Wee and T. J. Meyer, *Nat. Chem.*, 2016, **8**, 845–852.
- 209 B. Shan, B. H. Farnum, K.-R. Wee and T. J. Meyer, *J. Phys. Chem. C*, 2017, **121**, 5882–5890.
- 210 M. Wen, H.-L. Wu, J.-X. Jian, X.-Z. Wang, X.-B. Li, B. Chen, C.-H. Tung and L.-Z. Wu, *ChemPhotoChem*, 2017, **1**, 260–264.
- 211 P. Meng, M. Wang, Y. Yang, S. Zhang and L. Sun, *J. Mater. Chem. A*, 2015, **3**, 18852–18859.
- 212 M. Abdellah, S. Zhang, M. Wang and L. Hammarström, *ACS Energy Lett.*, 2017, **2**, 2576–2580.
- 213 B. Liu, X.-B. B. Li, Y.-J. J. Gao, Z.-J. J. Li, Q.-Y. Y. Meng, C.-H. H. Tung and L.-Z. Z. Wu, *Energy Environ. Sci.*, 2015, **8**, 1443–1449.
- 214 X. B. Li, B. Liu, M. Wen, Y. J. Gao, H. L. Wu, M. Y. Huang, Z. J. Li, B. Chen, C. H. Tung and L. Z. Wu, *Adv. Sci.*, 2015, **3**, 1500282.
- 215 C. J. Flynn, S. M. McCullough, E. Oh, L. Li, C. C. Mercado, B. H. Farnum, W. Li, C. L.

- Donley, W. You, A. J. Nozik, J. R. McBride, T. J. Meyer, Y. Kanai and J. F. Cahoon, *ACS Appl. Mater. Interfaces*, 2016, **8**, 4754–4761.
- 216 L. D'Amario, R. Jiang, U. B. Cappel, E. A. Gibson, G. Boschloo, H. Rensmo, L. Sun, L. Hammarström and H. Tian, *ACS Appl. Mater. Interfaces*, 2017, **9**, 33470–33477.
- 217 L. D'Amario, J. Föhlinger, G. Boschloo and L. Hammarström, *Chem. Sci.*, 2017, **9**, 223–230.
- 218 A. Wuttig, J. W. Krizan, J. Gu, J. J. Frick, R. J. Cava and A. B. Bocarsly, *J. Mater. Chem. A*, 2017, **5**, 165–171.
- 219 M. S. Prévot, N. Guijarro and K. Sivula, *ChemSusChem*, 2015, **8**, 1359–1367.
- 220 M. S. Prévot, Y. Li, N. Guijarro and K. Sivula, *J. Mater. Chem. A*, 2016, **4**, 3018–3026.
- 221 C. G. Read, Y. Park and K. S. Choi, *J. Phys. Chem. Lett.*, 2012, **3**, 1872–1876.
- 222 J. Gu, Y. Yan, J. W. Krizan, Q. D. Gibson, Z. M. Detweiler, R. J. Cava and A. B. Bocarsly, *J. Am. Chem. Soc.*, 2014, **136**, 830–833.
- 223 A. Renaud, B. Chavillon, L. Le Pleux, Y. Pellegrin, E. Blart, M. Boujtita, T. Pauporté, L. Cario, S. Jobic and F. Odobel, *J. Mater. Chem.*, 2012, **22**, 14353–14356.
- 224 Z. Xu, D. Xiong, H. Wang, W. Zhang, X. Zeng, L. Ming, W. Chen, X. Xu, J. Cui, M. Wang, S. Powar, U. Bach and Y. B. Cheng, *J. Mater. Chem. A*, 2014, **2**, 2968–2976.
- 225 L. Favereau, Y. Pellegrin, L. Hirsch, A. Renaud, A. Planchat, E. Blart, G. Louarn, L. Cario, S. Jobic, M. Boujtita and F. Odobel, *Adv. Energy Mater.*, 2017, **7**, 1601776.
- 226 S. Powar, D. Xiong, T. Daeneke, M. T. Ma, A. Gupta, G. Lee, S. Makuta, Y. Tachibana, W. Chen, L. Spiccia, Y. B. Cheng, G. Götz, P. Bäuerle and U. Bach, *J. Phys. Chem. C*, 2014, **118**, 16375–16379.
- 227 D. Xiong, W. Zhang, X. Zeng, Z. Xu, W. Chen, J. Cui, M. Wang, L. Sun and Y. B. Cheng, *ChemSusChem*, 2013, **6**, 1432–1437.
- 228 D. Xiong, Z. Xu, X. Zeng, W. Zhang, W. Chen, X. Xu, M. Wang and Y. B. Cheng, *J. Mater. Chem.*, 2012, **22**, 24760–24768.
- 229 X. Xu, J. Cui, J. Han, J. Zhang, Y. Zhang, L. Luan, G. Alemu, Z. Wang, Y. Shen, D. Xiong, W. Chen, Z. Wei, S. Yang, B. Hu, Y. Cheng and M. Wang, *Sci. Rep.*, 2014, **4**, 3961.
- 230 M. Yu, T. I. Draskovic and Y. Wu, *Phys. Chem. Chem. Phys.*, 2014, **16**, 5026–5033.
- 231 A. K. Diaz-Garcia, T. Lana-Villarreal and R. Gomez, *J. Mater. Chem. A*, 2015, **3**, 19683–19687.
- 232 A. Varga, G. F. Samu and C. Janáky, *Electrochim. Acta*, 2018, **272**, 22–32.
- 233 K. H. L. Zhang, K. Xi, M. G. Blamire and R. G. Egdell, *J. Phys. Condens. Matter*, 2016, **28**, 383002.
- 234 D. O. Scanlon and G. W. Watson, *J. Mater. Chem.*, 2011, **21**, 3655–3663.
- 235 T. Jiang, X. Li, M. Bujoli-Doeuff, E. Gautron, L. Cario, S. Jobic and R. Gautier, *Inorg.*

- Chem.*, 2016, **55**, 7729–7733.
- 236 D. O. Scanlon, K. G. Godinho, B. J. Morgan and G. W. Watson, *J. Chem. Phys.*, 2010, **132**, 024707.
- 237 R. Nagarajan, N. Duan, M. K. Jayaraj, J. Li, K. a. Vanaja, a. Yokochi, a. Draeseke, J. Tate and a. W. Sleight, *Int. J. Inorg. Mater.*, 2001, **3**, 265–270.
- 238 T. Arnold, D. J. Payne, A. Bourlange, J. P. Hu, R. G. Egdell, L. F. J. Piper, L. Colakerol, A. Masi, P. A. Glans, T. Learmonth, K. E. Smith, J. Guo, D. O. Scanlon, A. Walsh, B. J. Morgan and G. W. Watson, *Phys. Rev. B*, 2009, **79**, 1–9.
- 239 A. Barnabé, Y. Thimont, M. Lalanne, L. Presmanes and P. Tailhades, *J. Mater. Chem. C*, 2015, **3**, 6012–6024.
- 240 W. C. Sheets, E. Mugnier, A. Barnabé, T. J. Marks and K. R. Poeppelmeier, *Chem. Mater.*, 2006, **18**, 7–20.
- 241 J. Wang, P. Zheng, D. Li, Z. Deng, W. Dong, R. Tao and X. Fang, *J. Alloys Compd.*, 2011, **509**, 5715–5719.
- 242 S. Götzendörfer, C. Polenzky, S. Ulrich and P. Löbmann, *Thin Solid Films*, 2009, **518**, 1153–1156.
- 243 S. Hennessey and P. Farràs, *Chem. Commun.*, 2018, **54**, 6662–6680.
- 244 L. Lepleux, B. Chavillon, Y. Pellegrin, E. Blart, L. Cario, S. Jobic and F. Odobel, *Inorg. Chem.*, 2009, **48**, 8245–8250.
- 245 S. Sumikura, S. Mori, S. Shimizu, H. Usami and E. Suzuki, *J. Photochem. Photobiol. A Chem.*, 2008, **199**, 1–7.
- 246 S. Jana, S. Samai, B. C. Mitra, P. Bera and A. Mondal, *Dalt. Trans.*, 2014, **43**, 13096–13104.
- 247 N. Li, E. A. Gibson, P. Qin, G. Boschloo, M. Gorlov, A. Hagfeldt and L. Sun, *Adv. Mater.*, 2010, **22**, 1759–1762.
- 248 A. L. Smeigh, L. Le Pleux, J. Fortage, Y. Pellegrin, E. Blart, F. Odobel and L. Hammarström, *Chem. Commun.*, 2012, **48**, 678–680.
- 249 F. Odobel, Y. Pellegrin, E. A. Gibson, A. Hagfeldt, A. L. Smeigh and L. Hammarström, *Coord. Chem. Rev.*, 2012, **256**, 2414–2423.
- 250 F. Odobel and Y. Pellegrin, *J. Phys. Chem. Lett.*, 2013, **4**, 2551–2564.
- 251 L. D'Amario, L. J. Antila, B. Pettersson Rimgard, G. Boschloo and L. Hammarström, *J. Phys. Chem. Lett.*, 2015, **6**, 779–783.
- 252 S. H. Kang, K. Zhu, N. R. Neale and A. J. Frank, *Chem. Commun.*, 2011, **47**, 10419–10421.
- 253 A. Morandeira, J. Fortage, T. Edvinsson, L. Le Pleux, E. Blart, G. Boschloo, A. Hagfeldt, L. Hammarström and F. Odobel, *J. Phys. Chem. C*, 2008, **112**, 1721–1728.
- 254 C. J. Brinker and G. W. Scherer, *Sol-Gel Science: The Physics and Chemistry of Sol-*

- Gel Processing*, Academic Press Ltd., Elsevier, London, UK, 1990.
- 255 J. Zarzycki, *J. Sol-Gel Sci. Technol.*, 1997, **8**, 17–22.
- 256 A. Tang, C. Zhan, J. Yao and E. Zhou, *Adv. Mater.*, 2017, **29**, 1600013.
- 257 T. E. Rosser, T. Hisatomi, S. Sun, D. Antón-García, T. Minegishi, E. Reisner and K. Domen, *Chem. Eur. J.*, 2018, **24**, 18393–18397.
- 258 N. Queyriaux, E. S. Andreiadis, S. Torelli, J. Pecaut, B. S. Veldkamp, E. A. Margulies, M. R. Wasielewski, M. Chavarot-Kerlidou and V. Artero, *Faraday Discuss.*, 2017, **198**, 251–261.
- 259 J. Bisquert, *J. Phys. Chem. B*, 2001, **106**, 325–333.
- 260 M. Pazoki, U. B. Cappel, E. M. J. Johansson, A. Hagfeldt and G. Boschloo, *Energy Environ. Sci.*, 2017, **10**, 672–709.
- 261 J. Bisquert and I. Mora-Seró, *J. Phys. Chem. Lett.*, 2010, **1**, 450–456.
- 262 K. D. Benkstein, N. Kopidakis, J. van de Lagemaat and A. J. Frank, *J. Phys. Chem. B*, 2003, **107**, 7759–7767.
- 263 J. Halme, G. Boschloo, A. Hagfeldt and P. Lund, *J. Phys. Chem. C*, 2008, **112**, 5623–5637.
- 264 P. R. F. Barnes, A. Y. Anderson, S. E. Koops, J. R. Durrant and B. C. O'Regan, *J. Phys. Chem. C*, 2009, **113**, 1126–1136.
- 265 E. A. Gibson, A. L. Smeigh, L. Le Pleux, L. Hammarström, F. Odobel, G. Boschloo and A. Hagfeldt, *J. Phys. Chem. C*, 2011, **115**, 9772–9779.
- 266 A. J. Bard, A. B. Bocarsly, F. R. F. Fan, E. G. Walton and M. S. Wrighton, *J. Am. Chem. Soc.*, 1980, **102**, 3671–3677.
- 267 A. J. Bard, F. R. F. Fan, A. S. Gioda, G. Nagasubramanian and H. S. White, *Faraday Discuss. Chem. Soc.*, 1980, **70**, 19–31.
- 268 M. S. Prévot, X. A. Jeanbourquin, W. S. Bourée, F. Abdi, D. Friedrich, R. van de Krol, N. Guijarro, F. Le Formal and K. Sivula, *Chem. Mater.*, 2017, **29**, 4952–4962.
- 269 W. Ketir, A. Bouguelia and M. Trari, *Desalination*, 2009, **244**, 144–152.
- 270 A. R. C. Bredar, M. D. Blanchet, R. B. Comes and B. H. Farnum, *ACS Appl. Energy Mater.*, 2018, **2**, 19–28.
- 271 W. Ketir, S. Saadi and M. Trari, *J. Solid State Electrochem.*, 2012, **16**, 213–218.
- 272 M. M. Raber, M. D. Brady, L. Troian-Gautier, J. C. Dickenson, S. L. Marquard, J. T. Hyde, S. J. Lopez, G. J. Meyer, T. J. Meyer and D. P. Harrison, *ACS Appl. Mater. Interfaces*, 2018, **10**, 22821–22833.
- 273 J. T. Hyde, K. Hanson, A. K. Vannucci, A. M. Lapidés, L. Alibabaei, M. R. Norris, T. J. Meyer and D. P. Harrison, *ACS Appl. Mater. Interfaces*, 2015, **7**, 9554–9562.
- 274 A. M. Lapidés, B. D. Sherman, M. K. Brennaman, C. J. Dares, K. R. Skinner, J. L. Templeton and T. J. Meyer, *Chem. Sci.*, 2015, **6**, 6398–6406.

- 275 H. J. Son, C. Prasittichai, J. E. Mondloch, L. Luo, J. Wu, D. W. Kim, O. K. Farha and J. T. Hupp, *J. Am. Chem. Soc.*, 2013, **135**, 11529–11532.
- 276 D. Wang, M. V. Sheridan, B. Shan, B. H. Farnum, S. L. Marquard, B. D. Sherman, M. S. Eberhart, A. Nayak, C. J. Dares, A. K. Das, R. M. Bullock and T. J. Meyer, *J. Am. Chem. Soc.*, 2017, **139**, 14518–14525.
- 277 B. Reuillard, J. Warnan, J. J. Leung, D. W. Wakerley and E. Reisner, *Angew. Chem. Int. Ed.*, 2016, **55**, 3952–3957.
- 278 S. K. Ibrahim, X. Liu, C. Tard and C. J. Pickett, *Chem. Commun.*, 2007, **0**, 1535–1537.
- 279 D. H. Pool and D. L. DuBois, *J. Organomet. Chem.*, 2009, **694**, 2858–2865.
- 280 A. Krawicz, J. Yang, E. Anzenberg, J. Yano, I. D. Sharp and G. F. Moore, *J. Am. Chem. Soc.*, 2013, **135**, 11861–11868.
- 281 P. Reiss, M. Carrière, C. Lincheneau, L. Vaure and S. Tamang, *Chem. Rev.*, 2016, **116**, 10731–10819.
- 282 J. Liu, Y. Liu, N. Liu, Y. Han, X. Zhang, H. Huang, Y. Lifshitz, S.-T. Lee, J. Zhong and Z. Kang, *Science*, 2015, **347**, 970–974.
- 283 R. S. Sprick, J. X. Jiang, B. Bonillo, S. Ren, T. Ratvijitvech, P. Guiglion, M. A. Zwijnenburg, D. J. Adams and A. I. Cooper, *J. Am. Chem. Soc.*, 2015, **137**, 3265–3270.
- 284 D. J. Woods, R. S. Sprick, C. L. Smith, A. J. Cowan and A. I. Cooper, *Adv. Energy Mater.*, 2017, **7**, 1700479.
- 285 A. N. Avdonin, D. D. Nedeoglo, N. D. Nedeoglo and V. P. Sirkeli, *Phys. Status Solidi Basic Res.*, 2003, **238**, 45–53.
- 286 S. Adachi and T. Taguchi, *Phys. Rev. B*, 1991, **43**, 9569–9577.
- 287 H. Kaneko, T. Minegishi, M. Nakabayashi, N. Shibata, Y. Kuang, T. Yamada and K. Domen, *Adv. Funct. Mater.*, 2016, **26**, 4570–4577.
- 288 P. Reiss, G. Quemard, S. Carayon, J. Bleuse, F. Chandezon and A. Pron, *Mater. Chem. Phys.*, 2004, **84**, 10–13.
- 289 P. D. Cozzoli, L. Manna, M. L. Curri, S. Kudera, C. Giannini, M. Striccoli and A. Agostiano, *Chem. Mater.*, 2005, **17**, 1296–1306.
- 290 Y. Xu, W. Zhao, R. Xu, Y. Shi and B. Zhang, *Chem. Commun.*, 2013, **49**, 9803–9805.
- 291 D. Jiang, Z. Sun, H. Jia, D. Lu and P. Du, *J. Mater. Chem. A*, 2015, **4**, 675–683.
- 292 L. M. Rossi, J. L. Fiorio, M. A. S. Garcia and C. P. Ferraz, *Dalt. Trans.*, 2018, **47**, 5889–5915.
- 293 E. L. Rosen, R. Buonsanti, A. Llordes, A. M. Sawvel, D. J. Milliron and B. A. Helms, *Angew. Chem. Int. Ed.*, 2012, **51**, 684–689.
- 294 X.-B. Fan, S. Yu, X. Wang, Z.-J. Li, F. Zhan, J.-X. Li, Y. Gao, A.-D. Xia, Y. Tao, X.-B.

- Li, L.-P. Zhang, C.-H. Tung and L.-Z. Wu, *Adv. Mater.*, 2019, **31**, 1804872.
- 295 E. Reisner, *Angew. Chemie Int. Ed.*, 2019, **58**, 2–4.
- 296 Z. Pan, H. Rao, I. Mora-Seró, J. Bisquert and X. Zhong, *Chem. Soc. Rev.*, 2018, **47**, 7659–7702.
- 297 C. E. Creissen, J. Warnan and E. Reisner, *Chem. Sci.*, 2018, **9**, 1439–1447.
- 298 I. Gur, N. A. Fromer, M. L. Geier and A. P. Alivisatos, *Science*, 2005, **310**, 462–465.
- 299 A. H. Ip, S. M. Thon, S. Hoogland, O. Voznyy, D. Zhitomirsky, R. Debnath, L. Levina, L. R. Rollny, G. H. Carey, A. Fischer, K. W. Kemp, I. J. Kramer, Z. Ning, A. J. Labelle, K. W. Chou, A. Amassian and E. H. Sargent, *Nat. Nanotechnol.*, 2012, **7**, 577–582.
- 300 J. Gu, A. Wuttig, J. W. Krizan, Y. Hu, Z. M. Detweiler, R. J. Cava and A. B. Bocarsly, *J. Phys. Chem. C*, 2013, **117**, 12415–12422.
- 301 J. Tang, K. W. Kemp, S. Hoogland, K. S. Jeong, H. Liu, L. Levina, M. Furukawa, X. Wang, R. Debnath, D. Cha, K. W. Chou, A. Fischer, A. Amassian, J. B. Asbury and E. H. Sargent, *Nat. Mater.*, 2011, **10**, 765–771.
- 302 J. R. Lee, W. Li, A. J. Cowan and F. Jäckel, *J. Phys. Chem. C*, 2017, **121**, 15160–15168.
- 303 B. Shan, T.-T. Li, M. K. Brennaman, A. Nayak, L. Wu and T. J. Meyer, *J. Am. Chem. Soc.*, 2019, **141**, 463–471.
- 304 R. S. Clegg and J. E. Hutchison, in *Electron Transfer in Chemistry*, ed. V. Balzani, WILEY-VCH Verlag, Weinheim, Germany, 1st edn., 2001, pp. 541–577.
- 305 G. Von Freymann, V. Kitaev, B. V. Lotsch and G. A. Ozin, *Chem. Soc. Rev.*, 2013, **42**, 2528–2554.
- 306 Q. Liu, D. Wang, B. Shan, B. D. Sherman, S. L. Marquard, M. S. Eberhart, M. Liu, C. Li and T. J. Meyer, *J. Chem. Phys.*, 2019, **150**, 041727.
- 307 K. P. Sokol, W. E. Robinson, J. Warnan, N. Kornienko, M. M. Nowaczyk, A. Ruff, J. Z. Zhang and E. Reisner, *Nat. Energy*, 2018, **3**, 944–951.
- 308 D. Mersch, C. Y. Lee, J. Z. Zhang, K. Brinkert, J. C. Fontecilla-Camps, A. W. Rutherford and E. Reisner, *J. Am. Chem. Soc.*, 2015, **137**, 8541–8549.
- 309 S. Guldin, S. Hüttner, M. Kolle, M. E. Welland, P. Müller-Buschbaum, R. H. Friend, U. Steiner and N. Tétreault, *Nano Lett.*, 2010, **10**, 2303–2309.
- 310 J. H. Shin, J. H. Kang, W. M. Jin, J. H. Park, Y. S. Cho and J. H. Moon, *Langmuir*, 2011, **27**, 856–860.
- 311 S. H. A. Lee, N. M. Abrams, P. G. Hoertz, G. D. Barber, L. I. Halaoui and T. E. Mallouk, *J. Phys. Chem. B*, 2008, **112**, 14415–14421.
- 312 J. W. Lee, J. Lee, C. Kim, C. Y. Cho and J. H. Moon, *Sci. Rep.*, 2014, **4**, 6804.
- 313 N. Tétreault and M. Grätzel, *Energy Environ. Sci.*, 2012, **5**, 8506–8516.
- 314 B. Hatton, L. Mishchenko, S. Davis, K. H. Sandhage and J. Aizenberg, *Proc. Natl.*

- Acad. Sci. U. S. A.*, 2010, **107**, 10354–10359.
- 315 G. I. N. Waterhouse and M. R. Waterland, *Polyhedron*, 2007, **26**, 356–368.
- 316 L. Zhang, E. Reisner and J. J. Baumberg, *Energy Environ. Sci.*, 2014, **7**, 1402–1408.
- 317 E. A. Gaulding, G. Liu, C. T. Chen, L. Löbber, A. Li, G. Segev, J. Eichhorn, S. Aloni, A. M. Schwartzberg, I. D. Sharp and F. M. Toma, *J. Mater. Chem. A*, 2017, **5**, 11601–11614.
- 318 S. Jeong, S. Seo and H. Shin, *RSC Adv.*, 2018, **8**, 27956–27962.
- 319 W. A. Dunlap-Shohl, T. B. Daunis, X. Wang, J. Wang, B. Zhang, D. Barrera, Y. Yan, J. W. P. Hsu and D. B. Mitzi, *J. Mater. Chem. A*, 2018, **6**, 469–477.
- 320 J. N. Clifford, E. Palomares, M. K. Nazeeruddin, M. Grä, J. Nelson, X. Li, N. J. Long and J. R. Durrant, *J. Am. Chem. Soc.*, 2004, **126**, 5225–5233.
- 321 M. Borgström, E. Blart, G. Boschloo, E. Mukhtar, A. Hagfeldt, L. Hammarström and F. Odobel, *J. Phys. Chem. B*, 2005, **109**, 22928–22934.
- 322 A. Morandeira, G. Boschloo, A. Hagfeldt and L. Hammarström, *J. Phys. Chem. B*, 2005, **109**, 19403–19410.
- 323 T. Daeneke, Z. Yu, G. P. Lee, D. Fu, N. W. Duffy, S. Makuta, Y. Tachibana, L. Spiccia, A. Mishra, P. Bäuerle and U. Bach, *Adv. Energy Mater.*, 2015, **5**, 1401387.
- 324 Y. Farré, F. Maschietto, J. Föhlinger, M. Wykes, A. Planchat, Y. Pellegrin, E. Blart, I. Ciofini, L. Hammarström and F. Odobel, *Manuscript_In_Preparation*.
- 325 F. Würthner, C. R. Saha-Möller, B. Fimmel, S. Ogi, P. Leowanawat and D. Schmidt, *Chem. Rev.*, 2016, **116**, 962–1052.
- 326 C. Queffélec, M. Petit, P. Janvier, D. A. Knight and B. Bujoli, *Chem. Rev.*, 2012, **112**, 3777–3807.
- 327 J. G. Van Alsten, *Langmuir*, 1999, **15**, 7605–7614.
- 328 R. Kamata, H. Kumagai, Y. Yamazaki, G. Sahara and O. Ishitani, *ACS Appl. Mater. Interfaces*, 2019, **11**, 5632–5641.
- 329 T.-T. Li, B. Shan and T. J. Meyer, *ACS Energy Lett.*, 2019, **4**, 629–636.
- 330 A. Leventis, J. Royakkers, A. G. Rapisdis, N. Goodeal, M. K. Corpinot, J. M. Frost, D. K. Bučar, M. O. Blunt, F. Cacialli and H. Bronstein, *J. Am. Chem. Soc.*, 2018, **140**, 1622–1626.
- 331 G. Saranya, C. Yam, S. Gao and M. Chen, *J. Phys. Chem. C*, 2018, **122**, 23280–23287.
- 332 P. Salvatori, G. Marotta, A. Cinti, C. Anselmi, E. Mosconi and F. De Angelis, *J. Phys. Chem. C*, 2013, **117**, 3874–3887.
- 333 F. A. Armstrong, N. A. Belsey, J. A. Cracknell, G. Goldet, A. Parkin, E. Reisner, K. A. Vincent and A. F. Wait, *Chem. Soc. Rev.*, 2009, **38**, 36–51.
- 334 K. A. Vincent, A. Parkin and F. A. Armstrong, *Chem. Rev.*, 2007, **107**, 4366–4413.

- 335 W. Lubitz, H. Ogata, O. Rüdiger and E. Reijerse, *Chem. Rev.*, 2014, **114**, 4081–4148.
- 336 T. Sakai, D. Mersch and E. Reisner, *Angew. Chem. Int. Ed.*, 2013, **52**, 12313–12316.
- 337 N. A. Romero and D. A. Nicewicz, *Chem. Rev.*, 2016, **116**, 10075–10166.
- 338 M. H. Shaw, J. Twilton and D. W. C. MacMillan, *J. Org. Chem.*, 2016, **81**, 6898–6926.

A. Appendix

A.1. H₂ Quantification by Gas Chromatography

For H₂ quantification using gas chromatography (GC), CH₄ (2% in N₂) was used as the internal standard. The GC was calibrated regularly to obtain a response factor (RF), which relates the amount of H₂ to the amount of CH₄ with the peak areas (A):

$$\frac{n_{H_2}}{n_{CH_4}} = RF \times \frac{A_{H_2}}{A_{CH_4}}$$

The amount of CH₄ can be calculated using the ideal gas law, where R is the ideal gas constant, V_{headspace} is the headspace volume in the cell, T is the temperature, and p is the pressure (atmospheric):

$$n_{CH_4} = \frac{pV_{headspace} \times 0.02}{RT}$$

The amount of H₂ in the headspace is then obtained by relating the two equations:

$$n_{H_2} = RF \times \frac{A_{H_2}}{A_{CH_4}} \times \frac{pV_{headspace} \times 0.02}{RT}$$

Henry's law was used to estimate the amount of H₂ dissolved in solution:

$$H = \frac{C_{(aq)}}{P_i}$$

where C_(aq) is the concentration in the aqueous phase and P_i is the partial pressure in the headspace. For H₂, the partial pressure is equal to the %H₂ in the headspace assuming the cell pressure is constant at 1 atm.

$$\%H_2 = P_i(H_2)$$

The number of moles of gas in solution can then be calculated from the known amount in the headspace as determined using gas chromatography, accounting for the 2 % CH₄ / N₂ mixture, where H is Henry's constant, and V is the volume of solution.

$$\%H_2 = \left(\frac{A_{H_2}/A_{CH_4}}{\text{response factor}} \right) \times 0.02$$

The amount of H₂ dissolved in solution is then given by the equation below:

$$n = CV = \%H_2 \times H \times V$$

The headspace and solution H₂ were added to obtain the total amount of H₂ generated.

A.2. Additional Figures

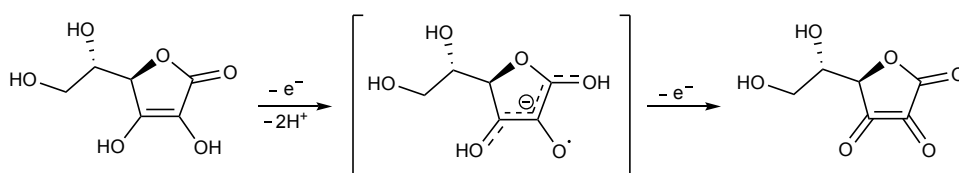


Figure A1 – Oxidation of ascorbic acid to dehydroascorbic acid.

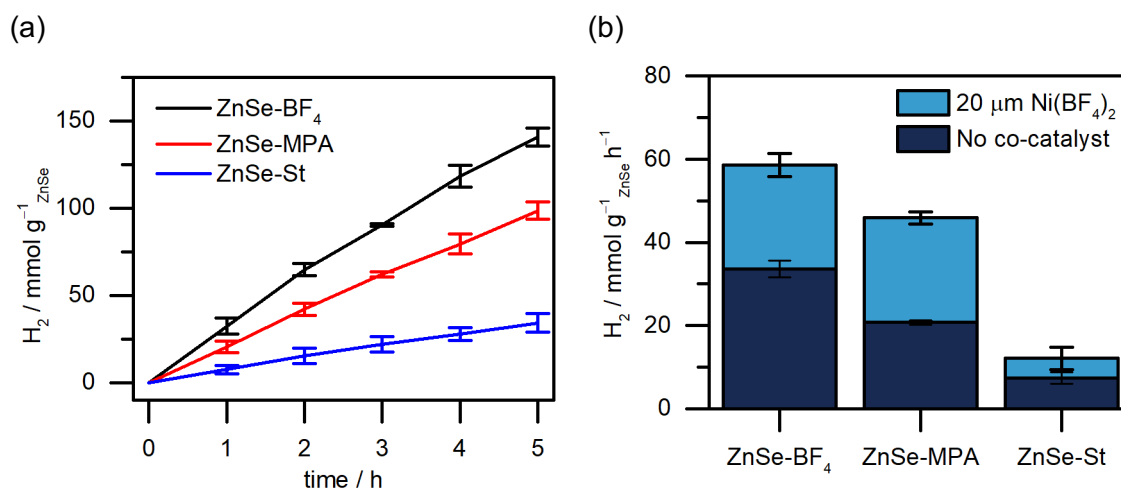


Figure A2 – a) Photocatalysis with ZnSe-BF₄, ZnSe-St, and ZnSe-MPA NRs ($\lambda > 400$ nm), b) the rate of H₂ generation after 3 h irradiation in the presence and absence of 20 μm Ni(BF₄)₂ under UV-filtered light ($\lambda > 400$ nm). Conditions: 50 mg L⁻¹ ZnSe, 0.4 M AA, pH 4.5, 25 °C, 100 mW cm⁻², AM 1.5G.

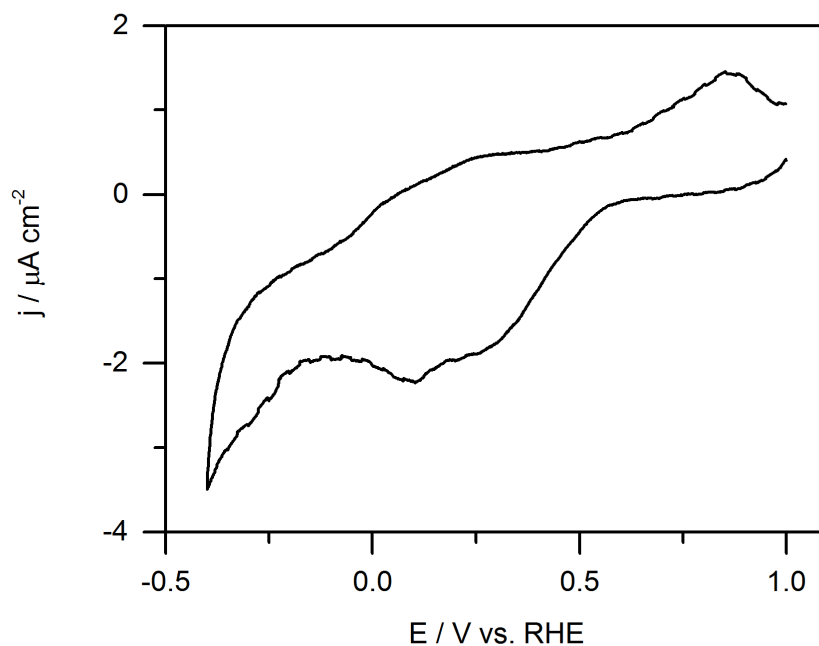


Figure A3– CV of an ITO|ZnSe electrode in 0.1 M Na₂SO₄, pH 5.5 with chopped light illumination (100 mW cm⁻², AM 1.5G, λ > 400 nm), scan rate = 5 mV s⁻¹.

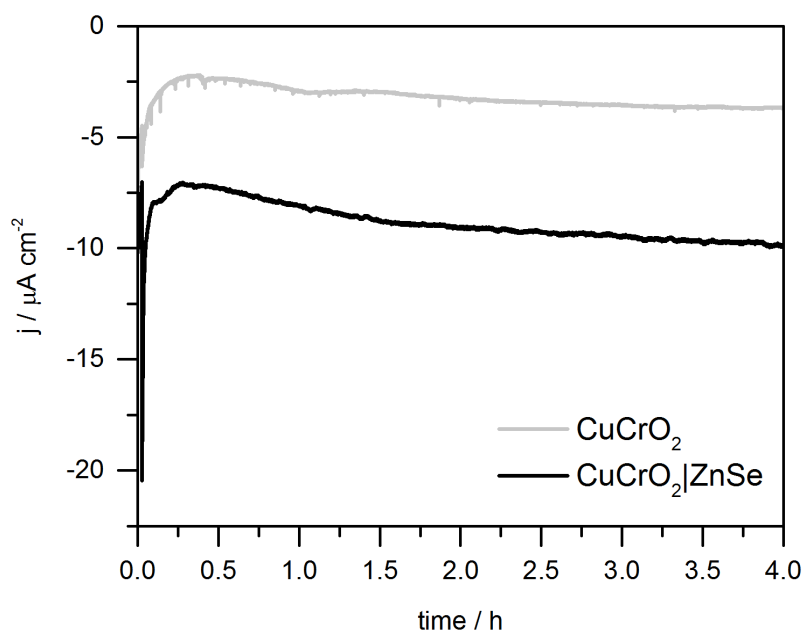


Figure A4 – CPPE of blank CuCrO₂ and CuCrO₂|ZnSe electrodes conducted in 0.1 M Na₂SO₄, pH 5.5 under illumination (100 mW cm⁻², AM 1.5G, λ > 400 nm).

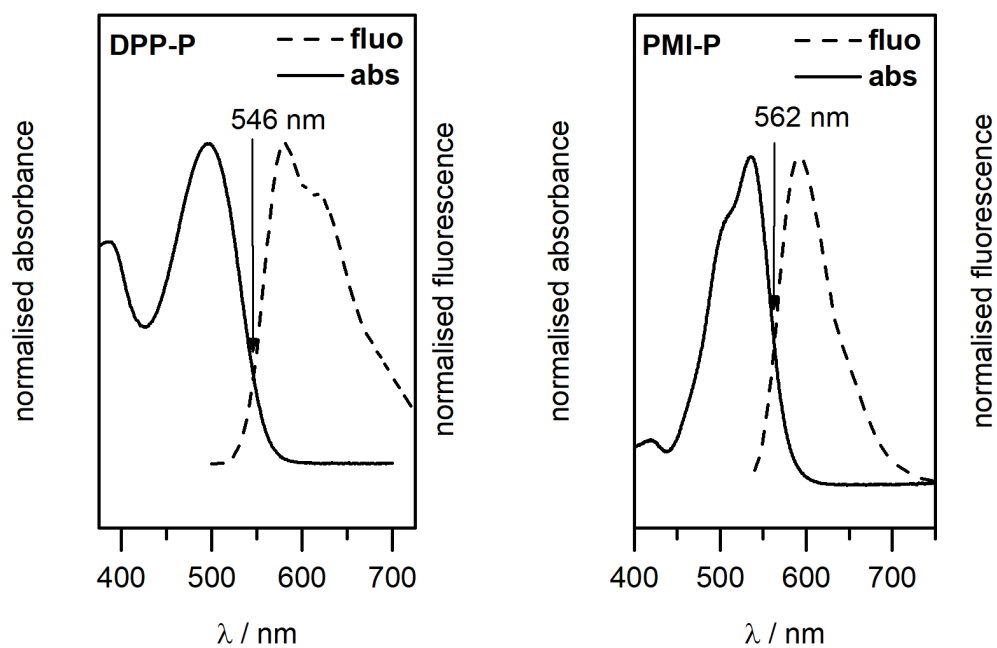


Figure A5 – Normalised absorption and emission spectra with intersection labelled for the determination of E_{00} with **PMI-P** and **DPP-P**.

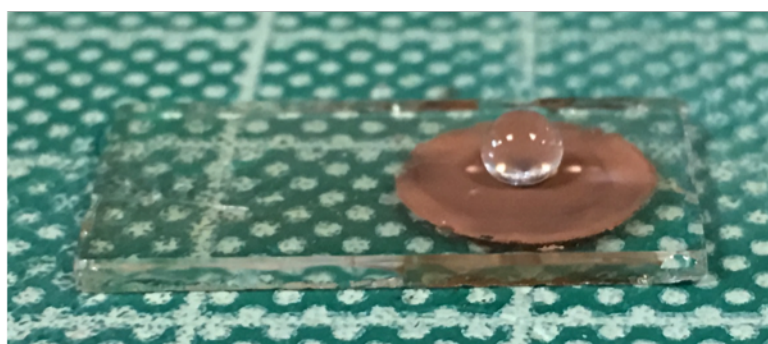


Figure A6 – Photograph of a water droplet on an IO-CuCrO₂|DPP-P electrode.

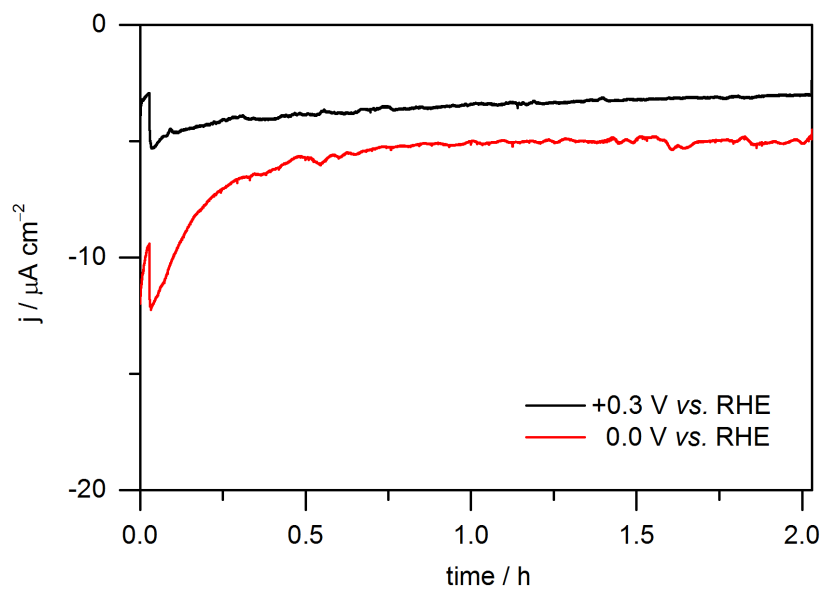


Figure A7 – CPPE of IO-CuCrO₂ electrodes under illumination at applied potentials of +0.3 V and 0 V vs. RHE. Conditions: aqueous Na₂SO₄ (0.1 M, pH3), light intensity of 100 mW cm⁻², AM 1.5G, $\lambda > 420$ nm.